The effect of endwall contouring on the unsteady flow through a turbine rotor

by

Dwain Iain Dunn

Dissertation presented for the degree of Doctor of Philosophy in Mechanical Engineering in the Faculty of Engineering at Stellenbosch University

Department of Mechanical and Mechatronics Engineering,
University of Stellenbosch,
Private Bag X1, Matieland 7602, South Africa.

Promoter: Prof. T.W. von Backström

December 2014

Declaration

By submitting this dissertation electronically, I declare that the entirety of the work contained therein is my own, original work, that I am the sole author thereof (save to the extent explicitly otherwise stated), that reproduction and publication thereof by Stellenbosch University will not infringe any third party rights and that I have not previously in its entirety or in part submitted it for obtaining any qualification.

Signature: .....
D.I. Dunn

Date: Tuesday 8th July, 2014
.....

Abstract

The effect of endwall contouring on the unsteady flow through a turbine rotor

D.I. Dunn

Department of Mechanical and Mechatronics Engineering,
University of Stellenbosch,
Private Bag X1, Matieland 7602, South Africa.

Dissertation: PhDEng (Mech)

December 2014

With increasing environmental concerns and the drive for a greener economy comes an increased desire to improve turbine engine fuel efficiency and reduce emissions. Unfortunately weight reduction techniques used increase the blade loading, which in turn increases the losses. Non-axisymmetric endwall contouring is one of several techniques being investigated to reduce loss in a turbine. An investigation at Durham University produced a non-axisymmetric endwall design for a linear cascade. An adaption of the most promising endwall was investigated in an annular rotating test rig at the CSIR using steady state instrumentation. The current investigation extends those investigations into the unsteady time domain.

Previous investigations found that a generic rotor endwall contour improved efficiency by controlling the endwall secondary flow vortex system in both a linear cascade and an annular $1\frac{1}{2}$ stage rotating test turbine. The current research was aimed at determining if there were any unsteady effects introduced by the contoured endwall. The approach was unique in that it investigated the unsteady effects of an endwall contour originally designed for a linear cascade both experimentally and numerically at three incidence angles (positive, zero and negative to represent increased load, design load and decreased load respectively), the results of which are openly available.

Unsteady experimental hotfilm results showed that the endwall contour made the velocity profile more radially uniform by reducing the strength of the endwall secondary flow vortex system. The fluctuations in the velocity were also reduced producing a more temporally uniform velocity profile. The FFT magnitude of the velocity at the blade passing frequency below midspan was also reduced. It was found that the reduction in the endwall secondary flow vortex system due to the contour increased with increasing loading.

Numerical results showed that the oscillations in the flow were small and did not penetrate the boundary layer. The contoured rotor was forward and aft loaded when compared to the annular rotor, resulting in a weaker cross passage pressure gradient which allowed the endwall secondary flow vortex system to be less tightly wrapped. Numerical results did

not show a significant difference in the oscillations observed in the annular and contoured rotor.

A new objective function for use in the endwall optimisation process was proposed that acts as a proxy for efficiency, but is less prone to uncertainty in the results. When used on the current results it shows the same trend as efficiency. It remains to be used to design an endwall for full validation.

Uittreksel

Die effek van endwandprofilering op die onbestendige vloei deur 'n turbine rotor.

("The effect of endwall contouring on the unsteady flow through a turbine rotor")

D.I. Dunn

Departement Meganiese en Megatroniese Ingenieurswese,
Universiteit van Stellenbosch,
Privaatsak X1, Matieland 7602, Suid Afrika.

Proefskrif: PhDIng (Meg)

Desember 2014

Met 'n toenemende omgewingsbesorgdheid en die strewe na 'n groener ekonomie kom 'n toenemende behoefte om turbine enjin brandstofdoeltreffendheid te verbeter en vrystellings te verlaag. Ongelukkig het gewigsbesparingstegnieke wat gebruik is die lemlading verhoog, wat op sy beurt die verliese verhoog. Nie-assimmetriese endwandprofilering is een van verskeie tegnieke wat ondersoek word om verliese in 'n turbine te verminder. 'n Ondersoek by die Universiteit van Durham het 'n nie-assimmetriese endwandontwerp vir 'n lineêre kaskade gelewer. 'n Aanpassing van die mees belowende endwand is in 'n annulêre roterende toetsopstelling by die WNNR getoets, deur gebruik te maak van bestendige toestand instrumentasie. Die huidige ondersoek brei daardie ondersoeke uit na die nie-bestendige verwysingsraamwerk .

Vorige ondersoeke het bevind dat die generiese rotor endwandprofiel doeltreffendheid verbeter as gevolg van die beheer van die endwand sekondêre vloei draaikolkstelsel in beide 'n lineêre kaskade sowel as 'n annulêre $1\frac{1}{2}$ stadium roterende toetsturbine. Die huidige navorsing was daarop gemik om vas te stel of die endwandprofiel enige onbestendige effekte tot gevolg gehad het. Die benadering was uniek in die sin dat dit die onbestendige effekte ondersoek het van 'n endwandprofiel wat oorspronklik ontwerp is vir 'n lineêre kaskade beide eksperimenteel en numeries op drie invalsshoeke (positief, nul en negatief om onderskeidelik verhoogde lading, ontwerplading en verlaagde lading te verteenwoordig), waarvan die resultate algemeen beskikbaar is.

Onbestendige eksperimentele warmfilm resultate het getoon dat die endwandprofiel die snelheidsprofiel meer radiaal uniform gemaak het deur die vermindering van die sterkte van die endwand sekondêre vloei werwelstelsel. Die skommelinge in die snelheid is ook verminder wat 'n meer tyduniforme snelheidsprofiel gelewer het. Die FFT (Fast Fourier Transform) grootte van die snelheid van die lem verbygaan frekwensie onder lem midbestek het ook verminder. Daar was bevind dat die vermindering in die endwand sekondêre vloei draaikolkstelsel as gevolg van die endwandprofiel toeneem met toenemende lading.

Numeriese resultate het getoon dat die ossilasie in die vloei klein was en nie die grenslaag binnegedring het nie. Die rotor met gevormde wand het 'n voor- en agterlading gehad in vergelyking met die rotor met annulêre wand, wat tot 'n laer drukgradient dwarsop die vloeirigting gelei het, die endwand sekondêre vloei draaikolkstelsel minder beperk het. Numeriese resultate het nie 'n beduidende verskil in die ossilasies tussen die annulêre en gevormde rotorwand getoon nie.

'n Nuwe doelwitfunksie vir gebruik in die endwand optimersproses is voorgestel wat dien as 'n plaasvervanger vir doeltreffendheid, maar minder geneig is tot onsekerheid in die resultate. Wanneer dit gebruik word op die huidige resultate toon dit dieselfde tendens as doeltreffendheid. Dit moet nog gebruik word in die ontwerp van 'n endwand vir volledige bevestiging.

Acknowledgements

I would like to express my sincere gratitude to the following people and organisations:

- First and foremost I'd like to thank The Lord, our Father, without whom nothing is possible.
- I'd also like to thank my beautiful wife and children, for their love and support through this PhD.
- Dr Glen Snedden for his encouragement and assistance in getting everything required for the research.
- The CSIR for providing funding for this research and providing the time needed to finish.
- Prof von Backström for guidance and support through out this research.
- Percy Mdluli who helped complete the experimental tests.
- Thomas Hildebrandt and Numeca Ingenieurbüro for support of the numerical works.
- Ndumiso Zwane and Frikkie Rossouw for early technical support.
- All the vacation student who helped keep the test rig well maintained.

Contents

List of Figures

List of Tables

Nomenclature

Roman Symbols

A	Area	$[(\mathrm{m}^2)]$
C	Velocity, Coefficient	$[(\mathrm{m/s}), (-)]$
E	Bridge voltage	$[(\mathrm{V})]$
i, j, k	Perpendicular unit vectors	$[(-)]$
L	Length	$[(\mathrm{m})]$
n	Number	$[(-)]$
R	Radius, Radial	$[\mathrm{mm}]$
P	Pressure	$[(\mathrm{Pa})]$
P_R	Power	$[(\mathrm{W})]$
S	Span	$[(\mathrm{mm})]$
S-T	Static-to-Total	$[(-)]$
t	Time	$[(\mathrm{s})]$
T-T	Total-to-Total	$[(-)]$
T	Temperature	$[(\mathrm{K})]$
U	Blade/wheel speed	$[(\mathrm{m/s})]$
W	Rotational speed	$[(\mathrm{RPM})]$
W_s	Specific work	$[(\mathrm{J/kg})]$
$X1$-$X4$	Axial measurement location	$[(-)]$
y	Distance off surface of interest	$[\mathrm{mm}]$
$y+$	Dimensionless wall distance	$[(-)]$

Greek Symbols

α	Yaw angle	$[(^\circ)]$
β	Relative yaw angle	$[(^\circ)]$
γ	Heat capacity ratio	$[(-)]$
Δ	Difference	$[(-)]$
δ_{ij}	The Kronecker Delta	$[-]$
ϵ	Turbulent energy dissipation rate	$[(\mathrm{m}^2/\mathrm{s}^3)]$
η	Efficiency	$[(\%)]$
η_{de}	Design efficacy	$[(-)]$

θ	Angle	$[(^\circ)]$
μ	Viscosity	$[(\mathrm{kg/m.s})]$
μ_t	Turbulent viscosity	$[(\mathrm{kg/m.s})]$
ρ	Density	$[(\mathrm{kg/m^3})]$
ϕ	Pitch angle	$[(^\circ)]$
Ω	Reduced frequency	$[(-)]$
ω	Rotational speed, Specific turbulent energy dissipation rate	$[(\mathrm{rad/s}, \mathrm{m^2/s^3})]$

Subscripts

0	Initial
$1, 2, 3$	Perpendicular velocity components
3	At measurement location X3
abs	Absolute
A	Primary Sensor
B	Bridge,Secondary Sensor
$B2B$	Blade to Blade
cal	Calibration
d	Drag
$design$	Design condition
D	Design
E	Expected
eff	Effective
f	Friction
$inlet$	Inlet
l	Lift
le	Leading edge
$local$	Local conditions (current point)
m	Mean, Momentum
mag	Magnitude
max	Maximum
o	Outlet
R	Rotor
r	Radial
ref	Reference value
S	Stator, Sensor
sec	Secondary
$span$	Axial
$static$	Static
t	Tangential,turbulent

te	Trailing edge
total	Total
w	Whirl
x	Axial

Superscript

$'$	Corrected

Abbreviations

2D	Two-Dimensional
3D	Three-Dimensional
AGS	Abu-Ghannam and Shaw
CAD	Computer Aided Design
CFD	Computational Fluid Dynamics
CSIR	Council for Scientific and Industrial Research
FFT	Fast Fourier Transform
FRAP	Fast Response Aerodynamic Probe
IFA300	Thermal anemometer system from TSI
LES	Large Eddy Simulation
MIT	Massachusetts Institute of Technology
NLH	Non-Linear Harmonic
NREC	Northern Research and Engineering Corporation
P2	Profile 2
PLA	Phase Lock Average
RPM	Revolutions per minute
SST	Shear Stress Transport
TSI	Precision measurement equipment manufacturer
TTL	Transistor-transistor logic
UK	United Kingdom
VITAL	EnVIronmenTALly Friendly Aero Engine

Chapter 1

Introduction

With rising fuel prices and increased concern for the environment there has been a general push by commercial and military aviation stakeholders to reduce fuel consumption and thereby reduce emissions. The Kyoto Protocol (United Nations Framework Convention on Climate Change (UNFCCC), 2013) exemplifies this which requires signatories to reduce greenhouses gas emissions. One of the methods used to reduce emissions is to improve fuel efficiency which can be done by reducing losses inherent in the turbine engine.

Secondary flows have been shown by several researchers (Harrison, 1990; Hodson and Dominy, 1987*b*; Ingram, 2003; Marchal and Sieverding, 1977; Moustapha *et al.*, 1985; Rose *et al.*, 2001; Snedden, 2011) to exist in turbomachinery, and are typically defined as being off design flows that cause unexplained secondary losses (Moore, 1985). Secondary flows in a turbine have a detrimental effect on efficiency which means a higher cost of operation. Rose (1994) stated that increasing the efficiency of a turbine by 0.1 % equated to a saving of approximately \$22000 a year in 1994HF for a Boeing 747. Snedden (2011) more recently stated that even a 0.1 % increase in engine efficiency across the full operating range of the American aviation business could translate to a saving of 53 million litres of fuel a year (based on the MIT Airline Data project of 2008 (Swelbar and Belobaba, 2010)).

In an attempt to reduce weight as a means of reducing fuel consumption, the number of blades per turbine disc are decreasing. The result of this is an increase in the work required out of the working fluid in order to maintain the same output. Secondary flows become more prevalent in cases where the aspect ratio decreases or the aerodynamic duty (blade loading) increases (Harvey *et al.*, 2002). Therefore as turbine engines get smaller and lighter for a given thrust rating, the secondary flows become stronger. A reduction in secondary flow leads to an increase in performance of the turbine engine. One of the methods currently being investigated to control secondary flows is non-axisymmetric endwall contouring.

1.1 Reasons for current investigation

Ingram (2003) performed linear cascade experiments at Durham University in collaboration with Rolls-Royce plc. using non-axisymmetric endwall contouring and found that contouring can improve efficiency if designed correctly. Brennan *et al.* (2001), Rose *et al.* (2001) and Harvey *et al.* (2002) experimentally tested endwall contouring using a model test turbine and found up to 0.9 % improvement in efficiency.

Snedden (2011) performed experimental investigations aimed at inspecting the performance of a generic endwall, as tested by Ingram (2003) in a linear cascade, in a annular

rotating environment. The experiments were aimed at investigating the steady effects, and it was found that the generic endwall contouring improved efficiency in the rotating environment as well. The current investigation was performed in conjunction and collaboration with the work of Snedden (2011).

In a series of investigations on low pressure turbines, Addison and Hodson (1990*a*,*b*) found that laminar, transitional and turbulent boundary layers exist in a turbine, with the start of the transition being unsteady and dominated by upstream stator wake turbulence. Rose *et al.* (2013) has also stated that vortices in the upstream blade wakes cause fluctuations in the lift of the rotor. Since the endwall contour alters the vortex structure there could also be an unsteady change to the lift profile. Miller (2013) also pointed out that efficiency was increased by as much as ~ 0.5 % by heat transfer due to convective cooling, which would be impacted by changes to the unsteady vortex structure. The habilitation thesis of Rose (2011) found that an increase in unsteady interaction lead to an increase in efficiency. It should however be noted that this was due to the reduction in mixing losses caused by heat transfer between the stator wake and the free stream.

In order to fully understand the effects that the non-axisymmetric endwall contour has on the flow field, it was required that unsteady measurements be performed to determine the following:

- Does the non-axisymmetric rotor endwall contour introduce any unsteady effects not present in the annular rotor?
- Will unsteady CFD analysis provide better results than steady state analysis?
- Does the reduction in secondary losses still apply for unsteady flow conditions?
- How does off design operation affect those changes observed?

The following activities were performed in order to answer those questions:

- A hotfilm system from TSI was obtained, commissioned and integrated into the CSIR $1\frac{1}{2}$ stage test turbine.
- A software suite was developed for analysis of the data.
- Hotfilm measurements were performed for both annular and contoured rotors at design condition as well as increased loading ($+5°$ incidence angle) and decreased loading ($-5°$ incidence angle) conditions.
- Unsteady CFD was performed replicating the operating conditions of the test rig.

As a means to accelerate the current research some assistance was given to Snedden (2011) as the test rig can only be used to perform steady or unsteady experiments individually, not both concurrently. It was also felt that in some cases it would be prudent as it would ensure consistency in technique. Unless otherwise stated all the work presented in this thesis was performed by the author.

1.2 Limitations

As with any research project there are limitations. Some of the major limitations are highlighted below:

- Some of the work in this investigation was carried out as part of the European Union funded Framework Programme 6, project VITAL. Due to the collaboration some decisions were taken to facilitate the outcomes of the project. Most notably the choice of blade numbers to allow for geometry simplifications in the numerical work.
- The test rig used was originally designed for tip clearance work, and as such all three of the blade rows had a tip gap. This is contrary to an actual turbine where the rotors have a tip gap and the stators have a hub gap.

1.3 Outline of thesis

The thesis will be presented in the following order:

- Introduction - this section
- Literature Survey - the aim of this section is to acclimate the reader with gas turbines in general, as well as a brief description of losses in a turbine. It follows on to describe secondary flows and a few of the loss reductions mechanisms currently being employed and/or researched.
- Experimental Setup and Technique - the $1\frac{1}{2}$ stage turbine test rig and the associated instrumentation is described in this chapter. The sampling technique and data processing are described along with a repeatability study.
- Experimental Results - the hotfilm results are presented. Initially the time averaged results are compared to those of Snedden (2011). Then the unsteady results are presented as time and azimuthally averaged FFT and time averaged contour plots for all three operating cases. Finally velocity triangles are presented.
- Numerical Technique - a description of the numerical method is presented. The mesh and boundary conditions are presented, as well as an investigation of the most appropriate turbulence model.
- Numerical Results - the unsteady numerical results are presented as: time and azimuthally averaged results; time averaged contour plots; as well as streamlines generated to show the secondary flows.
- Discussion and Conclusions - an overall discussion is provided covering the results and their importance. A new objective function for design optimisations that was developed as a result of this investigation is also discussed.
- Recommendations - based on the work done, some recommendations for future works are presented.

Chapter 2

Literature survey

This section gives a brief overview of the literature that was surveyed in the course of this investigation. It will be shown how secondary flows impact the performance of turbines and the various methods being investigated to reduce losses. Ultimately it will be shown why the current investigation is of interest.

2.1 Gas turbine engines

A turbomachine is a device in which energy is transferred to or from a continuously flowing fluid by a dynamic action of one or more moving blade rows (Dixon, 1992). The rotating blade rows create unsteady flows in a steady state machine. A turbine engine is a form of enclosed turbomachine that produces power by expanding a fluid to a lower pressure.

The turbine is one of the most beneficial means of creating mechanical power (Sonntag *et al.*, 2003). It has no reciprocating components or rubbing members, which means that lubricating oil consumption is very low and reliability is high (Cohen *et al.*, 1996). Turbines use a continuously flowing working fluid which does not need to be contained as with internal combustion engines, making turbines relatively small for the power output. These advantages allow the turbine to be used in large scale, high temperature applications. The high efficiency makes turbine engines ideal for applications that require high levels of power for instance: electrical power generation and propulsion.

Turbines that produce in excess of 1000 MW are now in use (Cohen *et al.*, 1996). With such a large power output even the smallest improvement in efficiency can have a large impact on the cost of power generation. Ingram (2003) showed that a 265 MW electrical generation unit operating in UK conditions would increase electrical revenue by $100000 a year with a 0.1 % improvement in efficiency. Whereas with respect to propulsion Rose (1994) stated that a 0.1 % improvement in fuel consumption was worth around $22000 a year for a Boeing 747.

Due to financial incentives of such improvements (both in terms of reduced fuel usage and lower carbon taxes) it is crucial that the flow features inside a turbine engine be better understood. A greater understanding of the flow field in a turbine engine can lead to better designs which in turn will lead to reduced fuel usage and thus reduced emissions.

2.1.1 General principle of operation

A gas turbine engine is made up of 3 basic components: a compressor, a combustor and a turbine. These components can be seen schematically in Figure 2.1. The compressor increases the static pressure of the working fluid which will later be expanded through the turbine. If there are no losses during the compression and the expansion through the turbine, then the turbine would produce enough power to operate the compressor. However, losses are a reality and so energy must be supplied to the system in order to overcome the losses and to produce useful power. The energy is supplied by the combustion of fuel in the combustor in the form of heat. The combustion process occurs essentially at a constant pressure, which results in an increase in temperature and volume of the working fluid. The working fluid is then expanded through the turbine providing either rotational work or propulsion. The rotational work is provided as torque via a shaft, and the propulsive power is provided as a high velocity jet of gas (Ingram, 2003; Saravanamuttoo *et al.*, 2001).

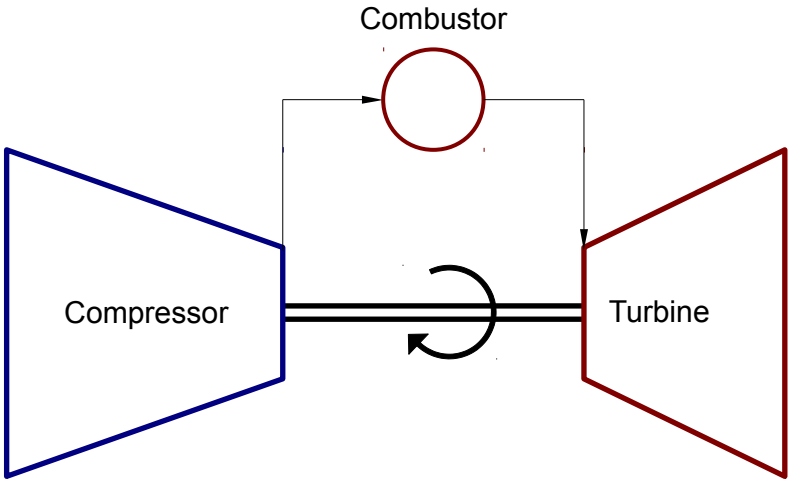

Figure 2.1: Schematic of a turbine engine showing the basic components of operation

As the gas exits the combustor it expands through alternating rows of stationary and rotating turbine discs due to the higher pressure upstream. The alternating stationary and rotating blade rows allow for the gas to be expanded and guided into the following blade row. Due to the shape of the turbine blades the turbine rotor is rotated (either due to impulse, or reaction) reducing the energy of the gas while providing shaft work. The process of conversion from pressure energy to kinetic energy to torque introduces many flow complexities.

2.1.2 Flow complexities in a turbine

In a gas turbine engine there are a variety of flow features that increase the complexity of the analysis. For this reason a linear cascade is typically used, so as to reduce the number of complexities in order to identify and investigate some of the flow features. The complexities in a turbine include, but are not limited to:

- Unsteady effects caused by the rotation of the blades. The trailing edge of the blades shed vortices into the flow field causing flow unsteadiness. These shed vortices interact with the next blade row downstream, where they can pass through unaffected or be split by the blade (clocking effects) (Jouini *et al.*, 2003).
- The potential effect of the downstream blade row changes the flow patterns even when steady state flow is assumed.
- Tip leakage flows can have a large impact on the flow field usually shown as a change in mass flow through the blade passage (Denton, 1993).
- Modern turbines can operate in the transonic region, making compressible effects important.
- Turbines are by their very nature annular in design. This induces radial and coriolis effects. These are some of the complexities that are averted with a linear cascade.
- Due to the high temperatures found in modern turbines, cooling leakage flows are used to keep the metal below its melting point. These leakage flows alter the flow structure in the turbine.
- The flow field exiting the combustor is seldomly as designed: the velocity and temperature profiles are not always uniform.
- Some turbines are not always run at the design point. This is done if extra power is required, for instance during take off.
- Due to the rotating hub of the rotor, the boundary layer gets skewed between the stator and the rotor. This increases the surface cross flow angles (Bindon, 1979). This skew can invalidate some loss correlations (Walsh and Gregory-Smith, 1990).

2.2 Loss Mechanisms

Traditionally loss can be broken down into three main categories, namely: profile loss, endwall loss and leakage loss (Denton, 1993).

2.2.1 Profile losses

Losses that are due to the blade boundary layers well away from the endwall, as well as trailing edge losses are categorised as profile losses. To simplify analysis it is often assumed that the flow is two-dimensional making it possible to base results on two-dimensional cascade results or boundary layer calculations (Denton, 1993).

2.2.2 Leakage losses

Flow that does not pass through the blade passage is classified as leakage flow. This can either be intentional as is the case for bleeding and cooling flows, or unintentional such as tip leakage flows. Tip leakage flows arise when the flow passes over the tip of the blade, be it at the hub or the casing, depending on the design of the blades. The detailed loss mechanisms depend on whether the blade is shrouded or unshrouded. The tip leakage flow can often have strong influence on the endwall loss (Denton, 1993).

2.2.3 Endwall losses

Endwall losses are also often referred to as secondary losses and can account for up to 50 % of the total pressure loss in a stage (Becz *et al.*, 2003; Sharma and Butler, 1986). Secondary losses are due to the annular boundary layer entering the blade row. Secondary losses are usually considered to be those losses that can not be accounted for otherwise (Denton, 1993). It should be noted that since the endwall losses are due to boundary layers they occur at both the hub and the tip of the blade.

2.3 Endwall loss and secondary flows

Much research over the years has gone into secondary flows in order to further the understanding of them. There is yet to be a prediction method that accurately predicts secondary flows (Langston, 2001). Most of the studies that have been performed have only dealt with planar or annular cascades with some studies concentrating on fundamental studies using cylinders (Belik, 1972). Sieverding (1985*a*) and Langston (2001) provide an in depth review of the literature on secondary flow investigations.

The first secondary flow vortex system as found in a linear cascade was first described by Hawthorne (1955). The inlet flow has an axis of vorticity that is perpendicular to the flow direction, which is caused by viscous effects. The inlet axis of vorticity is then deflected through a cascade. The passage vortex is due to the distortion of the vortex filaments of the inlet boundary layer passing with the flow through the curved passage (Sieverding, 1985*b*). Whereas the trailing filament vortex is caused by the spanwise or radial change in circulation.

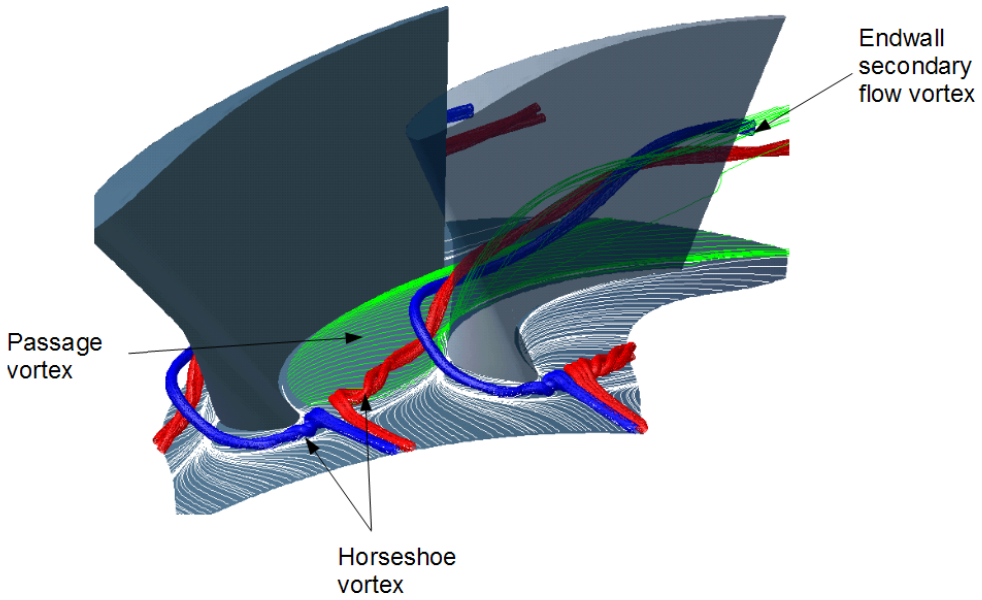

Figure 2.2: The main constituent flows found in endwall secondary flow vortex system, reproduced from Snedden (2011)

A horseshoe vortex is generated due to the inlet boundary layer impinging on the

leading edge of the turbine blade, as seen in Figure 2.2. The boundary layer flow has a lower stagnation pressure than the mainstream flow which causes a radial (spanwise in the case of cascades) pressure gradient on the blade leading edge. It is due to this radial pressure gradient that the flow tends to flow towards the endwall and wrap up around itself, forming a vortex which progresses around the leading edge of the blade forming the pressure side and the suction side legs of the horseshoe vortex (MacPherson and Ingram, 2010). The pressure side leg of the horseshoe vortex gets convected across the passage due to the cross passage pressure gradients. The pressure side leg gets caught up in the cross passage flow, forming the passage vortex. Langston *et al.* (1977) did some of the preliminary research that showed the evolution of the passage vortex through the blade passage. Schlienger *et al.* (2005) found that the blade wake then gets caught up in the endwall secondary flow vortex entraining the low momentum wake flow as shown in Figure 2.3, thereby reducing the momentum in the endwall secondary flow vortex structure further.

The passage vortex is the dominant secondary flow feature and has been reported by numerous researchers namely: Hodson and Dominy (1987*a*); Marchal and Sieverding (1977); Moore (1985); Moustapha *et al.* (1985) and Harrison (1990) to name a few. Quoting Gregory-Smith (1997), Ingram (2003) stated that the passage vortex is formed when a sheared flow is turned. The slower fluid follows a tighter radius of curvature, which leads to the tangential flow across the passage. In order to conserve continuity a vortical flow is generated. The cross passage pressure gradients act to strengthen the passage vortex thus a reduction in the pressure gradient delays the migration of the passage vortex (Ingram, 2003). Figure 2.4 gives an indication of how the various secondary flow features interact with each other (Ingram, 2003).

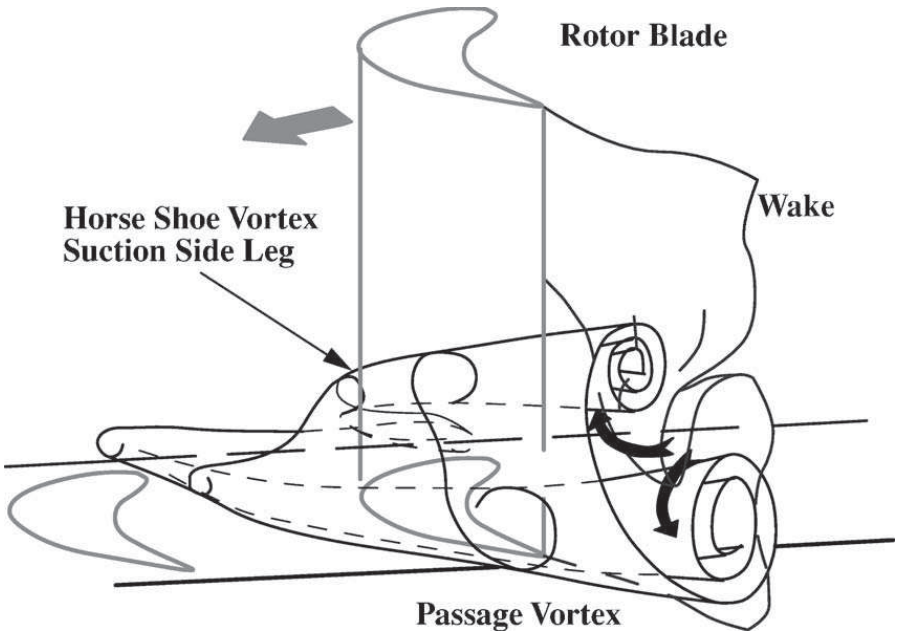

Figure 2.3: Roll up of the blade wake into the endwall secondary flow vortex (Schlienger *et al.*, 2005)

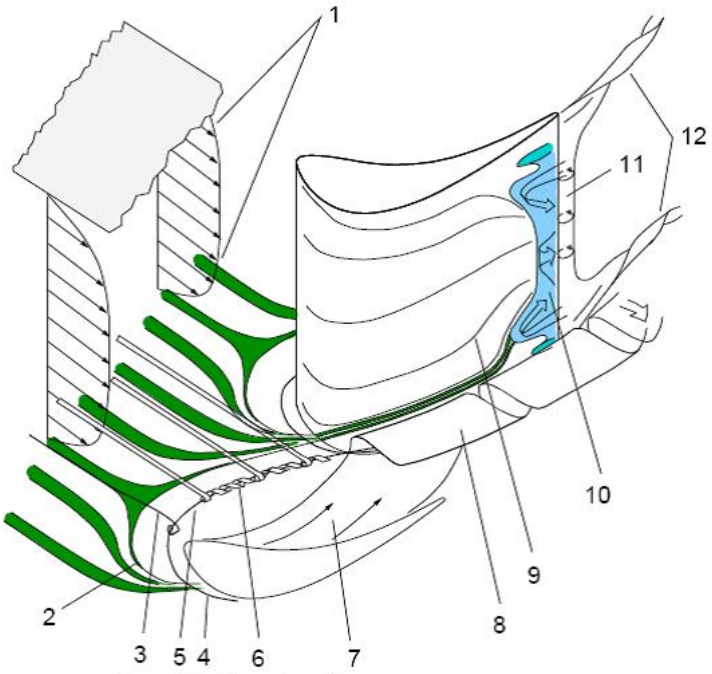

1: inlet boundary layer
2: separation line of the inlet boundary layer
3: horseshoe vortex core, inlet flow
4: suction side leg of horseshoe vortex
5: pressure side leg of horseshoe vortex
6: rolling up the inlet boundary layer
7: cross flow in the passage
8: passage vortex
9: motion of the suction side boundary layer
10: separation with backflow
11: eddying in the wake
12: trailing edge vortices

Figure 2.4: Schematic showing the various vortical structures in a turbine, Eymann *et al.* (2002) who reproduced it from Vogt and Zippel (1996).

In a rotating environment the inlet flow is skewed as it enters the rotor. This is because the boundary layer in the stator was developed on a stationary hub. As the boundary layer flow enters the rotor, the boundary layer gets skewed due to the change of reference frame caused by the rotating hub. The passage vortex gets further strengthened by this flow (Bindon, 1979, 1980; Boletis *et al.*, 1983; Walsh and Gregory-Smith, 1987).

2.4 Loss reduction mechanisms

Profile losses are caused due to boundary layer effects. Tip leakage losses can be reduced by reducing the size of the tip gap, or using a shroud. Shrouded blades, however, weigh more making a large decrease in the loss necessary to account for the weight increase. Secondary loss reduction therefore stands to produce the greatest benefit without a noticeable performance deficit.

There have been a large number of attempts to reduce the secondary flows, namely but not limited to:

- Profile aerodynamics, by means of aft loading.
- Radial variation in blade profile, such as lean or sweep.
- Making use of unsteady flow interactions.
- Utilisation of leading edge modifications.
- Endwall flow conditioning, such as endwall fences
- Axisymmetric endwall profiling
- Three-dimensional non-axisymmetric endwall profiling

2.4.1 Aft Loading

An aft loaded blade profile is one where the cross passage pressure gradient is the largest towards the trailing edge of the blade. Since the cross passage pressure gradient is the cause of the passage vortex, moving the maximum cross passage pressure gradient further back will delay the onset of the passage vortex. Therefore the flow leaving the rotor has a smaller passage vortex (Ingram, 2003).

2.4.2 Lean and sweep

The stacking line of a blade that exhibits lean does not leave the hub (or casing) radially (i.e. the blade "leans" tangentially when compared to a normal blade). Compound lean is a blade that exhibits lean at both ends of the blade i.e. at the hub and casing. A blade that has sweep has the leading edge line swept back axially. The major advantage of lean is that it reduces the velocity on one side of the blade at the endwall and increases it at the other. Overall lean does not directly reduce the overall loss co-efficient but the outlet angle deviations are reduced. The reduced outlet angle deviations mean that the outlet velocity profile and the loss distribution become more uniform (Harrison, 1989; Ingram, 2003).

2.4.3 Unsteady flow interactions

It has been found that up to 1 % relative efficiency difference can be obtained by changing the relative angle between the stator blades either side of the rotor (i.e. upstream and downstream) (Park *et al.*, 2006). The wake of the upstream stator gets mixed out with the rotor wake reducing the fluctuation of the instantaneous efficiency, about its mean value for a given period.

2.4.4 Utilisation of leading edge modifications

By using a large radius fillet between the blade surface and the endwall at the leading edge of the blade, some researchers have shown up to 1.5 % reduction in secondary flows (Langston, 2001; Muller *et al.*, 2002; Muller and Vogeler, 2005).

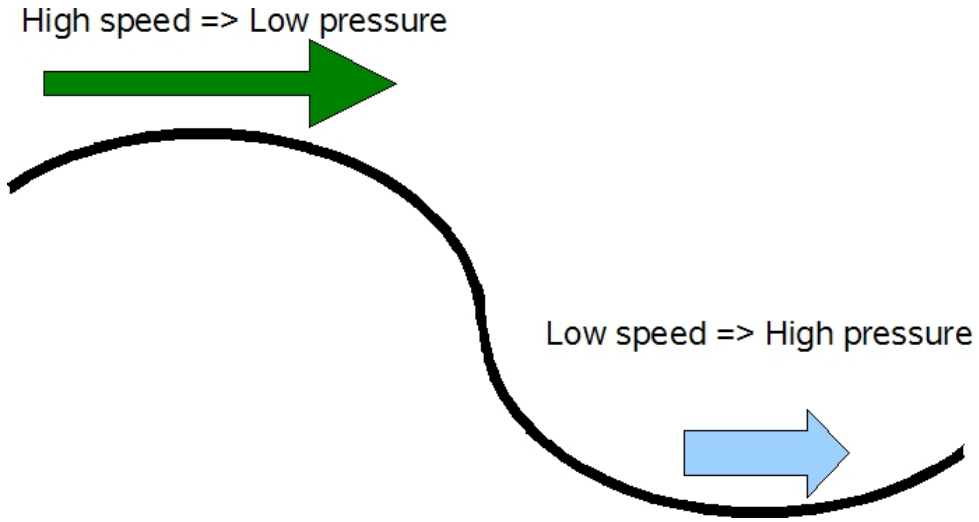

Figure 2.5: Basic principle of non-axisymmetric endwall contouring, recreated from Ingram (2003)

2.4.5 Endwall flow conditioning

Endwall fences control the boundary layer and reduce the streamwise vorticities, the secondary kinetic energy and the thickness of the loss region (Kawai *et al.*, 1989). Fences, however, are prone to degradation due to the temperature of the gas leaving the combustor.

2.4.6 Axisymmetric endwall profiling

Russian engineers first proposed the idea of axisymmetric endwall profiling, now known as a *Russian Kink*. The *Russian Kink* is an increase in the hub radius (reduction in cross sectional area) along the camber line. It has been found to improve performance by accelerating the boundary layer out the blade passage (Wang *et al.*, 1987).

2.4.7 Three dimensional non-axisymmetric endwall profiling

With improvements to manufacturing processes, it has become possible to machine endwalls having complex non-axisymmetrical profiles. Investigations into non-axisymmetric endwall contouring as a means of secondary flow control is starting to show favour by numerous researchers (Brennan *et al.*, 2001; Gregory-Smith *et al.*, 2001; Harvey *et al.*, 2002; Ingram *et al.*, 2003, 2002; Snedden *et al.*, 2009, 2007) to name a few. The main aim of non-axisymmetric endwall contouring is to alter the local static pressure such that the flow is either accelerated or decelerated, using the principle of streamline curvature as shown in Figure 2.5. By altering the local static pressure the endwall profile could then be strategically placed to reduce the endwall cross passage flow, hence reducing the secondary flows caused by it (Ingram, 2003). Atkins (1987) stated that the reduced cross passage pressure gradient was the reason for the improved performance when utilising a *Russian Kink*.

Viscous CFD, as well as computational power has progressed to a point where non trivial endwalls can be designed, optimised and evaluated in an automated fashion as described in MacPherson and Ingram (2010). CFD has progressed to a level where large complex analysis are possible, however, some aspects of CFD are still somewhat unreliable.

Harvey and Ramsden (2000) listed the properties available in CFD according to accuracy of the solution:

- Static pressure
- Mass flow and exit flow angle distributions
- Secondary flows
- Overall entropy rise
- Shocks and separations
- Local skin friction / heat transfer rates

Automated endwall design methods usually use some form of optimisation technique which would require an objective function. An objective function is a parameter, in this case a CFD variable, that is required to be maximised or minimised depending on the choice of variable used. Snedden *et al.* (2010*b*) listed the following variables as being some of the most commonly used:

- Rotor outlet angle
- Coefficient of secondary kinetic energy
- Helicity
- Pressure loss coefficient
- Rotor efficiency
- Stage efficiency

As can be seen, there are numerous variables to use and numerous objective functions are being utilised in the design of endwall contours. The spread in the choice of objective functions shows how little is known about secondary flow control by means of endwall contouring. Ingram (2003) even stated that even though endwall contouring has been introduced into real machines, the Trent 500 for instance (Brennan *et al.*, 2001; Harvey *et al.*, 2002), and have shown tangible performance improvements, little is known about how they actually work.

The current investigation is aimed at extending the current understanding of non-axisymmetric endwall contouring. Specifically the unsteady effects in a rotating $1\frac{1}{2}$ stage rotating turbine rig.

2.5 Unsteady effects

Even under steady state operation, where the engine is running at a constant speed with uniform inlet conditions, a turbine engine is inherently unsteady. The compressor and the turbine have alternating rows of stator and rotor blades which generate wakes and other secondary flows. These wakes and secondary flows are seen by the downstream blade row

as rotating about the machine axis relative to the current blade creating an oscillating flow. The wake flow has been shown to be composed of a von Karman vortex street which has votices shed from alternating surfaces of the blade (Cicatelli and Sieverding, 1996).

The wake can have a detrimental effect to the boundary layer in a turbine (Banieghbal *et al.*, 1996) causing early onset of transition. The location of transition is of great importance from a cooling point of view as the heat transfer characteristics change according to the state of the boundary layer (Dunn *et al.*, 2011*a*). The blade surface pressure is also affected which creates a fluctuating blade pressure profile which could potentially cause vibrations. The wake induces a slip velocity that has an effect on the blade incidence angle, creating off-design flow for some time (Hilditch *et al.*, 1996). The potential of these interactions increases with blade loading and more so when the effects of compressibility become important (Japikse, 1986).

In certain conditions the unsteadiness can improve the flow in a turbine. At low Reynolds numbers the wake can aid with boundary layer re-attachment (Banieghbal *et al.*, 1996). In turbines with repeating blade numbers the wakes can be lined up so as to coincide and thus reduce the amount of disturbed flow (Jouini *et al.*, 2003).

One of the concerns with endwall contouring is how will the endwall boundary layer be affected by the addition of the contouring. If the pressure field gets disturbed enough by the contour, separation could occur which would have a negative effect on heat transfer.

Chapter 3

Experimental Setup and Technique

This chapter details the experimental set-up and the technique used to evaluate the flow conditions. The instrumentation will be presented along with the process used to obtain the results.

3.1 Instrumentation and rig description

A schematic of the experimental test rig can be seen in Figure 3.1, with the relevant measurement locations shown in Figure 3.2. The experimental setup can be described as being a vertical axis $1\frac{1}{2}$ stage turbine test rig that makes use of a compressor to draw the ambient air in through the rig. The instrumentation used and the uncertainty of the individual components are listed in Table 3.1.

The compressor motor was frequency controlled, which allowed the compressor speed to be altered, making it possible to control the pressure drop across the turbine and therefore the inlet velocity. The inlet velocity, C_{inlet}, was used as a set point and was calculated using:

$$C_{inlet} = \sqrt{\frac{2(P_{total} - P_{static})}{\frac{P_{abs}}{RT}}} \tag{3.1.1}$$

Where the total pressure, P_{total}, was measured at $X0$ using a Kiel probe. A static pressure ring with three equidistant ports was used to obtain the average inlet static pressure, P_{static}. The density was obtained using $\rho = \frac{P_{abs}}{RT}$ and the measured inlet temperature and absolute pressure. The inlet temperature was measured at three equally spaced locations at the inlet ($X0$), then averaged. The absolute pressure was measured for the room (approximately 1.5 m below the inlet). By setting the inlet velocity in this manner allows the test rig to compensate for changes in atmospheric temperature and pressure.

The rotor speed was also used as a set point, in order to maintain a given incidence angle. A hydraulic dynamometer was used to regulate the rotor speed which was measured in conjunction with the torque. The dynamometer regulated the back pressure of the hydraulics, thereby imposing a resistance to the rotor and thus controlling the speed.

The signal which was used to determine the rotor speed was also used in order to phase lock the unsteady data. The speed pick-up in the Himmelstein torque transducer is comprised of a Hall effect sensor which detects the presence of 60 square cut teeth. The output was a sinusoidal signal, the frequency of which corresponds to the rotational speed of the rotor in RPM. The sinusoidal signal was then converted to a TTL step function such that there was one step per revolution. The rise of the step occurred at the 60^{th} pulse from the speed pick-up and lasted $5\mu s$. The rise occurred at the same rotor phase angle and was used as t_0.

Table 3.1: Experimental instrumentation and uncertainties

Primary Instrumentation		
Parameter	Instrument	Uncertainty
Torque	Himmelstein MCRT 28002T(5-2)CNA-G	±0.03Nm
Speed	+ Model 721 Mechanical Power Instrument	2RPM
Barometric Pressure	Siemens Sitrans P 7MF4233-1FA10-1AB6-Z A02+B11	0.075 % of full scale
Temperature	PT1000 RTD's	±0.05°C
Secondary Instrumentation		
Unsteady Flow Mapping	TSI Model 1240 Standard Cross Flow "X" Probe	±0.77 % mean velocity
Tangential Traverse	Custom cable system	Better than 0.01°
Radial traverse	Custom two component backlash free	0.01 mm
Yaw traverse	traverse driven by Cool Muscle® drives	0.1°

A custom built actuator was used to move the probe to various radial and yaw locations. The traverse could be connected to various axial locations in the rig (labeled $X1 - X4$ in Figure 3.1). Positions $X2 - X4$ reside on a tangential traverse drum which allows for different tangential positions to be measured. All traverse measurements in this thesis were measures at $X3$.

All unsteady data was acquired using TSI hotfilm measurement equipment, namely the IFA 300. Due to space constraints only cross flow probes could be used. The TSI $1240 - 20$ hot-film X-probe (shown in Figure 3.3) connected to a Model 1155 probe support was used for the measurements. The step function used to phase lock the data was sampled in addition to the hot-film signal.

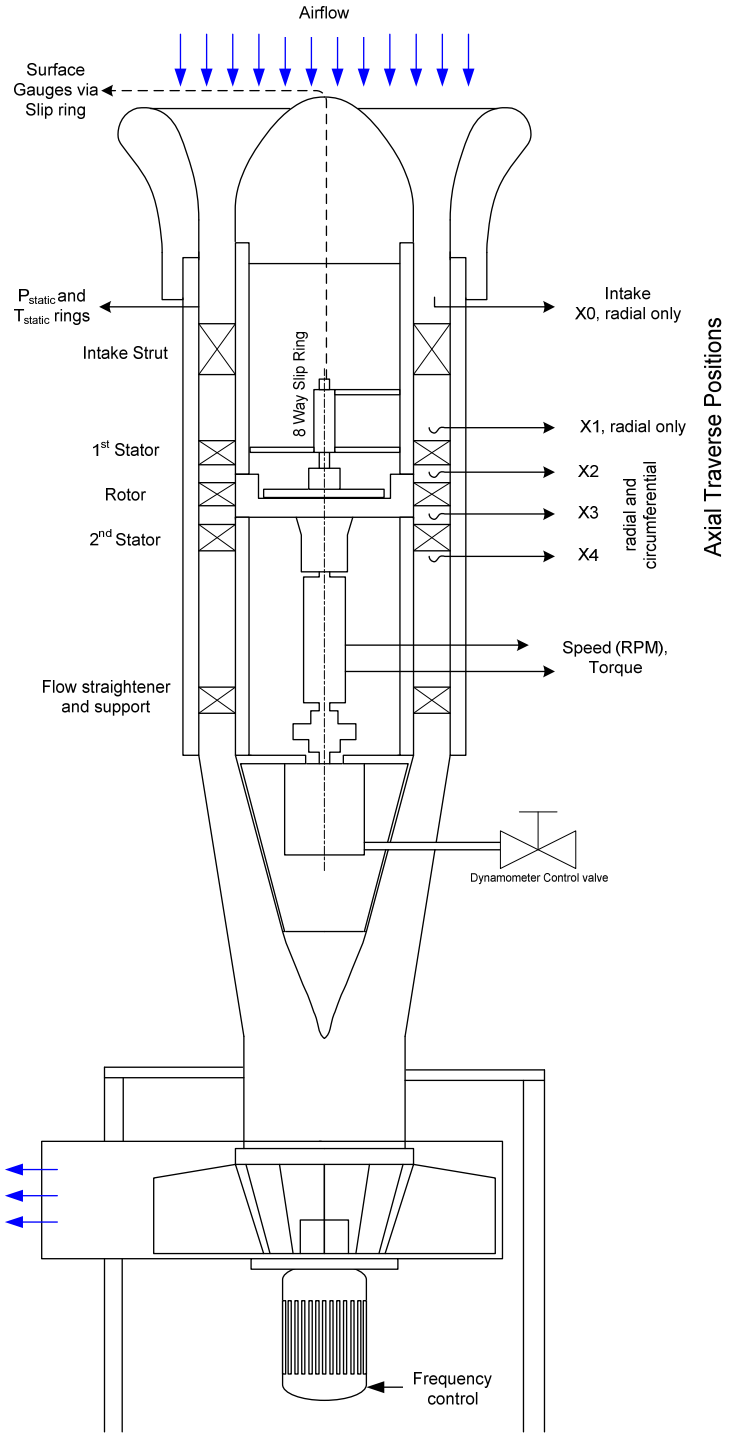

Figure 3.1: Schematic of the vertical $1\frac{1}{2}$ stage test rig, Snedden (2011)

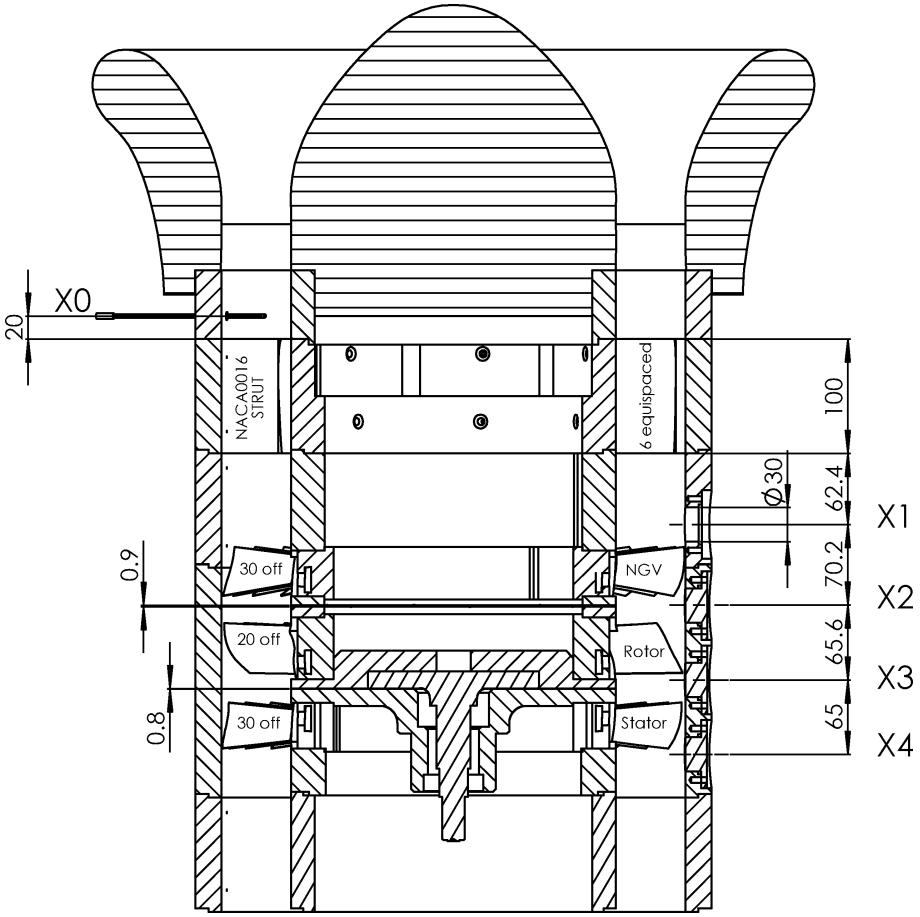

Figure 3.2: Rig schematic showing distances between items, Snedden (2011)

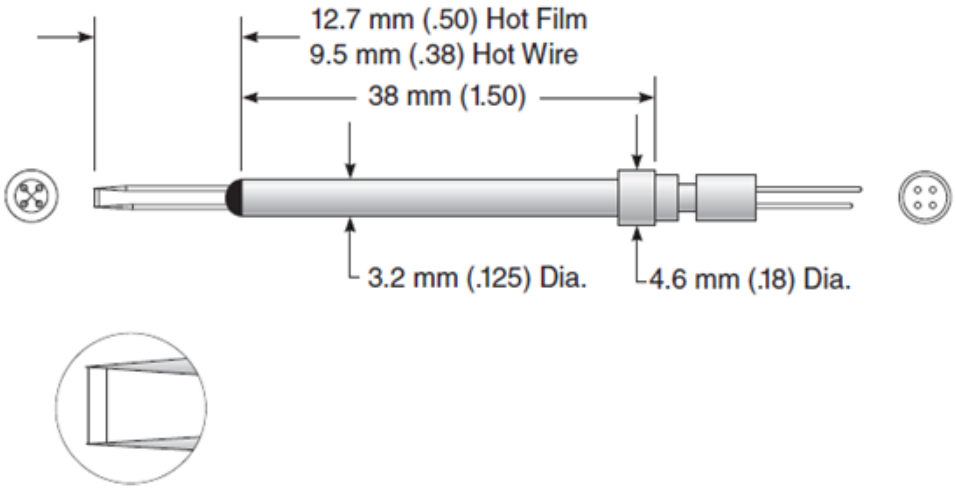

Figure 3.3: Dimensions of the TSI model 1240 – 20 X-probe

3.2 Blade and endwall description

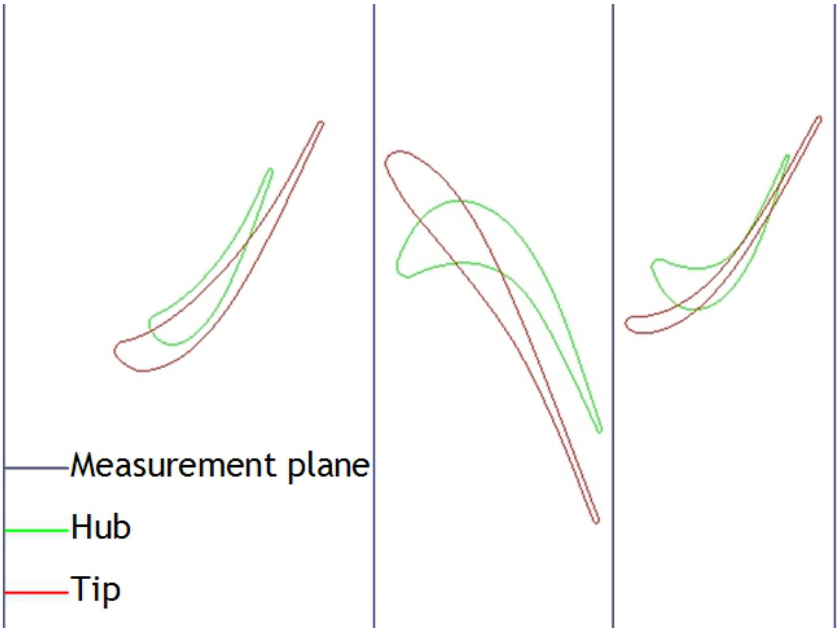

Figure 3.4: Hub and tip blade profile showing measurement locations, Snedden (2011).

The blading that was used was based on the cascade blading of Ingram (2003). In order to take rotation into account, blades were designed using the inverse design method of NREC (1972). The requirement that the hub profile be the same as used by Ingram (2003) was set to enable the use of a similar endwall contouring investigated by Ingram (2003).The resulting blade profiles can be seen in Figure 3.4. Design operating conditions used for the blade design are listed in Table 3.2. Table 3.3 shows the conditions to be tested with both the annular and contoured rotor.

The endwall contouring to be tested was an adaptation of the P2 endwall tested by Ingram *et al.* (2003), which can be seen in Figure 3.5. The P2 endwall contour showed the most promise of the endwalls. CAD representations of the blade profiles and the contouring can be seen in Figure 3.6,. The blade on the left is the blade on the annular endwall, and the blade on the right is the blade on the contoured endwall. In order to generate the blades, the casing profile was lofted to the hub profile (by linear interpolation). T-slots were used to locate the blades on the rotor ring, using retaining rings to prevent axial movement.

Table 3.2: Test rig design summary

Inlet		
Axial Velocity		21.38 m/s
1st Stator		
No. of Blades		30
Inlet Angle	Hub	0°
	Casing	0°
Outlet Angle	Hub	68.26°
	Casing	61.20°
Midspan Outlet Absolute Velocity		46.4 m/s
Rotor		
No. of Blades		20
Design Rotational Speed		2300 RPM
Blade passing frequency		766.7 Hz
Inlet Angle	Hub	42.75°
	Casing	−23.98°
Outlet Angle	Hub	−68.00°
	Casing	−71.15°
Flow Coefficient	Hub	0.625
	Midspan	0.52
	Casing	0.439
Stage Reaction	Hub	0.38
	Midspan	0.60
	Casing	0.70
Midspan Outlet Relative Velocity		57.4 m/s
Modified Stage Power		3.42 kW
Stage Pressure Ratio		1.0393
Exit Reynolds Number		127500
Zweiffel Coefficient (Zweifel, 1945) @ hub		0.94

Table 3.3: Experimental test conditions

Test Case	Rotor Speed (RPM)	Incidence Angle (°)	Rotor tested
Increased loading	1907	+5°	Annular
Increased loading	1907	+5°	Contoured
Design loading	2300	0°	Annular
Design loading	2300	0°	Contoured
Decreased loading	2820	−5°	Annular
Decreased loading	2820	−5°	Contoured

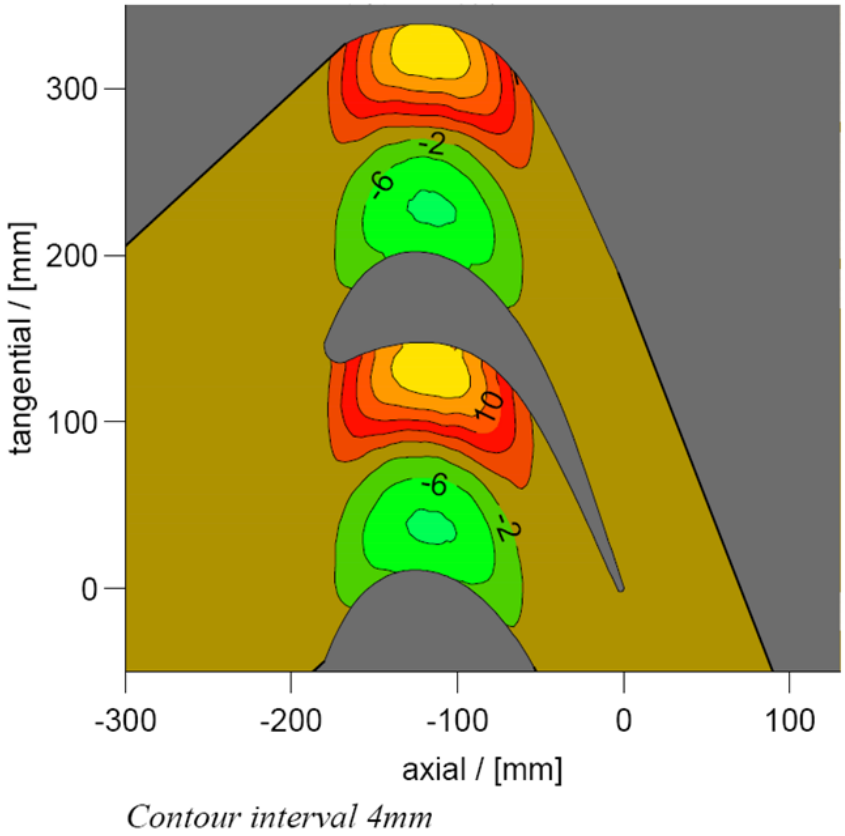

Figure 3.5: P2 endwall contour as tested by Ingram (2003)

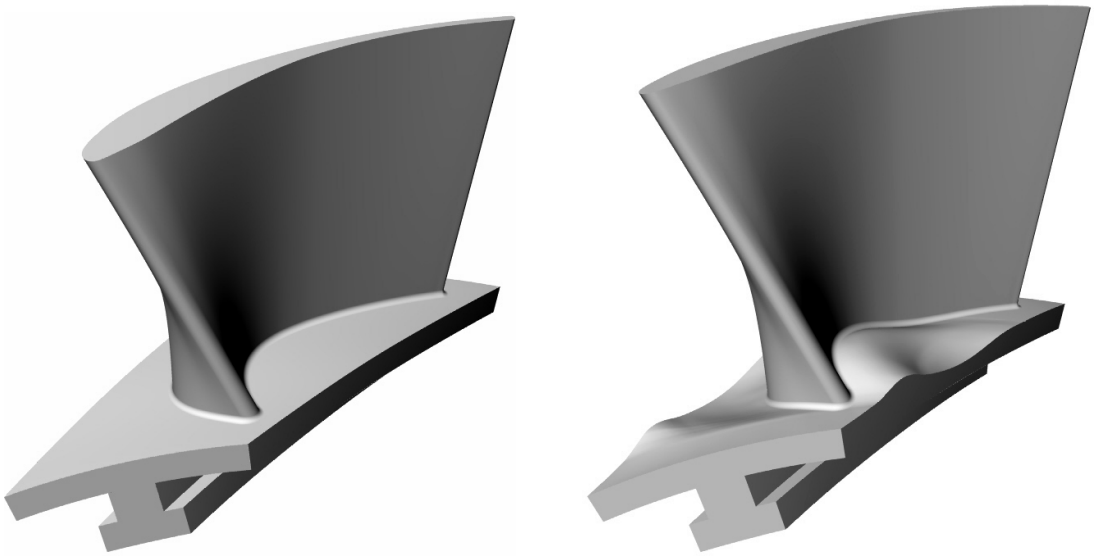

(a) Annular endwall (b) Contoured endwall

Figure 3.6: CAD representation of the rotor blades showing endwall contouring

3.3 Sample technique

3.3.1 Hot-film calibration and calculation

Calibration of the hot-films was carried out utilising the TSI Model 1129 auto calibrator. All calibrations were carried out using the prescribed method for dual cross flow sensors as described in TSI Incorporated (2003). The calibration range was from $C_{cal} = 0$ to $C_{cal} = 50m/s$, with the maximum expected velocity being approximately $C_{max} = 30m/s$. Calibrating to a velocity higher than expected allows sufficient room for unexpected flow features.

The velocity calculation method used by the ThermalPro software is presented below (TSI Incorporated, 2013). Firstly the bridge voltage of the hotfilm gets corrected to take changes in fluid temperature into account using the following relationship:

$$E_{B'} = E_B \left(\frac{T_s - T'}{T_s - T} \right)^2 \tag{3.3.1}$$

Where E_B is the bridge voltage as measured, $E_{B'}$ is the corrected bridge voltage, T_S is the sensor operating temperature, T is the fluid temperature and T' is the temperature during sampling. The corrected bridge voltage then has the calibration applied to it which converts the corrected bridge voltage to a velocity component (C_1, C_2 or C_3).

If the sensors are labeled "A" and "B" indicating perpendicular directions based on probe orientation then the effective velocity seen by each sensor can be represented by:

$$C_{A,eff}^2 = (C_1 cos\alpha_1 - C_2 sin\alpha_1)^2 + C_3^2 \tag{3.3.2}$$

$$C_{B,eff}^2 = (C_1 sin\alpha_1 + C_2 cos\alpha_1)^2 + C_3^2 \tag{3.3.3}$$

Where C_{eff} is the effective velocity, C_1, and C_2 perpendicular velocity components, and α is the angle between the velocity vector and the sensor axis. In the case of a two sensor probe C_3^2 is assumed to be negligible (in this case it would be the radial velocity (C_r).

Heating of the sensor film increases the rate of oxidation which in turn changes the resistance of the film (Perry, 1982). Increasing the resistance means that the calibration no longer holds. In addition to this the ambient air contains small molecules of dust. The dust can be seen in Figure 3.7, which shows the rotor blades after they have been tested. The dust particles erode the hotfilm as well, changing its properties even further. For this reason calibrations were performed before each sample set. Typically a sample set took less than two hours of continuous testing, reducing errors caused by sensor drift.

3.3.2 Sample grid

The sample grid consisted of 342 points, 18 in the tangential direction (1° increments from 31° to 48° in the rig co-ordinate system) and 19 in the radial direction starting at 3.5 mm from the endwall thereafter every 3.1 mm. The spanwise extent was from $S = 201.5$ mm to $S = 145.5$ mm which gave a clearance of 2.5 mm between the probe and the endwall.

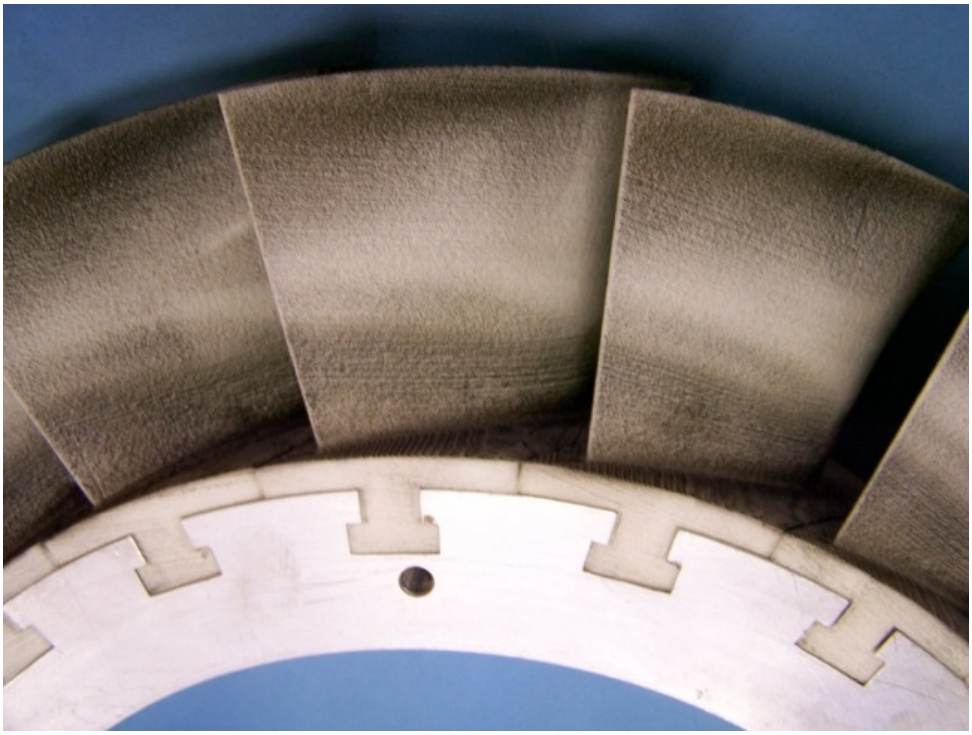

Figure 3.7: View of the suction surface of a tested rotor, showing dust deposition

Table 3.4: Spanwise distributions of the yaw angle offset used during testing

Span (%)	Probe Yaw angle (°)
Rotor Speed 1907 RPM	
5.74 - 26.1	50
31.2 - 66.7	30
76.9 - 97.5	0
Rotor Speed 2300 RPM	
5.74 - 26.1	50
31.2 - 66.7	20
71.8 - 97.5	0
Rotor Speed 2820 RPM	
5.74 - 21.0	10
26.1 - 76.9	0
82.0 - 97.5	-20

During initial testing it was found that the cone of acceptance of the probe did not always contain the flow field for all sample points. To account for this the probe was yawed so as to keep the flow in the cone of acceptance. The steady state absolute yaw angle was used as a reference for the offset of the probe used during testing. Table 3.4 shows the yaw angles used during testing for each of the rotor speeds.

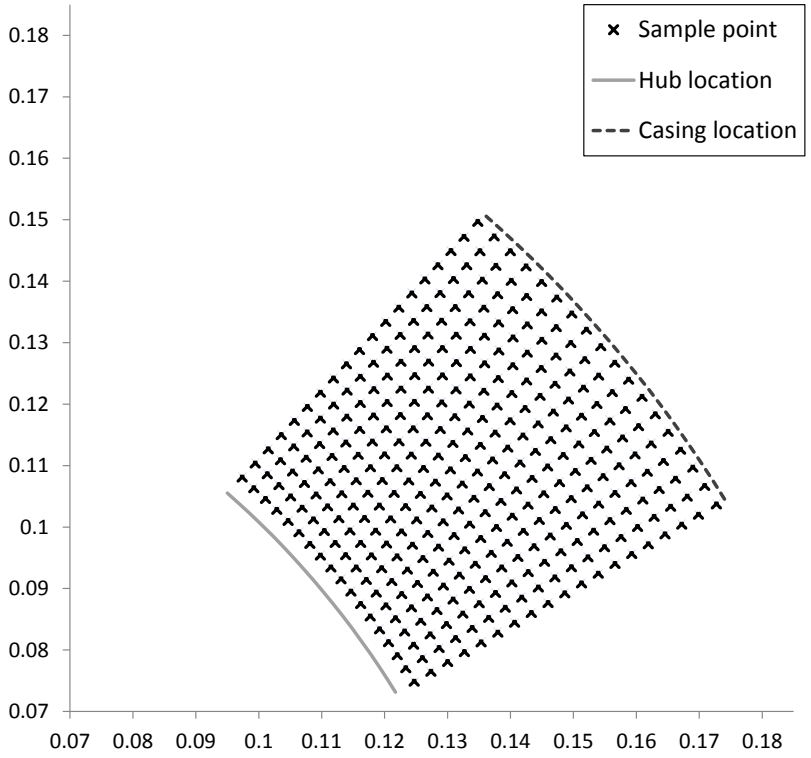

Figure 3.8: Sample grid used for hotfilm measurements

3.3.3 Sample settings

King's Law (TSI Incorporated, 2003) was used to relate the calibrated values to the measured values as it consistently produced the lowest Mean Square Error, as calculated by the ThermalPro software supplied by TSI for use with the IFA300. Prato *et al.* (2002) found that King's Law gave excellent agreement between five-hole probe data and time-averaged hot-film data.

Unsteady sampling was carried out using the settings displayed in Table 3.5. Filtering was not done via the IFA300's low pass auto filtering capability, but instead it was software filtered allowing for more control. The ThermalPro software (TSI Incorporated, 2000) was set to perform temperature correction using a TSI supplied general purpose T-type thermocouple.

Sample frequency per channel	$100kHz$
Number of samples per channel	65535
Calibration Curve fit	King's Law

Table 3.5: Sample settings

3.4 Data processing and handling

After sampling, the data is in a binary file format which contains voltage data. ThermalPro was used to convert this data into velocities using the calibration curves as well as temperature data. The resulting ASCII text file contains four columns of data. The first column contained the time stamp of each sample using the sample start time as a reference. The next column contains the calibrated corrected axial velocity followed by the calibrated corrected tangential velocity. Finally, the last column contains the trigger signal used for phase-lock averaging (PLA).

Before any processing occurs, the data was checked for statistically improbable data or outliers. Chauvenet's criterion (Coleman and Steele, 1989), was used to determine if a data point was spurious or not. The criterion states that any value that exceeds five times the standard deviation from the mean is improbable (probability of measured value being less than $6e-7$). This was done to remove those values points which violated the calibration or were spurious. If the measured point does not satisfy the calibration equations they were assigned approximately -1 m/s as a value by the ThermalPro software. The average of the two surrounding points was used to replace the removed spurious value in order to ensure that the phase was not affected by data removal. Thus the number of samples was kept constant. It was found that the number of points removed was less than 0.5 % of the total, with the majority being found closest to the endwall.

Using the method of Perlman and Auerbach (1977), the data was phase lock averaged (PLA) in order to reduce the magnitude of random fluctuations inherent in discretely sampled data. PLA was performed by parsing (read in and sort the data into its components) the data using the first rise in the sampled step function. All the parsed portions were then grouped according to the number of sample points per revolution. The group with the largest number of parsed portions was used and the other groups were discarded. It was the largest group that was phase lock averaged. Inspection showed that there were at least eight revolutions used to average each grid point. The result was an averaged data set that consisted of exactly one revolution of the rotor as specified by the step function.

After PLA, the data was such that at each point on the grid the data was for the rotor being in the same relative location with respect to the sample point i.e. the first rise in the step function. Thus the rotor phase angle had to be adjusted in order to make it such that for each point the rotor was in the same absolute location. The adjustment was calculated according to the tangential location of the sample point. A sawtooth was generated such that one wavelength corresponded to one blade passing. Thus the sawtooth could be used to adjust the rotor phase angle since the starting value would be dependent on the measurement location. The phase alignment was then done by aligning the sawtooth of each point.

The velocity magnitude was calculated as follows:

$$C_{mag} = \sqrt{C_x^2 + C_t^2} \tag{3.4.1}$$

Where C_x is the axial velocity, and C_t is the tangential velocity. C_r could not be measured with the probe used, and was considered to be small. The measurements used

for (but not presented in) Snedden (2011) showed that the average radial velocity was less than 1 m/s The yaw angle, α, was calculated as:

$$\alpha = atan(C_x/C_t) + offset \tag{3.4.2}$$

Where $offset$ was the offset angle (shown in Table 3.4 of the probe for the current sample point. The secondary velocity (C_{sec}) was taken to be that component of velocity that deviates from the mean bulk flow using the method of Matsunuma (2006).

$$C_{sec} = C_{mag} * sin(\alpha_{sec})/\overline{C}_{mag} \tag{3.4.3}$$

Where $\overline{C}_{mag}$ was the mean bulk velocity and α_{sec} was defined as

$$\alpha_{sec} = \alpha - \overline{\alpha}_{design} \tag{3.4.4}$$

$\overline{\alpha}_{design}$ was the mean design rotor outlet yaw angle. Design outlet yaw angle for rotor and stator respectively was defined as:

$$\alpha_{R-design} = -944.523S^2 + 187.756S + 22.4063 \tag{3.4.5}$$
$$\alpha_{S-design} = -132.846S^2 + 161.535S - 86.5147 \tag{3.4.6}$$

Where S was the span in mm measured from the machine axis. The relative velocity, W and relative yaw angle β were also calculated, shown in Equation 3.4.7 and Equation 3.4.8 respectively.

$$W = \sqrt{(U + C_t)^2 + C_x^2} \tag{3.4.7}$$
$$\beta = acos(C_x/W) \tag{3.4.8}$$

The grid data had to be converted to Cartesian co-ordinates from the polar co-ordinates that were used for measurement. Once the grid was converted, the data was arranged into a format that Tecplot (Tecplot Inc., 2008) could read. The data was also radially and tangentially averaged and each written to a separate file for use in averaged plots.

Fast Fourier Transforms (FFT) were processed from the raw data (IFA300 output, all 65536 samples) instead of the PLA data thus maintaining data that might have otherwise been eliminated by the averaging technique, such as rotating distortions. Ambient noise would be constant and present in both annular and contoured data sets. The data was used such that the first and last data points were in phase. The FFT's were then azimuthally averaged allowing for radial changes to be seen.

Once the data was in the Tecplot format, scripts were used to replicate the current view for each time step so as to get plots that were consistent in range size and location regardless of timestep or input test case.

3.5 Repeatability

A repeatability study was performed in conjunction with the tests to determine applicability of the yaw angles in Table 3.4. A radial traverse was performed using the same spacing as used for the area traverse, except only the center line was sampled, 40°. The results can

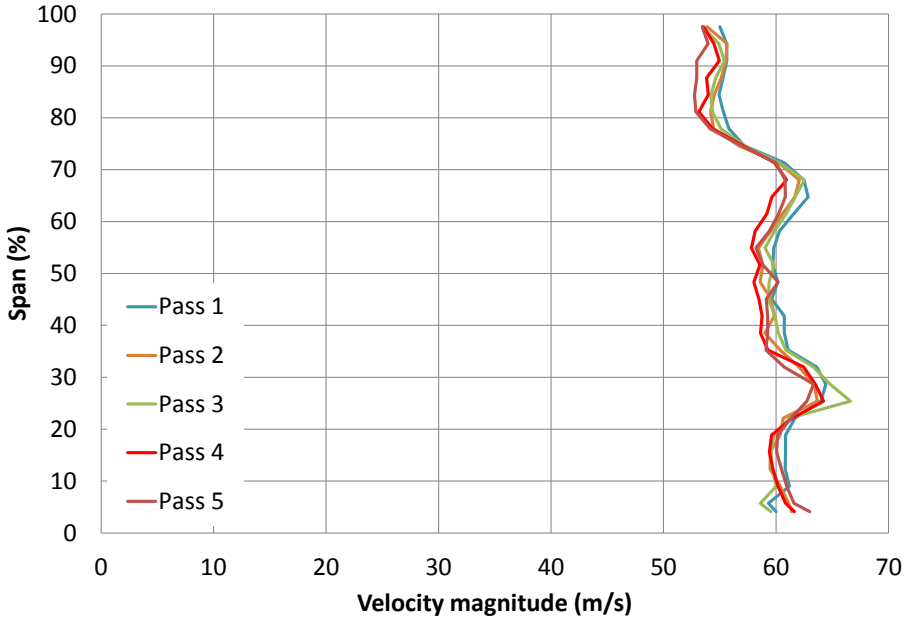

Figure 3.9: Linear traverse relative velocity magnitude at rotor exit

be seen in Figure 3.9. It can be seen that in general the results correlate well with each other. It should also be noted that due to only one radial line being sampled, the results are slightly different to those in Chapter 4.

Chapter 4

Experimental Results

The results in this section comprise the unsteady investigation that was performed as described in Chapter 3. Initially the unsteady results are compared with the steady state results that were presented by Snedden (2011). The author performed the experiments for Snedden (2011) as part of a larger investigation. Then the time averaged as well as the time averaged, azimuthally averaged results are presented. The FFT results of the time averaged, azimuthally averaged data is also presented. The last set of results is presented in the form of velocity triangles. Finally a discussion and conclusions of the experimental results are provided.

As discussed earlier, the following conventions hold in this chapter. Steady state results refer to the 5 hole probe results, and unsteady results refer to those results obtained by the hotfilm probe. Where measurement technique has been omitted, unsteady state measurement is implied.

4.1 Comparison to steady state results

4.1.1 Design Condition

The most striking observation was that there was a larger difference between steady and unsteady measurements than found between annular and contoured rotor exit flow fields. The absolute yaw angle in Figure 4.1 shows reasonable correlation between the steady data to the unsteady data. The discrepancies, however, can be attributed to the difference in measurement technique. The steady state data was sampled at only three azimuthal co-ordinates (31°, 40°, 49°) and averaged (Snedden, 2011). The unsteady data, however, was sampled at 18 azimuthal locations (from 31° up to and including 38°). Thus not all of the flow features caused by the stators that propagated through the rotor were captured by the 5 hole probe.

Another cause of the discrepancy between the steady and unsteady data sets was the measurement technique used to measure the steady yaw angle. The yaw ports of the 5 hole probe were connected to the positive and negative terminals of a partial differential pressure transducer, thus making it possible to null yaw the probe. Typically the static pressure for a 5 hole probe is calculated by averaging the four outer ports (pitch and yaw ports). The steady state static pressure was calculated by averaging the pitch ports only since the yaw ports were not measured with respect to atmosphere. A downside of this connection method, however, is that in highly sheared flows the results can be unreliable

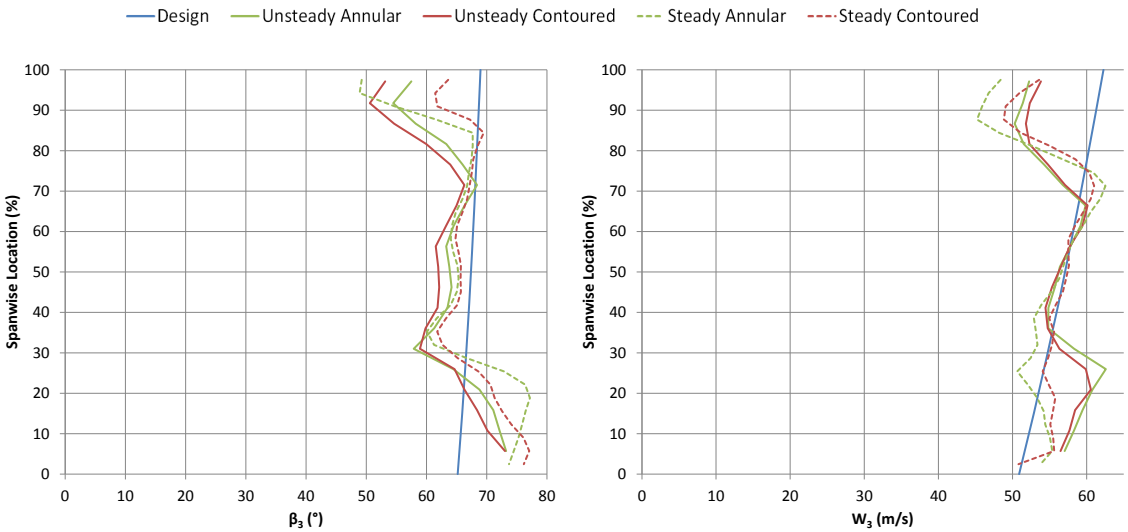

(a) Rotor exit relative yaw angle

(b) Rotor exit relative velocity magnitude

Figure 4.1: Design Case: Comparison of steady state to unsteady measurements

(Van Den Berg and Bertelrud, 1988). This is due to the influence of the tangential velocity on the static pressure not being captured. In general, due to the size of the 5 hole probe the average of the pitch ports was sufficient. However, in the endwall secondary flow and tip leakage regions where shear dominates the flow, it does not quite capture the velocities there. The unsteady data however, measures the tangential velocity directly and was felt to be more accurate.

The endwall secondary flow region as shown in the rotor exit relative yaw angle (Figure 4.1a) for the unsteady measurements was lower than that of the steady state data. The peak in relative yaw angle at 20 % span in the steady state annular data was not captured by the unsteady data set. The steady data measured the tip leakage under turning (based on rotor exit relative yaw angle) to be less than that of the unsteady data, but the magnitude of the annular data set was comparable.

The rotor exit relative velocity profiles compare reasonably well, however, below 40 % span the steady and unsteady results do not show the same trend. The reason for the difference is due to the difference in yaw angle as well as the velocity magnitude. The steady relative velocity also contains the radial component which was unavailable in the unsteady data set. The rotor exit relative velocity profile highlights yet again the difference in the ability of the two measurement techniques to capture the velocity in regions of highly sheared flows.

4.1.2 Increased Loading Condition

As with the design case the correlation of the relative yaw angle measurements in Figure 4.2 was found to be acceptable. The worst correlation was found to be at the tip (casing) which has high shear flow. The annular rotor tip regions show the same shape, but the steady data predicts a much steeper gradient. Despite the steeper gradient the location of the peak relative yaw angle corresponds well. It is expected that the contoured steady data was not very reliable in the tip region as the trend was different from all other measurements.

The relative velocity correlates better than the relative yaw angle. The steady and

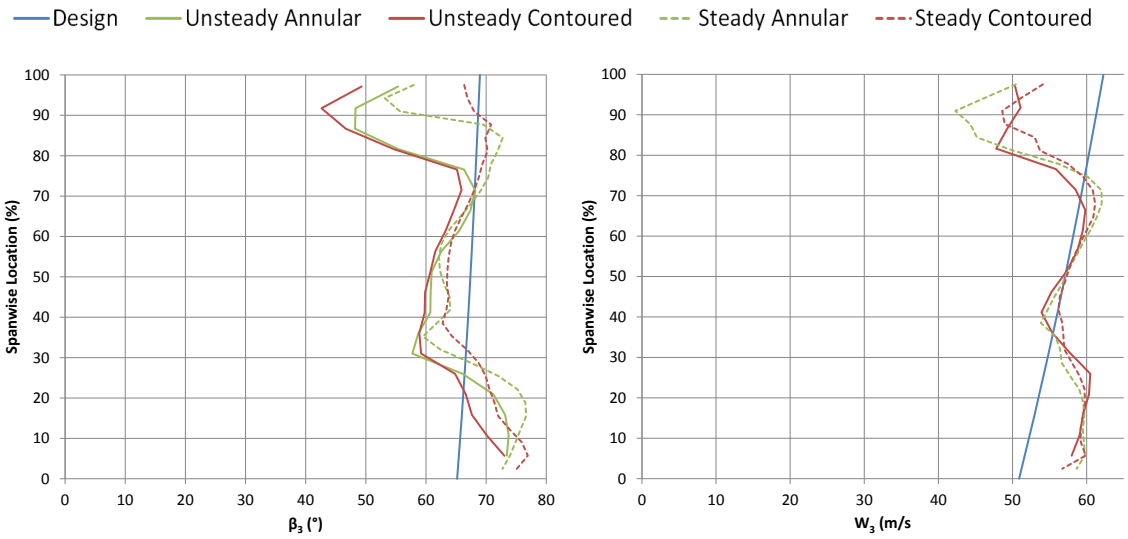

(a) Rotor exit relative yaw angle (b) Rotor exit relative velocity magnitude

Figure 4.2: Increased Loading Case: Comparison of steady state to unsteady measurements

unsteady data follow the same trends with the flow features being in the same place and the inflection points being approximately the same. The differences between annular and contoured also carry over well considering the increased turning due to the increased loading.

4.1.3 Decreased Loading Condition

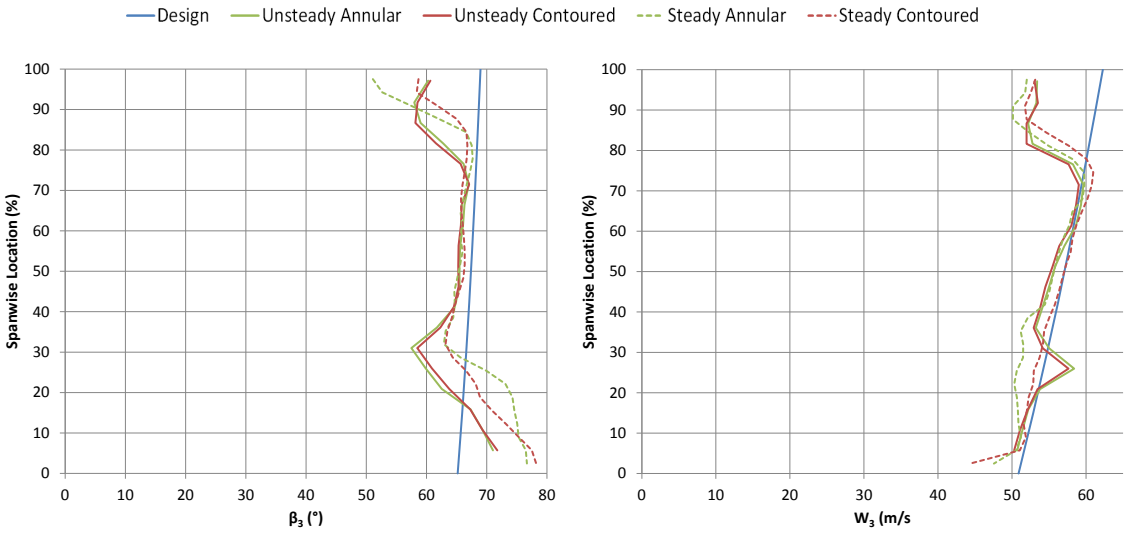

(a) Rotor exit relative yaw angle (b) Rotor exit relative velocity magnitude

Figure 4.3: Decreased Loading Case: Comparison of steady state to unsteady measurements

Figure 4.3 shows the decreased loading comparison of the unsteady and steady data

sets. Of all the loading cases it follows the design the best over the largest span, as is to be expected due to the reduced amount of work extracted from the flow and thus the reduced turning in the flow. The difference observed between steady annular and contoured was not captured in the unsteady data, however, Snedden (2011) felt that his data set here was erroneous which was confirmed by the unsteady measurements. The gradient of the unsteady rotor exit relative yaw angle was steeper at 40 % span resulting in a lower value due to the endwall secondary flow vortex structure at 31 % span. This results in a peak in the relative velocity magnitude at 25.9 % span. It was originally thought that the change in the probe yaw angle be as discussed in Chapter 3 (shown in Table 3.4 was the cause of this, but the yaw angle change of 10° is done at 21 % span (thus the peak seen did not occur at the change, but after it). The data point at first glance would appear incorrect, but the gradient before and after the peak suggest it is correct. The unsteady measurements for both the annular and contoured rotors were repeated twice to verify the peak and it was present in both repeated data sets (as well as the numerical results presented later).

4.2 Unsteady results

As in Dunn *et al.* (2013) both time averaged and time averaged, azimuthally averaged data sets are presented in this section. The time averaged plots constitute the contour plots to the left of Figure 4.4 to Figure 4.21. The area of the contour plot has been extended to include the hub and the casing. The value for these regions was set to 0 (to satisfy zero velocity on the wall).

The plots on the right constitutes the time averaged, azimuthally averaged data spanning from hub to casing. The horizontal error bars at each spanwise location indicate the range of velocities measured (i.e. minimum and maximum velocity measured). The FFT's have been plotted on the same plot to indicate the frequencies of interest of the corresponding sample locations. The FFT plots use the secondary X-axis at the top of the plots, which is in multiples of blade passing frequency (with 1 being the blade passing frequency, shown in Table 4.1). The FFT scale can be seen on the bottom right of the plot as a vertical line representing 1 m/s.

Table 4.1: Blade passing frequency for the three speeds tested

Loading Condition	Rotor speed	Blade Passing Frequency
-	RPM	Hz
Increased Loading	1907	635.7
Design Loading	2300	766.7
Decreased Loading	2820	940

4.2.1 Design condition

The time averaged, azimuthally averaged tangential velocity plots in Figure 4.4 and 4.5 show a reasonable correlation with the design tangential velocity at mid-span, while the tip and endwall flows have a poor correlation due to the tip leakage and endwall secondary flow structures. The deficit in velocity in the tip region (above 70 % span) was due to the relatively large tip gap allowing the flow through more axially aligned. In the endwall

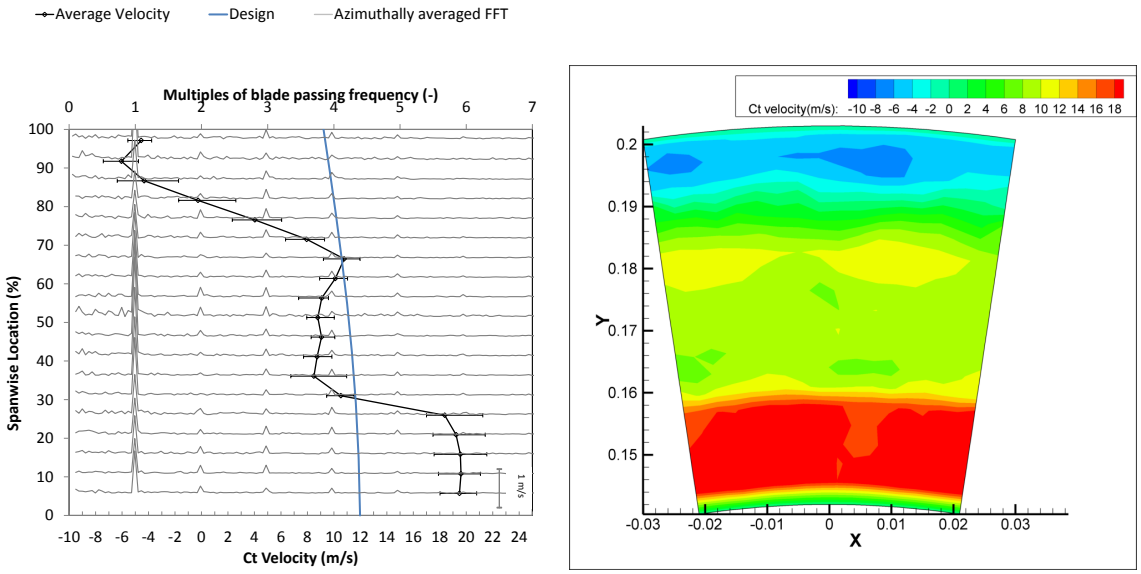

(a) Area averaged profile, with FFT (b) Time averaged contour

Figure 4.4: Design case, annular rotor: Tangential velocity downstream of the rotor

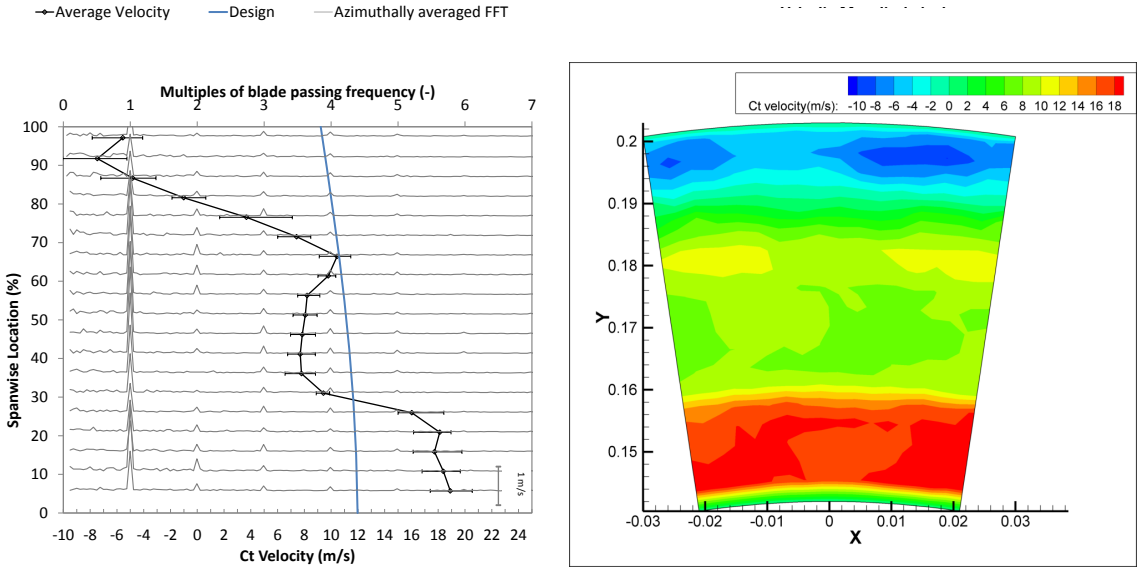

(a) Area averaged profile, with FFT (b) Time averaged contour

Figure 4.5: Design case, contoured rotor: Tangential velocity downstream of the rotor

region (below 30 % span) the increase in tangential velocity was due to the presence of the endwall secondary flow vortex structure.

When comparing the endwall secondary flow structure in 4.4 and 4.5, it can be seen that the magnitude has been reduced at 18 % span by the contoured rotor with a subsequent decrease in the velocity variation. This was indicative of a reduction in the strength of the endwall secondary flow structure. The midspan region also showed a reduction in the oscillating component of the flow, which resulted in a smaller range of incidence angles

seen by the downstream stator row.

The tip leakage flow, however, showed an increase in strength with the peak value being further away from the design (ideal) value, indicative of a higher loss. The velocity fluctuations were also increased.

Looking at the time averaged contour plots it can be seen that the area of the peak value of tangential velocity at the endwall is reduced for the contoured case. The tip leakage flow was also increased with the velocity containing another contour level. The magnitude was changed, as well as the azimuthal extent. However, the spanwise extent remained the same with the turning point for both cases occuring at 67 % span. The overall structure in the midspan flow was also changed, with the annular case matching the design better at midspan.

The axial velocities in Figure 4.6 and 4.7 show a similar trend. The contoured rotor has reduced the intensity of the endwall secondary flow region while at the same time increasing the tip leakage flow. As seen for the tangential velocity, the magnitude of the axial velocity oscillations was reduced.

Something not seen in the tangential velocities is the redistribution of the high momentum flow of the endwall secondary flow region in the spanwise direction. The spanwise distribution in flow has thus been made more uniform. This can be seen in Figure 4.8 and 4.9 where the velocity magnitude of the endwall secondary flow system was drastically reduced.

The redistribution of the high momentum flow is due to the change in the vortex structure due to the contoured endwall. The vortex structure is less tightly wrapped so the midspan flow is strengthened instead of the endwall secondary flow system. The CFD results in Chapter 6 give a better representation of the unwrapped vortex system and will be covered in more detail there.

4.2.2 Increased Loading condition

The speed of a turbine with increased loading is less than that of the ideal case. The increased loading causes the flow through the turbine to perform more specific work. Thus there is an increase in the flow turning (to increase the momentum change in the flow which results in an increased torque). As discussed earlier, some of the endwall secondary flow vortex is due to the curling up of the boundary layer of the turned flow to enable rotational momentum to be conserved. Therefore the results for the turbine with increased loading should show evidence of increased endwall secondary flow. Figure 4.10 and 4.11 show the increase in turning that occurs in the increased loading case, shown as an increase in the tangential velocity. The peak tangential velocity of the annular case increasing by $8m/s$, while the contoured case increases by $7m/s$.

The contoured rotor had a lower peak tangential velocity in the endwall secondary flow region by $1.7m/s$, however, at 20 % span the reduction was $2.7m/s$. The small reduction close to the endwall was due to the boundary having a tangential velocity close to that of the wheel speed ($U = 28.2m/s$) at 0 % span.

The axial velocity plots (Figure 4.12 and 4.13) show a much weaker (by approximately $2.5m/s$) endwall secondary flow structure for the contoured case. As with the design case the magnitude of the fluctuations was also reduced. The axial velocity below 20 % span was improved with the gradient being less extreme.

Looking at the contour plots, it can be seen that the contoured endwall redistributes the high momentum flow in the endwall secondary flow region in the spanwise direction

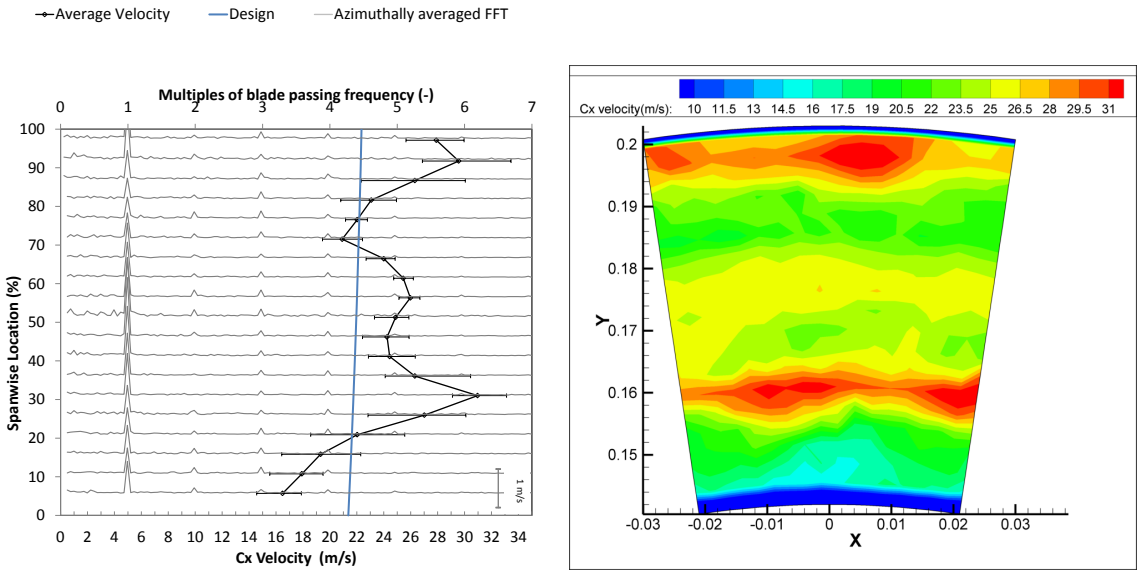

(a) Area averaged profile, with FFT (b) Time averaged contour

Figure 4.6: Design case, annular rotor: Axial velocity downstream of the rotor

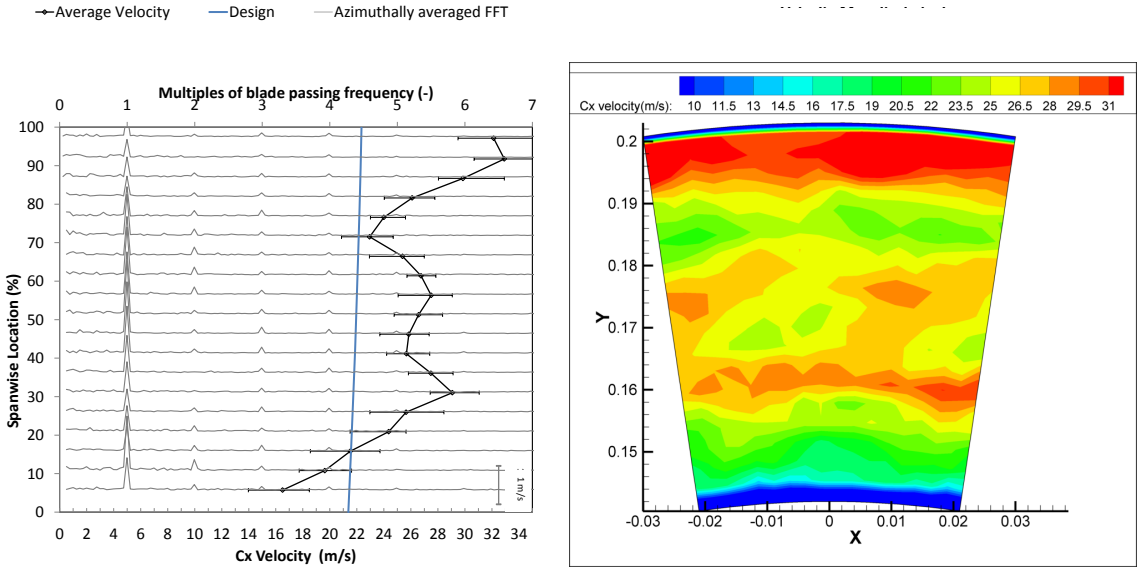

(a) Area averaged profile, with FFT (b) Time averaged contour

Figure 4.7: Design case, contoured rotor: Axial velocity downstream of the rotor

both toward the endwall and towards the blade tip. As seen in previous results the tip leakage flow was again affected.

The velocity magnitude results in Figure 4.14 and 4.15 did not show anything significant not already covered. The endwall secondary flow vortex was again reduced in strength by the contouring. The energy was then redistributed in the spanwise direction. The magnitude of the oscillations was reduced. The increase in tip leakage flow of the contoured rotor was more evident.

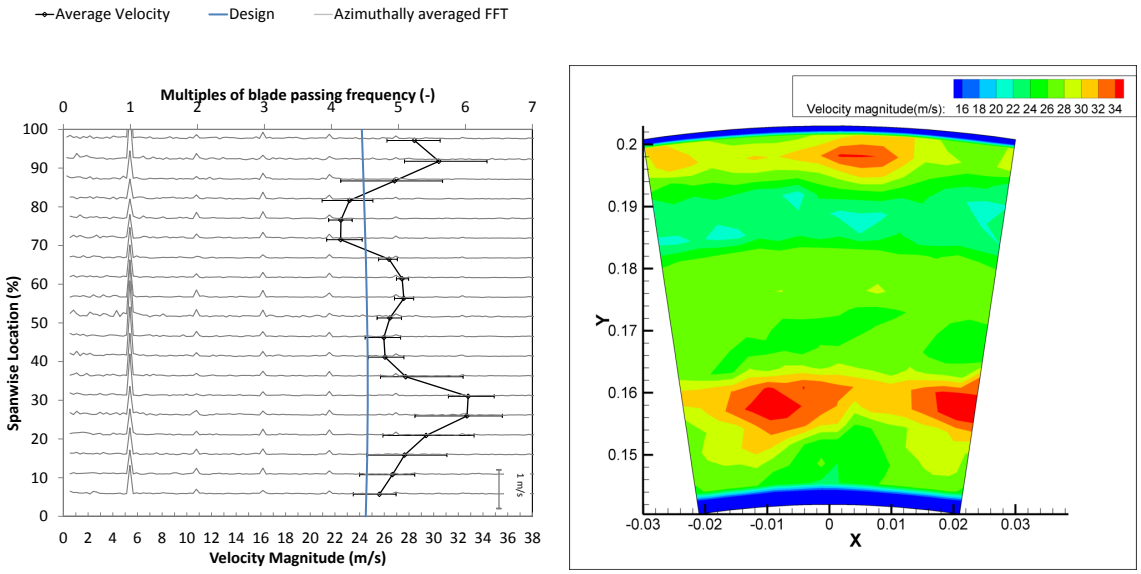

(a) Area averaged profile, with FFT (b) Time averaged contour

Figure 4.8: Design case, annular rotor: Velocity magnitude downstream of the rotor

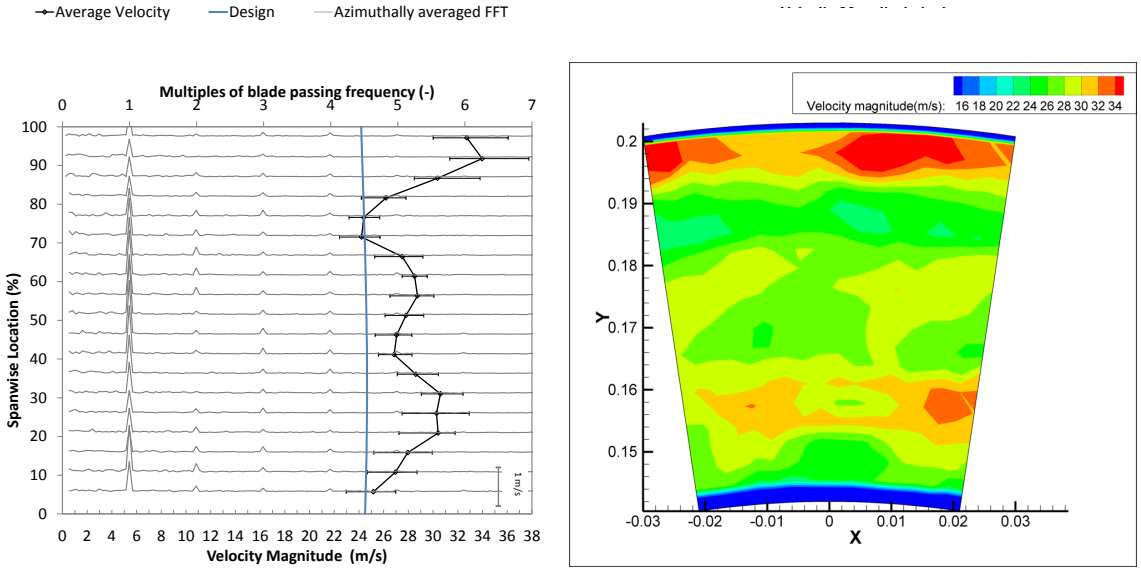

(a) Area averaged profile, with FFT (b) Time averaged contour

Figure 4.9: Design case, contoured rotor: Velocity magnitude downstream of the rotor

The FFT did, however, reveal that the magnitude of the wake (magnitude of the FFT at the blade passing frequency) was increased in the endwall secondary flow region. The increase can be explained by looking at the contour plots. With the vortex core less tightly wrapped around itself, and more open in the spanwise direction; a more distinct wake was measured. Thus the change between peak values was larger.

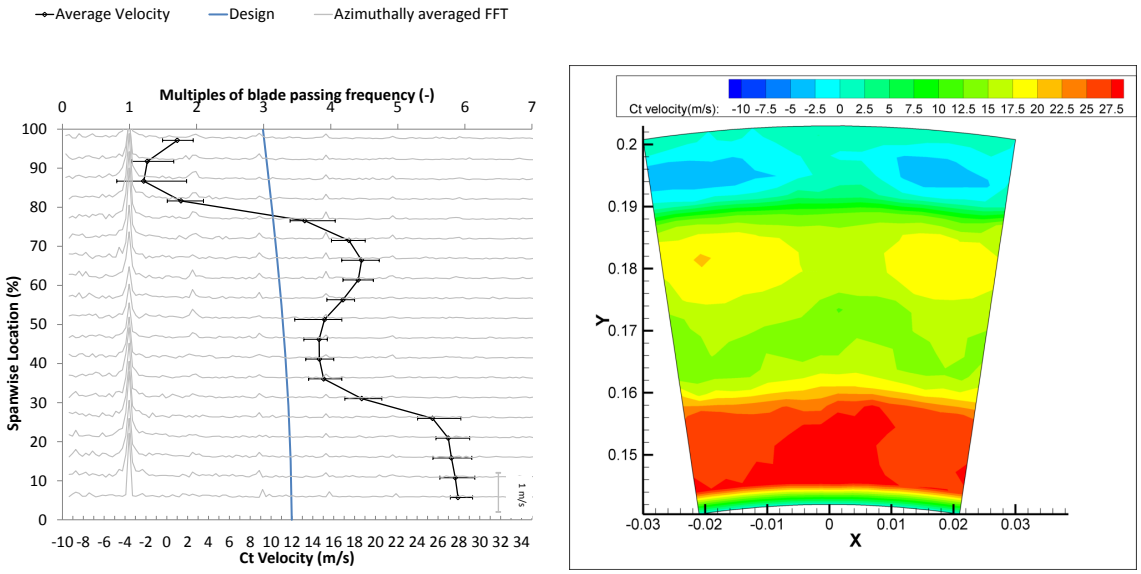

(a) Area averaged profile, with FFT (b) Time averaged contour

Figure 4.10: Increased Loading case, annular rotor: Tangential velocity downstream of the rotor

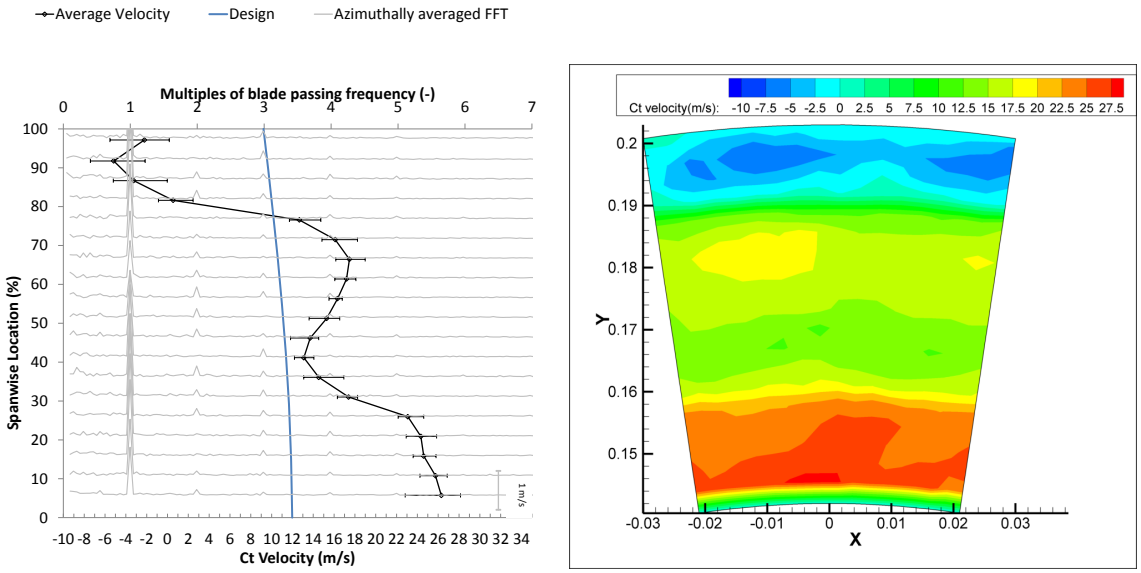

(a) Area averaged profile, with FFT (b) Time averaged contour

Figure 4.11: Increased Loading case, contoured rotor: Tangential velocity downstream of the rotor

4.2.3 Decreased Loading Condition

The decreased loading condition caused the turbine to rotate faster than the design condition. The resulting tangential velocity was thus lower than that of the design condition, which was indicative of lower turning of the flow. Since the flow was not turned as much

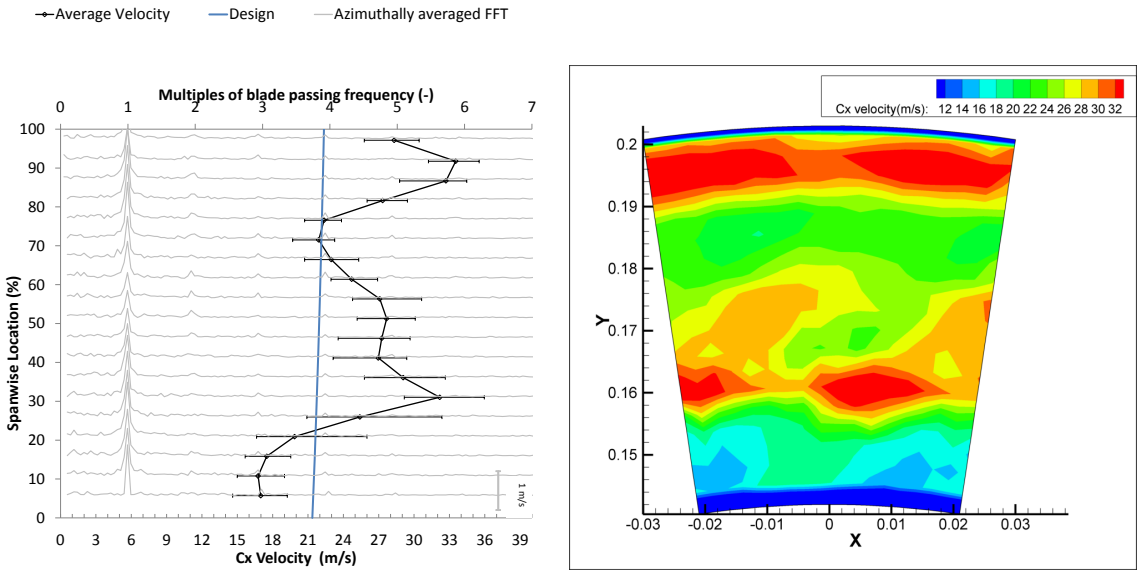

(a) Area averaged profile, with FFT (b) Time averaged contour

Figure 4.12: Increased Loading case, annular rotor: Axial velocity downstream of the rotor

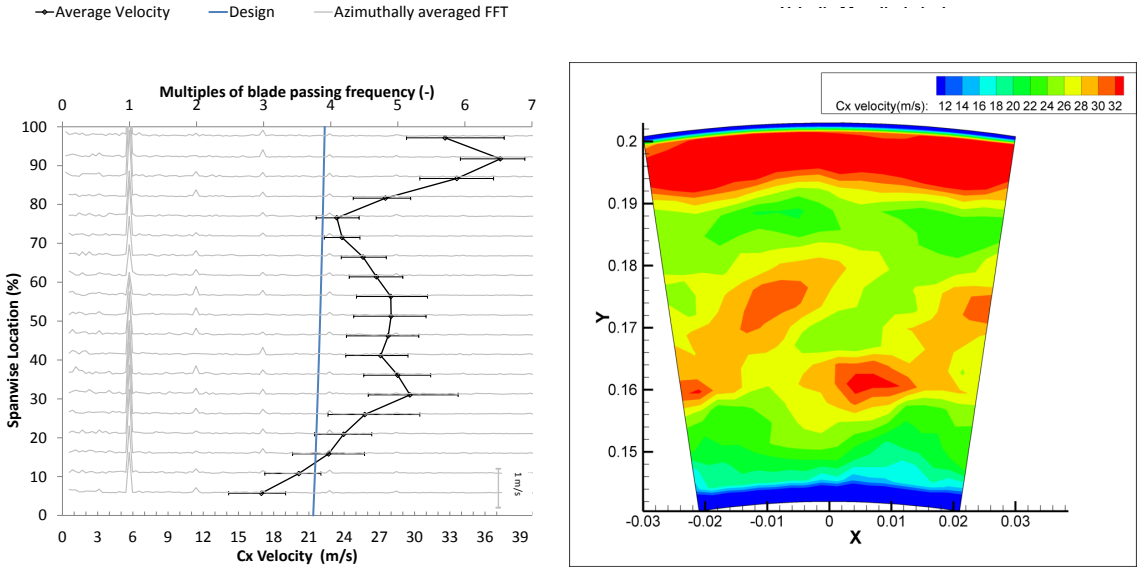

(a) Area averaged profile, with FFT (b) Time averaged contour

Figure 4.13: Increased Loading case, contoured rotor: Axial velocity downstream of the rotor

as for the increased loading condition, a less prominent endwall secondary flow structure was expected.

As seen with the design and increased loading conditions, the contoured rotor presented with an improvement in the flow structure. This can be seen in Figure 4.16 to 4.21. The peak in the tangential velocities at 26 % span was initially thought to be an anomaly due to the change in the yaw angle. Three separate tests at different yaw angles were

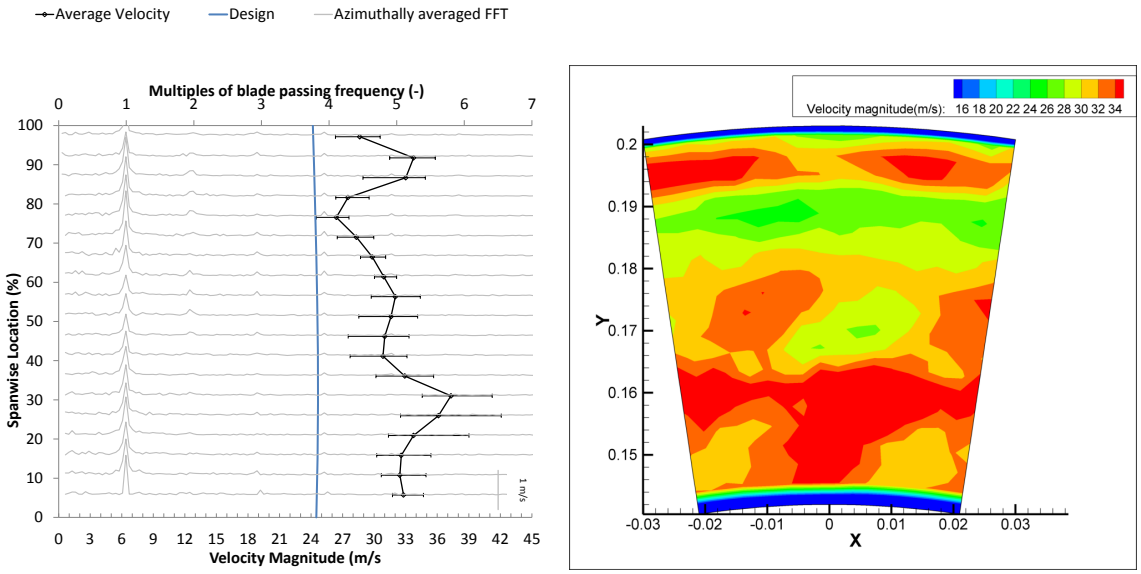

(a) Area averaged profile, with FFT (b) Time averaged contour

Figure 4.14: Increased Loading case, annular rotor: Velocity magnitude downstream of the rotor

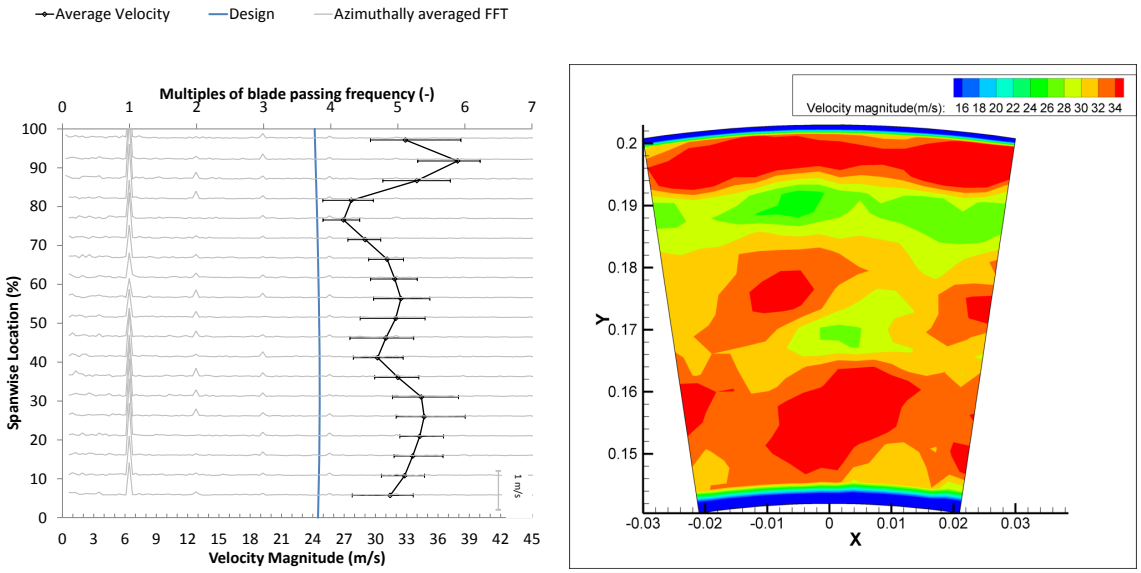

(a) Area averaged profile, with FFT (b) Time averaged contour

Figure 4.15: Increased Loading case, contoured rotor: Velocity magnitude downstream of the rotor

performed and the results were consistent and the same feature was evident in the annular and contoured data sets, therefore it was considered to be a flow feature.

Looking at Figure 4.18 and 4.19 it can be seen that the peak was due to the presence of the vortex core at approximately 30 % span. The vortex reduced the velocity above the core and increased it below the core (due to the circular nature of a vortex). The reduction

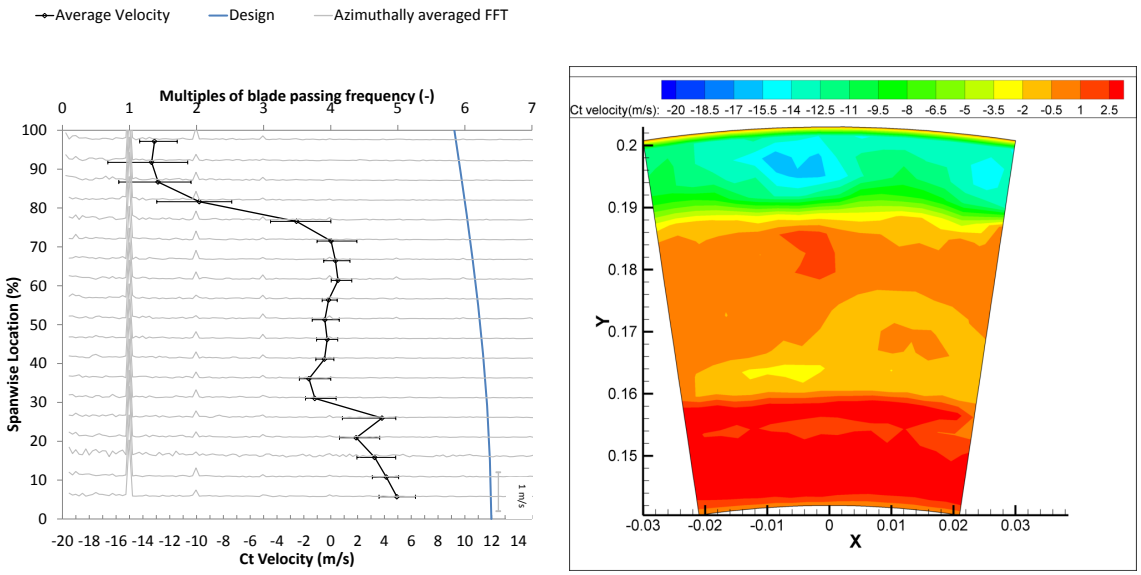

(a) Area averaged profile, with FFT (b) Time averaged contour

Figure 4.16: Decreased Loading case, annular rotor: Tangential velocity downstream of the rotor

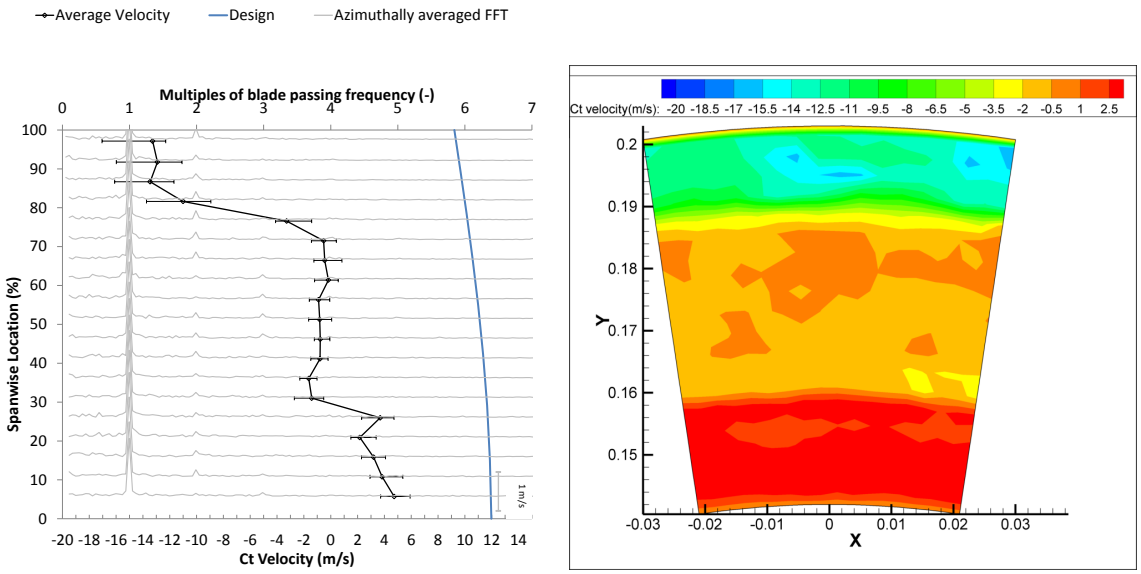

(a) Area averaged profile, with FFT (b) Time averaged contour

Figure 4.17: Decreased Loading case, contoured rotor: Tangential velocity downstream of the rotor

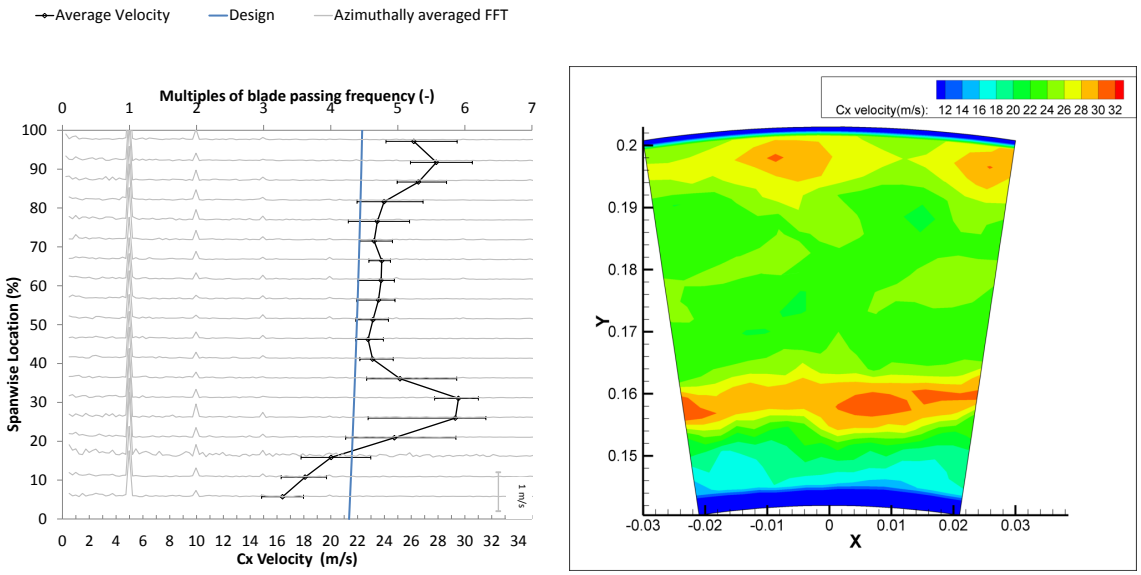

(a) Area averaged profile, with FFT (b) Time averaged contour

Figure 4.18: Decreased Loading case, annular rotor: Axial velocity downstream of the rotor

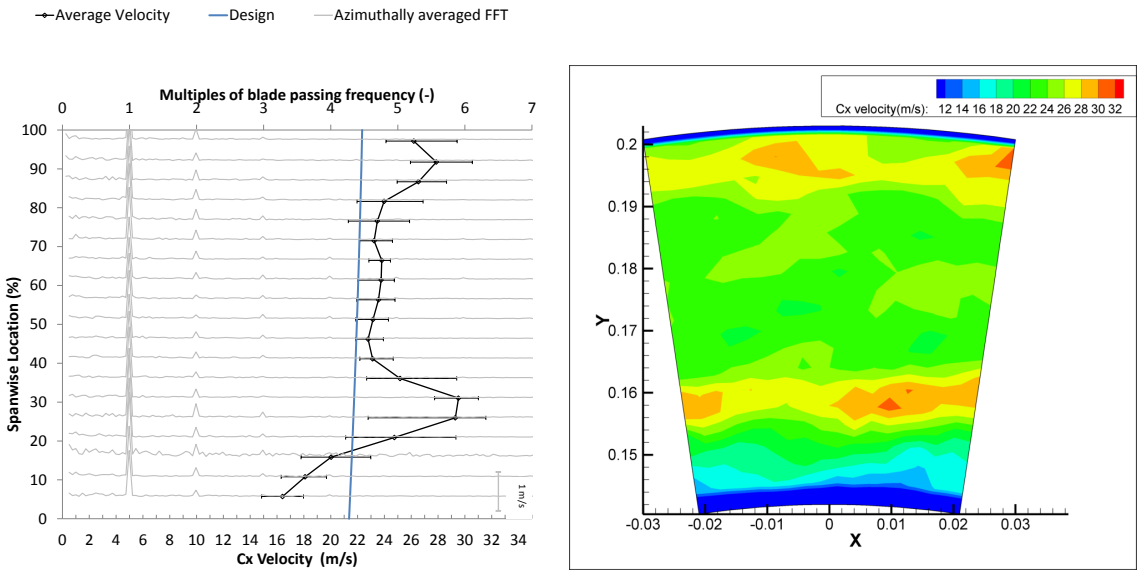

(a) Area averaged profile, with FFT (b) Time averaged contour

Figure 4.19: Decreased Loading case, contoured rotor: Axial velocity downstream of the rotor

in the tangential velocity at 20 % span was thought to be due to the boundary layer. Thus the peak would be the convergence of the endwall secondary flow vortex and the boundary layer flow, as shown in Figure 4.20 and 4.21.

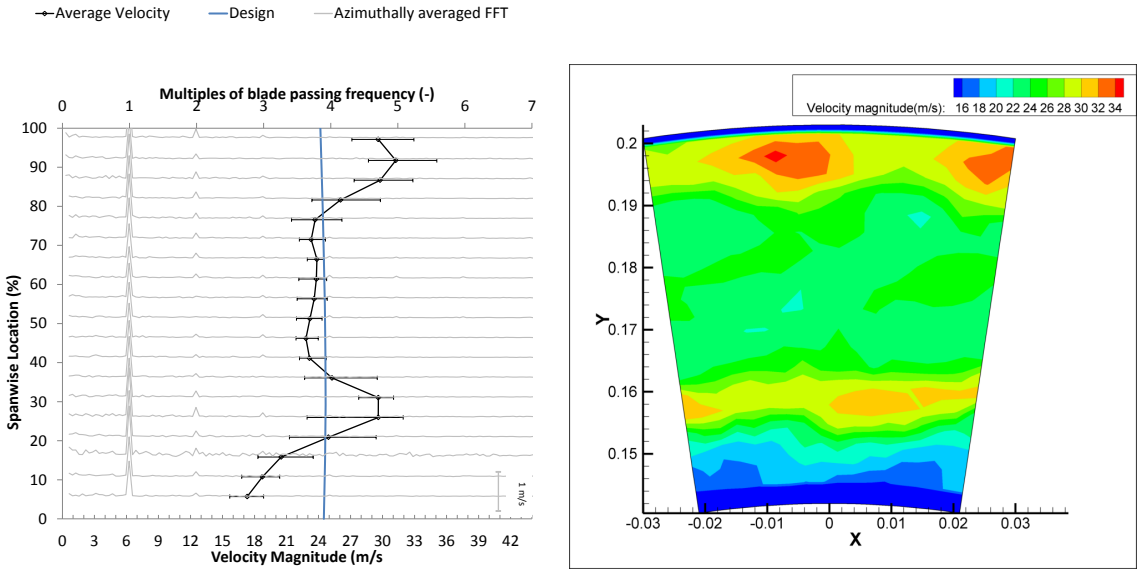

(a) Area averaged profile, with FFT (b) Time averaged contour

Figure 4.20: Decreased Loading case, annular rotor: Velocity magnitude downstream of the rotor

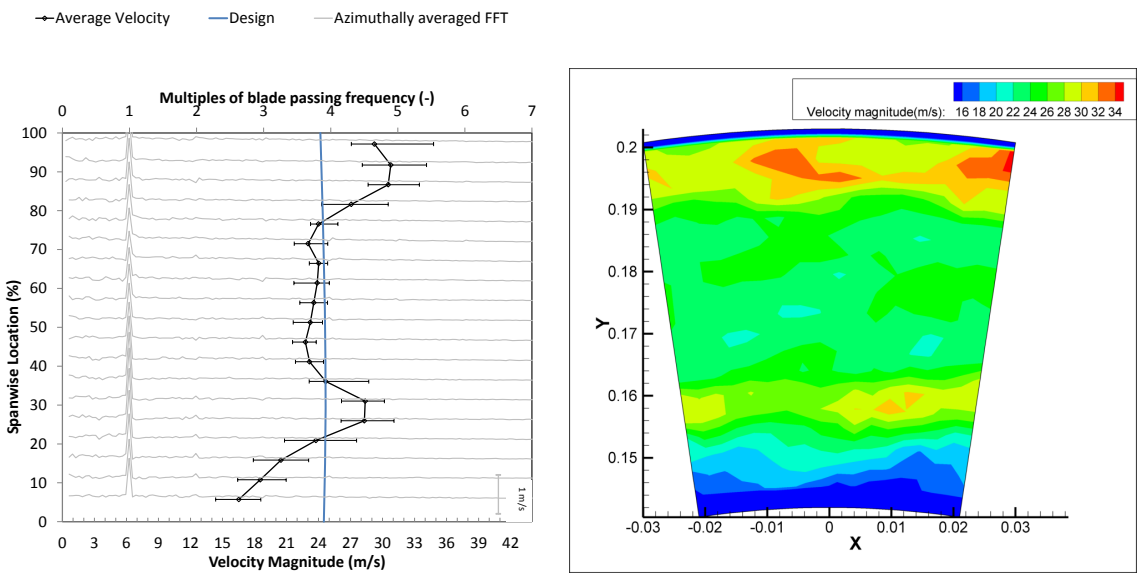

(a) Area averaged profile, with FFT (b) Time averaged contour

Figure 4.21: Decreased Loading case, contoured rotor: Velocity magnitude downstream of the rotor

4.3 Velocity Triangles

Velocity triangles are used during the design process of a turbine to determine basic performance characteristics as well as to match the exit flow angle of a blade row with the incidence angle of the downstream blade row (Saravanamuttoo *et al.*, 2001). For this reason it was felt that it would be beneficial to compare the velocity triangles of the design case to those measured experimentally. The velocity triangles presented were generated using the time averaged, azimuthally averaged results presented in Section 4.2.1 above (with only the design results being presented). Only six spanwise locations are presented, two at the tip, one midspan and three close to the endwall. The locations were chosen to highlight the changes in regions of interest. It was assumed that the flow entering the rotor was close enough to design to

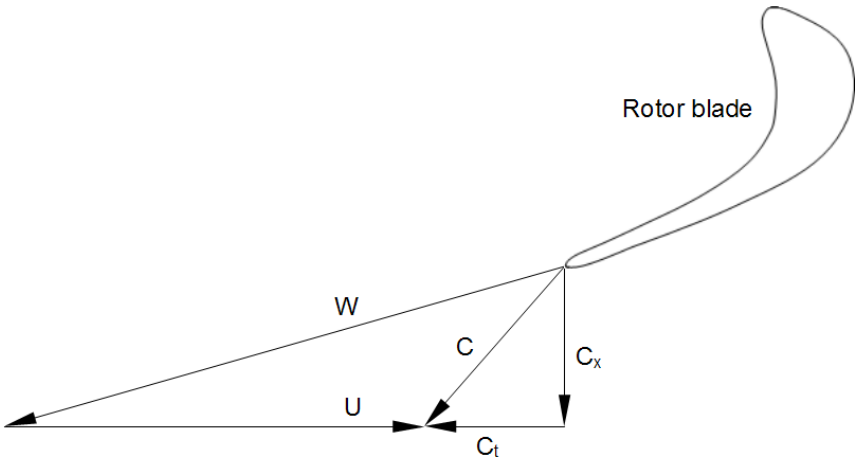

Figure 4.22: Convention used for the rotor exit velocity triangles, based on Dixon (1992)

The convention used for the velocity triangles can be seen in Figure 4.22. U is the blade velocity at the current radius, C_t is the tangential velocity (negative in 4.22, C_x the axial velocity (always the vertical line in 4.23), C is the absolute velocity magnitude and W the relative velocity magnitude.

In Section 4.2 it can be seen that the tangential velocity of the design speed was negative above 80 % span. For this reason Figure 4.23 (a) and (b) have the axial velocity to the left of the absolute velocity unlike in 4.22. It is evident that the annular case produces a relative velocity that is closer to that of the design case. The implication of this is that the downstream blade has an incidence angle that is closer to that which it was designed for. This is consistent with the observation that the contoured rotor has a negative influence on the flow at the tip.

At midspan, shown in Figure 4.23 (c), the tangential velocities were very similar ($0.7m/s$ difference), however, the contoured rotor axial velocity was higher. The resulting flow of the contoured rotor was thus further away from design than the annular flow. Both annular and contoured velocity triangles, however, were closer to the design than at the blade tip (in Figure 4.23 (a) and (b)).

The last 3 velocity triangles, Figure 4.23 (d) through (f) are from the hub region which has previously been shown to be the area of improvement in the flow. Figure 4.23 (d) shows that the relative velocity of the contoured rotor now matches that of the design case in

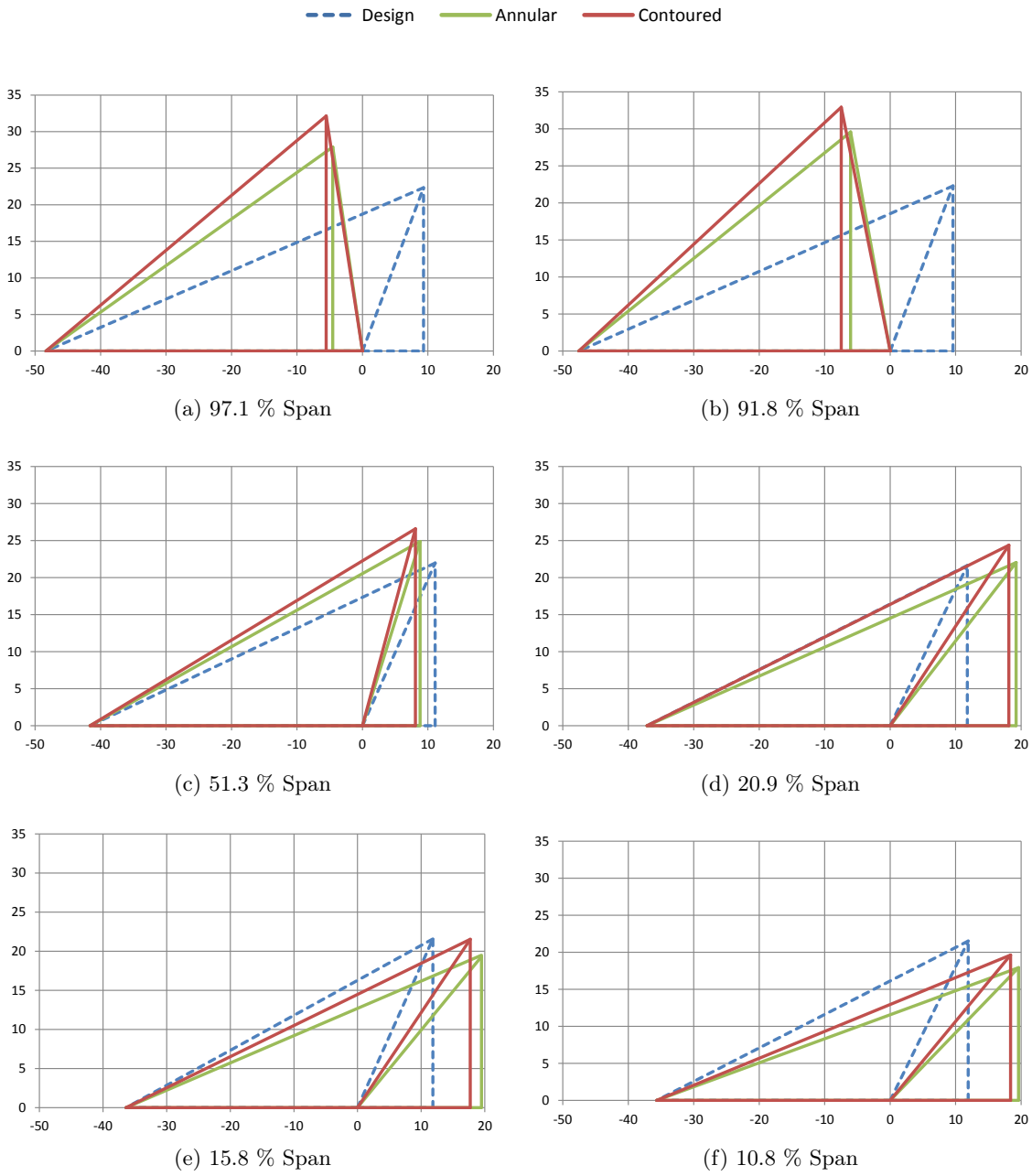

(a) 97.1 % Span

(b) 91.8 % Span

(c) 51.3 % Span

(d) 20.9 % Span

(e) 15.8 % Span

(f) 10.8 % Span

Figure 4.23: Comparison of the design condition rotor exit velocity triangles

orientation. However, due to the difference in tangential velocity compared to design, the downstream stator does not experience the designed incidence angle. Overall the contoured rotor velocity triangle is a closer match to that of the design velocity triangle.

Closer to the hub, in Figure 4.23 (e), the contoured rotor relative flow was no longer in line with the design as in Figure 4.23 (d). The velocity triangle of the contoured rotor was again closer to matching that of the design velocity triangle, with a reduced tangential velocity and an increased axial velocity.

Just off the hub at 10.8 % span, Figure 4.23 (f), the annular rotor exit velocity has a

large tangential component compared to the design case. The axial velocity was also found to be lower. The contoured rotor however, has a reduced tangential flow compared to the annular case, and an increased axial velocity. These changes result in a rotor exit relative velocity that was closer to that of the design case.

The effect the contour has on the flow at the hub becomes more evident when looking at the velocity triangles. The graphs in Section 4.2 show that the contour improves the flow, however, only of one component at a time. The velocity triangles show a comparison of the measured velocity components on a single graph. It can be seen that the contoured rotor moves the velocity triangle in the hub region to be closer to that of the design. The tangential velocity is reduced, reducing its influence on the secondary flow, which augments the axial velocity. In the tip region the opposite was true.

4.4 Discussion and Conclusions

It has been shown that the contoured rotor changed the flow field in several ways. The velocity magnitude in the endwall secondary flow region was reduced resulting in a reduction in the over-turning of the flow at the hub (below 30 % span). Thus the flow incidence was closer to design resulting in cleaner flow for the downstream blade rows.

The velocity magnitude of the tip leakage flow was increased in the contoured rotor. The mechanisms are not fully understood yet and further investigation is required (covered in Chapter 6). The influence on the tip leakage flow was also reported by Snedden *et al.* (2010*a*) and Hilfer *et al.* (2012) using a different measurement technique and can thus be considered to be a real flow effect in the test turbine.

The temporal variation in the velocities measured were reduced which produces a more temporally uniform inlet flow for the downstream blade rows. The variations would be seen by the downstream blade row as being a change in incidence angle with time, oscillating about the time averaged incidence angle. The varying incidence angle changes the lift produced by the individual blades (Japikse, 1986), which results in a fluctuating blade load. The lift fluctuations generate moving pressure patterns which would have an effect on noise generation (Japikse, 1986). Since the losses and heat load on the turbine airfoil surfaces are increased by the unsteady interactions from upstream blade rows (Sharma *et al.*, 1988), these will be reduced by the smaller fluctuations experienced.

The velocity of the endwall secondary flow vortex system was reduced in magnitude and more radially distributed, producing a more radially uniform velocity profile. That in turn means that downstream blade rows have an incidence angle which is closer to what it was designed for.

The same was true for the increased loading case, however, the peak tangential velocity was reduced by $2.7m/s$ as opposed to approximately $1m/s$ for the design case. With the redistribution of the endwall secondary flow, a more distinct wake was measured.

The velocity triangles show that the flow not only gets redistributed in the spanwise direction, but also from tangential to axial velocity components as well. With the tangential velocity reduced and the axial velocity strengthened, the rotor exit flow becomes more aligned with the design flow direction improving the downstream incidence angles.

Chapter 5

Numerical Technique

Before the numerical work could be performed, it was necessary to investigate which turbulence model was most appropriate for the geometry and boundary conditions. The main criteria used for selecting the turbulence model to be used in this investigation was velocity because it was one of the experimentally measured quantities. The velocity profile at a given point will be compared to the experimental results. The area traverses will also be used for comparison but the data will be radially averaged in order to produce a velocity profile.

5.1 Numerical Method

NUMECA's FINE^{TM}/Turbo v8 was used for the numerical work as it is a specialist CFD code aimed at turbomachinery. FINE^{TM}/Turbo uses EURANUS as the solver which uses Runga-Kutta central and upwind differencing (Numeca, 2007). FINE^{TM}/Turbo has several mechanism to accelerate the solution times, most notably is multigridding and the Non-linear Harmonic (NLH) method. Multigridding allows for a coarse mesh to be used to speed up transmission of the transported properties through the domain, which is then used on a finer mesh to improve definition. The Non-linear Harmonic (NLH) method is specifically for unsteady simulations and solves the harmonics of the flow as a transported quantity. During post processing these harmonics get converted to the fluctuating component of the flow and applied to the steady state solution.

Initially the Non-linear Harmonic (NLH) method employed by FINE^{TM}/Turbo was to be used to carry out the unsteady simulations. It was found, however, that the NLH method was not suitable for the current investigation due to the flow regime. Some of the flow features invalidated the assumptions made in developing the NLH method causing instability in the results (predicting a severe separation on the suction surface of the blade), thus the Domain Scaling method was used.

The Domain Scaling method is a moving mesh method which means that the mesh that contains the rotor is rotated about its axis in small increments. The flow domain is then solved for each of the increments, Numeca International (2008). The Domain Scaling method, however, requires that the periodicity of the stator and the rotor coincide. The matching periodicity requirement means that the outlet of the stator row has the same physical area as that of the inlet to the rotor row at the stator/rotor interface. Thus, for the relevant number of blades the numerical domain must consist of three stator blades

per stator row and two rotor blades.

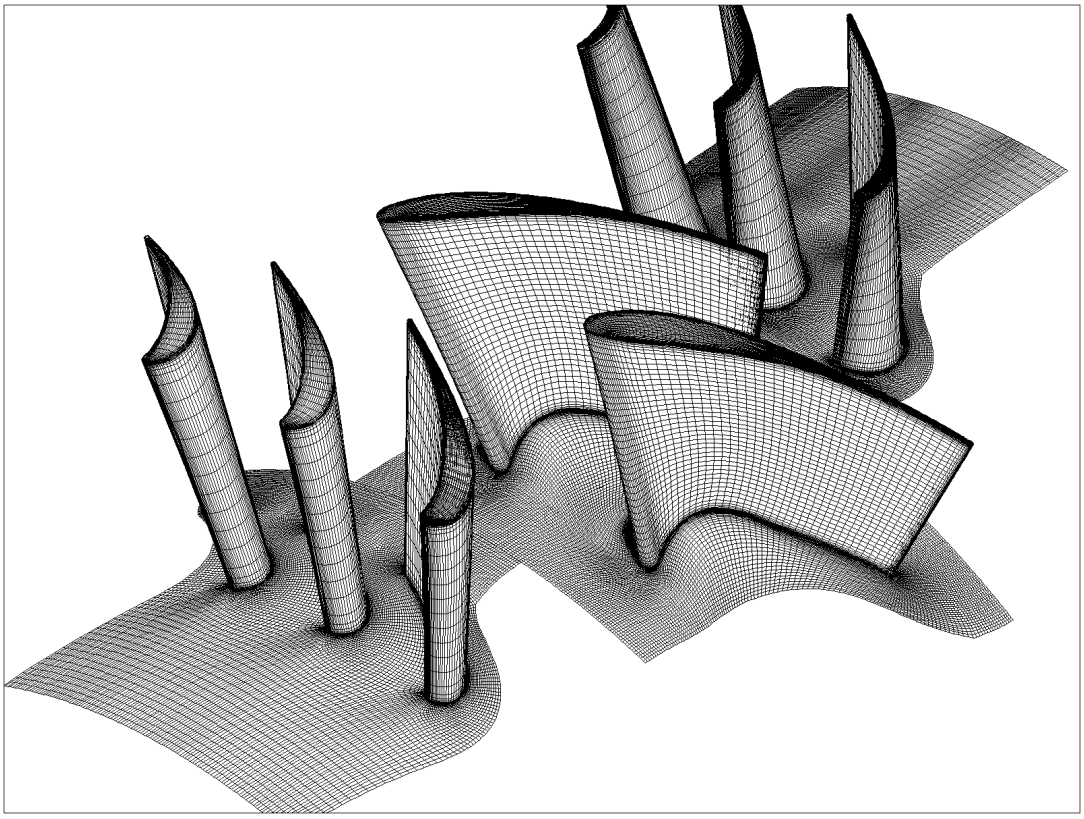

Figure 5.1: The blades used for the CFD analysis, showing the surface mesh

5.2 Geometry description

The geometry used for the simulation was the same used to manufacture the blade, as shown in Chapter 3. The profiles used to generate the turbine blades can be seen in Figure 3.4. The 1 $\frac{1}{2}$ stage blade surface mesh used for the CFD analysis can be seen in Figure 5.1. Since the current investigation is interested in the endwall effects, it was considered necessary to have as low a y^+ value as possible. The grid was thus generated with a $y^+ < 2.5$ (with the average below 1) for the entire endwall and blade surfaces. In order to capture the flow features adequately a fine mesh was used containing over 5 million cells. The author generated the current mesh for an investigation by Snedden (2011) who found that the soluton was grid independent (the grid was fine enough to capture the physics of the flow such that a finer mesh did not introduce any changes to the result. It met or exceeded the recommendations of Dunham and Meauze (1998), but the stator mesh was marginal.

5.3 Boundary Conditions

The types of boundary conditions that were chosen coincided with the values that were directly measured in the experimental setup. The inlet was specified by velocity components since the inlet velocity is specified by measuring the static pressure. The inlet static pressure may fluctuate depending on changes in density and temperature. The outlet was specified as having a radial pressure equilibrium at midspan ($R = 0.1725$). Turbine exit flows typically have a radial pressure distribution which would require a very large outlet section to ensure that the pressure profile gets mixed out sufficiently for a uniform outlet boundary type to be valid. FINE^{TM}/Turbo allows for a radial distribution at the domain outlet provided a reference pressure is provided at a known location. The working fluid was set as air with perfect gas attributes. The operating conditions tested at matched those of the experimental tests and can be seen in Table 3.3.

Inlet velocity $[m/s]$	21.38
Inlet temperature $[K]$	293
Number of rotor blades $[-]$	20
Number of stator blades $[-]$	30
Inlet turbulence $[\%]$	< 1
Outlet pressure $[kPa]$	82.9
Design rotational speed $[RPM]$	2300
Inlet temperature $[K]$	298.15
Characteristic length $[m]$	0.06
Characteristic velocity $[m/s]$	25
Characteristic density $[kg/m^3]$	1.0

Table 5.1: CFD Boundary conditions

The characteristic values listed in Table 5.1 are used to calculate certain values (Numeca, 2007). The characteristic length is used in the transition model to calculate the free stream turbulent intensity. The characteristic velocity is used for preconditioning of the simulation as well as to calculate the skin friction coefficient, C_f. The characteristic density is used for the Boussinesq approximation for incompressible flow to calculate the solid data C_f and to calculate the Reynolds number when the dynamic viscosity is calculated using Sutherland's Law.

5.4 Turbulence models

The turbulence models investigated were those available in FINE^{TM}/Turbo $V7.4$, thus no user coded or modified turbulence models were investigated. The choice of turbulence models investigated was based on the list of recommended low Reynolds number models found in the user manual (Numeca, 2007) for the flow conditions to be tested. The turbulence models investigated are as follows:

- Baldwin-Lomax

- Spalart-Allmaras
- Spalart-Allmaras with the Abu-Ghannam and Shaw (AGS) transition model
- The low Reynolds number Yang-Shih $k-\epsilon$ model
- The non-linear low Reynolds number $k-\epsilon$ model
- The Wilcox $k-\omega$
- The Shear-Stress Transport (SST) $k-\omega$

The Baldwin-Lomax is ideal for design cycle analysis where a robust and fast model is ideal. It is a two layer algebraic (zero equation) model. The turbulent viscosity is calculated differently in the inner and outer layers. Prantl's mixing length model is used in the inner layer, whereas the mean flow and the length scale are used for the outer layer (Numeca, 2007).

The Spalart-Allmaras turbulence model is a one equation model. It solves the transport equation for the eddy viscosity. Unlike the Baldwin-Lomax model, the Spalart-Allmaras model solves the transport equation for eddy viscosity, so it is always continuous. Due to the robustness and ability to treat complex flows the Spalart-Allmaras has become very popular. Compared to the $k-\epsilon$ turbulence model the Spalart-Allmaras is more robust and less computationally expensive (Numeca, 2007).

The Spalart-Allmaras with the Abu-Ghannam and Shaw transition model is the standard Spalart-Allmaras with a transition model incorporated in order to determine the transition of the boundary layer from laminar to turbulent. For this investigation only the Abu-Ghannam and Shaw model was investigated even though other transition techniques are available. The AGS model is based on the correlations obtained by Abu-Ghannam and Shaw (1980). The correlation is based on experimental data from transition on a flat plate with pressure gradients (Numeca, 2007).

The low Reynolds number Yang-Shih $k-\epsilon$ model is a form of the standard $k-\epsilon$ turbulence model that does not have a wall function. It infers the boundary layer profile from the input values at the wall (Numeca, 2007).

The non-linear low Reynolds number $k-\epsilon$ model does not use the first order closure model approximation according to the Boussinesq hypothesis. It is time consuming and is recommended for research only (Numeca, 2007).

The Wilcox $k-\omega$ (Wilcox, 1998) predicts free shear flow spreading rates that show good agreement with experiments for far wakes, mixing layers and planar, round and radial jets (Numeca, 2007).

The SST $k-\omega$ was developed to blend the robustness and accurate formulation of the $k-\omega$ and the free stream independence of the $k-\epsilon$. The $k-\omega$ and the $k-\epsilon$ are both multiplied by a blending function and added together (Menter, 1994). The blending function is created such that in the near wall regions the $k-\omega$ is used and in the free stream regions, far from the walls, the $k-\epsilon$ is used (Dunn, 2006; Numeca, 2007).

5.5 Method of comparison

In order to ensure that the turbulence model is appropriate, the CFD results were compared with experimental data. The experimental data used for the comparison was the 5-hole probe steady state measurements as at the time of the numerical investigation there were no unsteady results available. The CFD was run in steady state using the experimental conditions in order to make an appropriate comparison.

Comparison with pressure plots was not performed because the measurement technique only allowed an approximated static pressure. The 5-hole probe was connected using a modified connection method of Kaiser (1996). The calibration was performed using the method of Ingram (2003). The static pressure is calculated using the pitch ports only, since the yaw ports are only measured relative to each other. This allowing a more accurate yaw angle but less accurate static pressure.

5.6 Results and Discussion

As can be seen from the list of turbulence models there are some variants. For instance the Spalart-Allmaras model was run with transition modelling, and two versions of the $k-\epsilon$ model were tested.

In order to simplify the graphs the variants were compared with each other first. The model that fits the trend best was then compared with all the other turbulence models. By splitting up the comparison in this manner, the number of data series present on the graphs was reduced, which made the graphs less cluttered, and easier to interpret. Thus none of the variants were presented in Figure 5.4.

It was thought that due to the low Reynolds number the flow might be transitional in regions. Thus the inlet turbulence boundary conditions were altered to investigate possible effects of the inlet conditions. For the Spalart-Allmaras, three values of turbulence viscosities were used, namely $\mu_t = 0.0001$, $\mu_t = 0.0005$ and $\mu_t = 0.0009$. The default value in FINE^{TM}/Turbo is $\mu_t = 0.0001$ and is typical for external flows (Numeca, 2007). For turbo-machinery flows the recommended value of turbulence viscosity is between $\mu/\mu_t = 1$ and $\mu/\mu_t = 5$, thus the extreme values as well as a middle value is chosen (these values are based on the viscosity of air as being $\mu = 1.8e-5 Pa.s$).

5.6.1 Comparison of variants

Looking at Figure 5.2 and Figure 5.3 it was evident that there were negligible differences between the different variants even when changing the inlet turbulence level. Changing the turbulent viscosity level any more increased it beyond the recommended levels (Numeca,

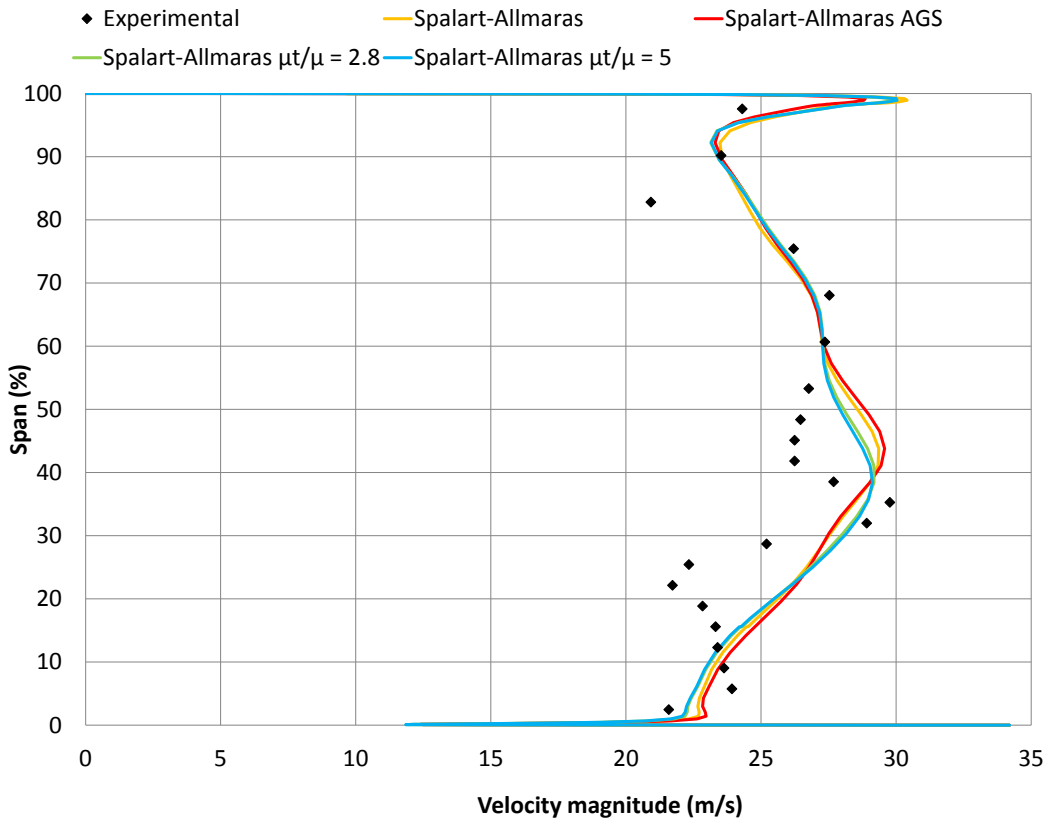

Figure 5.2: Comparison of the velocity profile at X3 using Spalart-Allmaras

2007), thus the turbulent viscosity ratios beyond this were not tested.

With respect to the Spalart-Allmaras variants in Figure 5.2, the experimental average velocity was $C = 24.92m/s$ compared to the numerical average velocity of $C = 24.79m/s$. The trend was correct, but it did not capture all features in the profile. Since all the variants of the Spalart-Allmaras produce approximately the same velocity profile, only the standard Spalart-Allmaras was compared with the other turbulence models due to its reduced computational expense.

It was evident from Figure 5.3 that the different $k - \epsilon$ variants did not differ significantly. The biggest differences were found at the hub and casing. Since the resolution in the experimental measurements at the hub and casing were not as fine as the numerical results, the differences in turbulence models in this region was not relevant.

As with the Spalart-Allmaras, the $k - \epsilon$ variants were very similar. To reduce complexity the Yang-Shih $k - \epsilon$ turbulence model was thus treated as the best since the added complexity of the variants adds to computational expense, but did not improve the results significantly..

The $k - \omega$ variants (which are shown in Figure 5.4) were significantly different and were

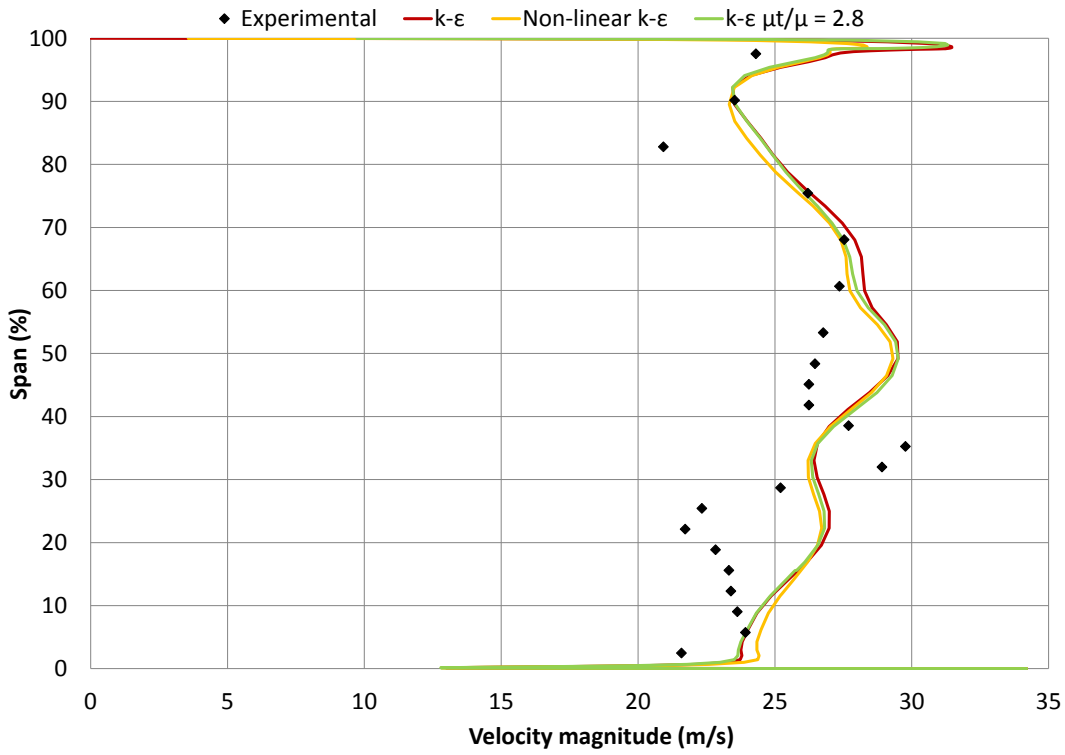

Figure 5.3: Comparison of the velocity profile at X3 using $k - \epsilon$

thus compared directly with the other turbulence models.

5.6.2 Comparison of turbulence models

Looking at Figure 5.4 it was evident that none of the turbulence models show an ideal correlation. The turbulence models either have a good area averaged velocity, or a good reproduction of the velocity profile. A good reproduction of the velocity profile is sought since the current investigation is more interested with flow features and not mean values.

With reference to Figure 5.4 it is clear that all the turbulence models fail in some aspect or another. The Spalart-Allmaras, Baldwin-Lomax and the $k - \epsilon$ follow the values at an appropriate level, but do not capture the profile very well. The $k - \omega$ and the SST $k - \omega$, however, follow the profile reasonably well but fail to capture the correct values.

In the current investigation the trend is of more importance than the actual values since the values can generally be captured experimentally. The trend is a result of the flow features. These features and the manner and location in which they are initiated are of importance. Thus the $k - \omega$ models are the most appropriate.

The Wilcox $k - \omega$ (Wilcox, 1998) captures the trend very well at the casing with the tip leakage flows peaking in the same locations. Conversely, at the hub it does not quite capture the position of the peaks. The trend shows the correct type of features but in the

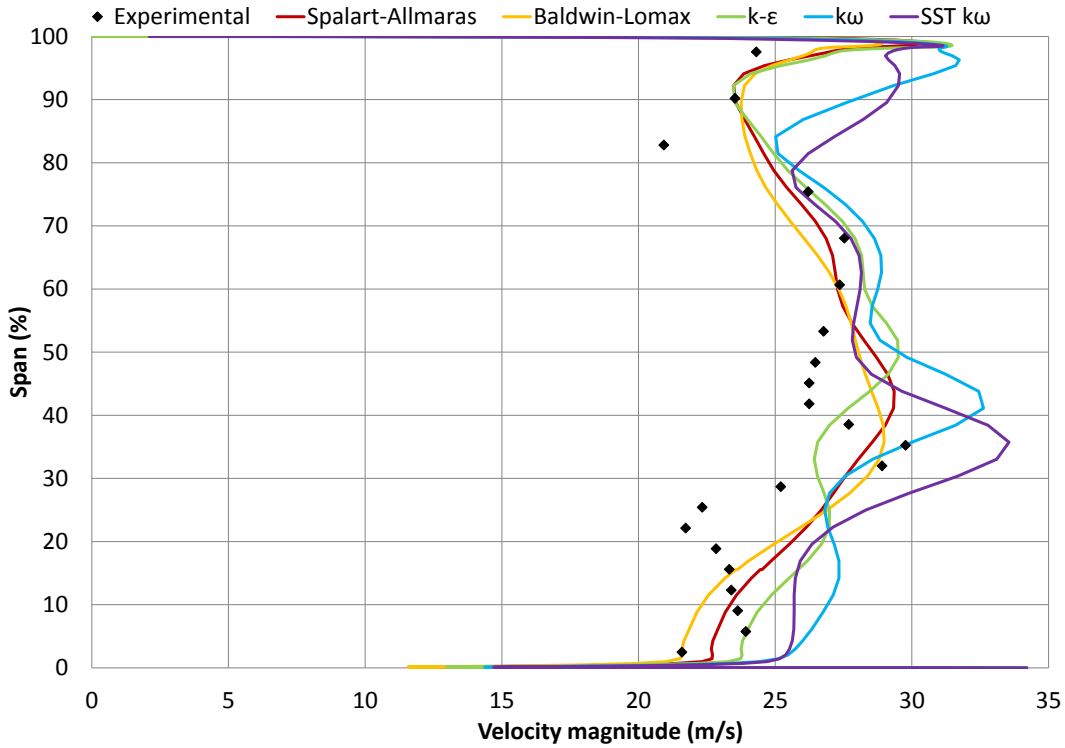

Figure 5.4: Comparison of turbulence models at X3

wrong locations. The SST $k-\omega$, however, captures the hub features very well but captures the flow features poorly at the casing. Therefore the SST $k-\omega$ was chosen, since the area of interest is the flow near the end wall.

5.7 Conclusions and Recommendations

Looking at the velocity profiles it was evident that none of the current turbulence models were sufficient to accurately model the secondary flows present in a rotating environment. Thus the most appropriate turbulence model was determined from a set of available turbulence models in a commercial CFD code, Numeca's FINE^{TM}/Turbo . It was found that the Spalart-Allmaras and the Baldwin-Lomax models are adequate for the cases where the average velocity and thus flow rates are of importance. The Spalart-Allmaras and the Baldwin-Lomax models also have a lower computational expense than the other models.

The $k-\epsilon$ models gave a fair approximation but did not improve the accuracy of the simulation when compared to the added computational expense. The SST $k-\omega$ model performed the best of the two $k-\omega$ models tested. It did not capture the velocity values very accurately but it captured the velocity magnitude profile the best of all the turbulence models tested.

With reference to the data it is evident that Baldwin-Lomax is still one of the best all

purpose models for turbomachinery. The SST $k-\omega$ shows some promise as it predicted the velocity magnitude reasonably well, but the Baldwin-Lomax predicted the radial and tangential velocities better.

Due to the complex nature of secondary flow, it may still be sometime before computational hardware and the numerical models are such that the complexities can be appropriately modelled. Until such time it is important that new models be investigated and validated against experimental data. It is also recommended that the computational expense be carefully weighed against the required accuracy. FINE^{TM}/Turbo does offer higher order turbulence models but they are non-linear and not recommended for use in design cycle analysis (Numeca International, 2008) due to the added computational expense (these models were tested in the current investigation however did not prove to increase accuracy).

Chapter 6

Numerical Results

The numerical results will be presented in this chapter. During the preparation of Dunn *et al.* (2010) it became evident that hard copy versions of the unsteady data did not produce the required insight into the data presented. For this reason a digital appendix (Appendix A) is provided which contains the animations describing the unsteady flow fields. The contours presented in the thesis are the time averaged contours, unless otherwise stated.

6.1 Time averaged results: Comparison of numerical and experimental results

The time averaged results presented below are the time averaged results as calculated by FINE^{TM}/Turbo as part of the solution process. The last step of each simulation is to output a series of files as specified by the user, the two of interest in this section were the time averaged and the meridionally (azimuthally), time averaged results. The averaging technique applied to the CFD data was done in the same manner as was used for the experimental data averaging.

6.1.1 Design Condition

In Figure 6.1 it can be seen that in general the trend of the experimental results was well captured by the CFD. As seen in the comparison of the steady to unsteady experimental results in Chapter 4 regions of high shear were not well captured. Specifically the tip leakage flow and the endwall secondary flow region.

The rotor outlet relative yaw angle in Figure 6.1a showed that the majority of the differences between the annular and contoured numerical results occurred at or below midspan. The changes seen all made the outlet relative yaw angle more uniform, with the under-turning at midspan being reduced (increased outlet relative yaw angle) and the over-turning in the endwall secondary flow vortex being reduced (decrease in outlet relative yaw angle). The steady state numerical results of Snedden (2011) showed that there was a difference in the tip leakage flow, which was not captured by the unsteady investigation.

The rotor relative velocity magnitude showed a similar trend with the tip leakage flow of both annular and contoured rotor being the same. However, this was only true above 95 % span. The peak values of rotor relative outlet velocity were comparable, however, the spanwise location was not. The contoured rotor had peaks that were located closer to the hub than those of the annular rotor.

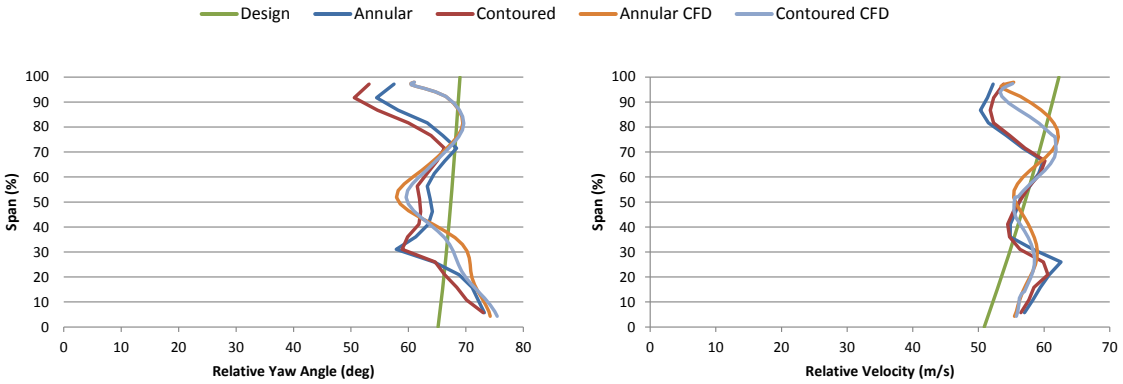

(a) Relative outlet flow angle

(b) Relative velocity magnitude

Figure 6.1: Design case: Comparison of unsteady annular and contoured CFD and experimental results

A point of concern was that the steady state CFD as well as the experimental work (both steady and unsteady) found that the contoured rotor affected the tip leakage flow. Looking at the contours in Figure 6.2 and 6.3 it can be seen that the tip leakage flows of the annular and contoured rotors were comparable.

Figure 6.4 shows the comparison of the steady and unsteady CFD results. The difference in the tip leakage flow of the steady state results were larger than the difference found in the unsteady results. With the exception of the relative rotor outlet flow angle (6.4a), the overall trend match well between the steady and unsteady results. The steady state CFD predicted a more pronounced annular endwall secondary flow region.

Since the steady state CFD was performed using the same mesh, numerical settings and solution controls (except for the handling of time) it was concluded that the difference was due to the wake shedding through the tip leakage flow as well as at the trailing edge of the blade. The experimental setup was scrutinized at this stage to answer the experimental differences.

Early in the testing phase it was found that the blades rubbed against the casing in 3 distinct locations. The blades were carefully sanded until they did not rub against the casing. This was tested using engineering blue painted on the blade tips and running the rig at maximum speed (to allow the blades to stretch under centrifugal forces). Once the blades did not transfer any of the engineering blue onto the casing they were deemed to not rub and testing commenced.

The scuffed region was measured and found to be larger in the axial direction than the axial chord of the turbine blades in question. Thus the blades were untwisting under the aerodynamic load applied. When the blades untwist the tip flow becomes more axially aligned than intended (under turned), which results in a lower rotor exit yaw angle as seen in Figure 6.2. Unfortunately during the scuff testing the rig was run at maximum speed (3000 RPM) to maximise the centrifugal load and thus maximise the amount of rubbing (i.e. if rubbing does not occur at this speed it will not at test speeds). The result was that the extent of the untwist at the speeds tested at could not be determined, nor the difference in the untwist of the annular and contoured rotor blades as the casing scuff marks were for a speed not used during testing.

With respect to the endwall secondary flow, Figure 6.2 shows that the size and mag-

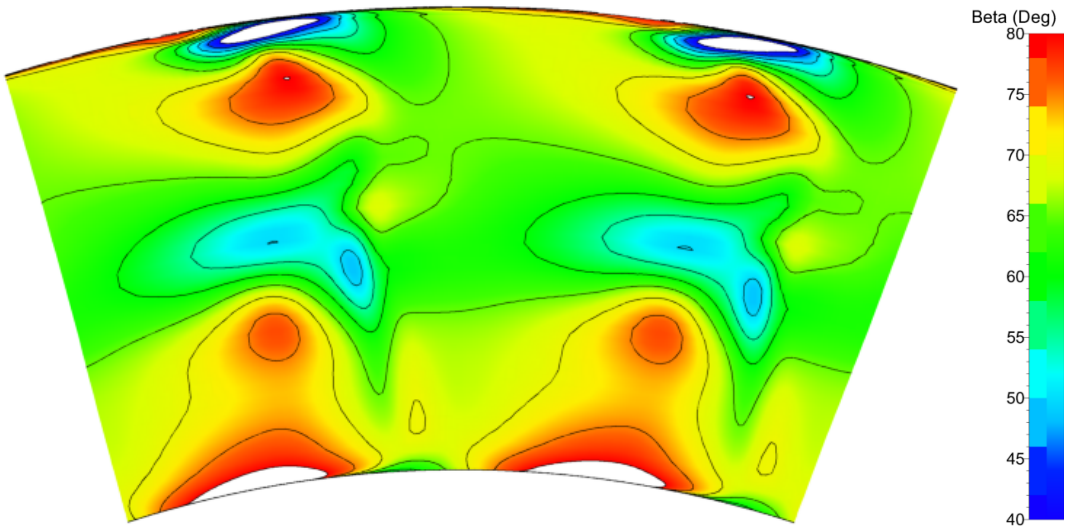

(a) Annular endwall

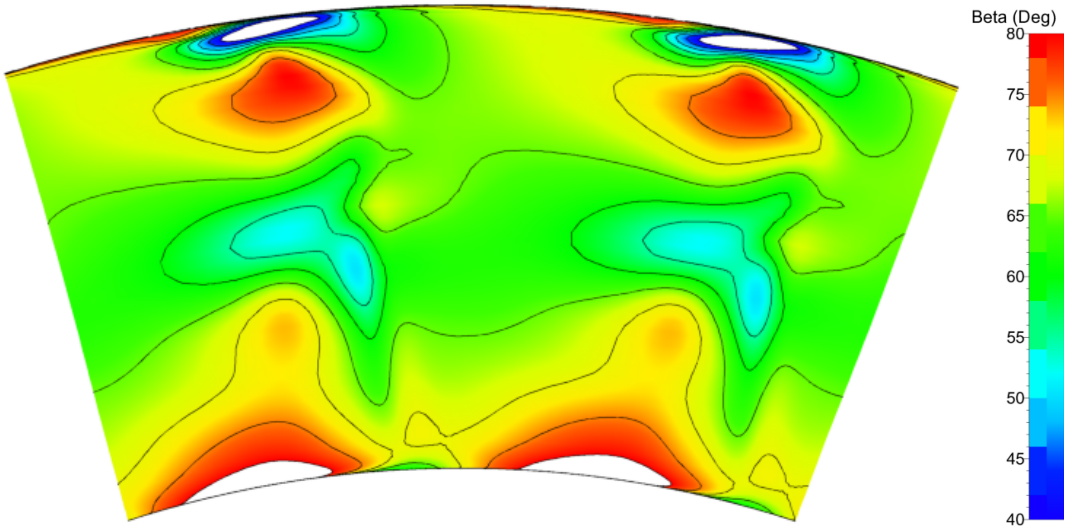

(b) Contoured endwall

Figure 6.2: Design case: Comparison of annular and contoured outlet flow angle contours

nitude of the endwall secondary flow vortex structure of the contoured rotor have been reduced in both size and magnitude. In general the contour has become more uniform. A more uniform rotor exit flow means a more uniform stator inlet flow which results in a more uniform incidence angle.

In Figure 6.3 it can be seen that the contoured rotor does present with a radial leg extending from the endwall secondary flow vortex down towards the hub (to the left of the blade wake). Figure 6.5 shows streamlines and streamtubes (for clarity) coloured according to point of release. The point of release was kept constant across the loading conditions so as to make a comparison with the design case. The yellow and orange streamlines were released from the tip. The purple streamtubes were released from the leading edge of the blade. The red and blue streamtubes were released from the rotor endwall boundary layer.

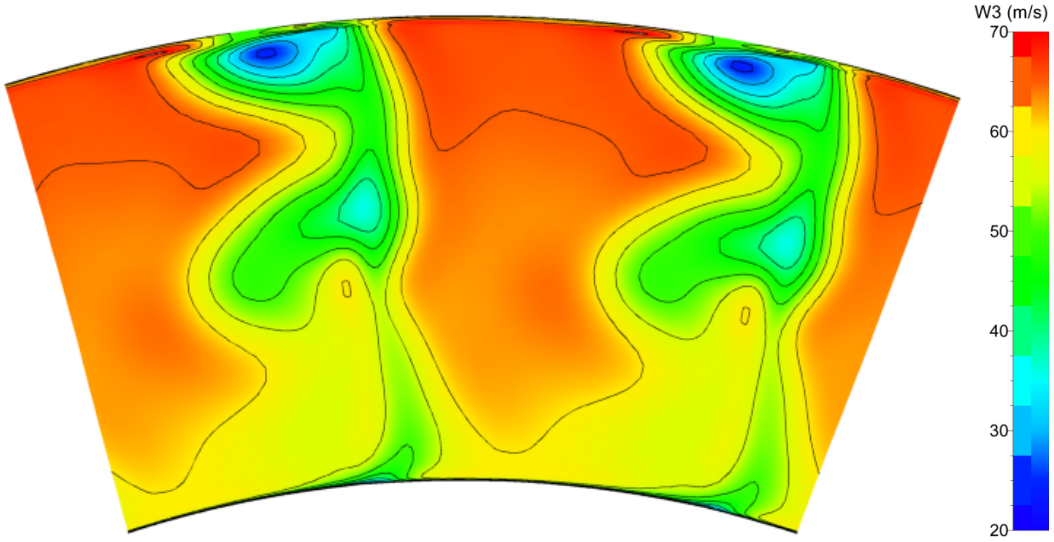

(a) Annular endwall

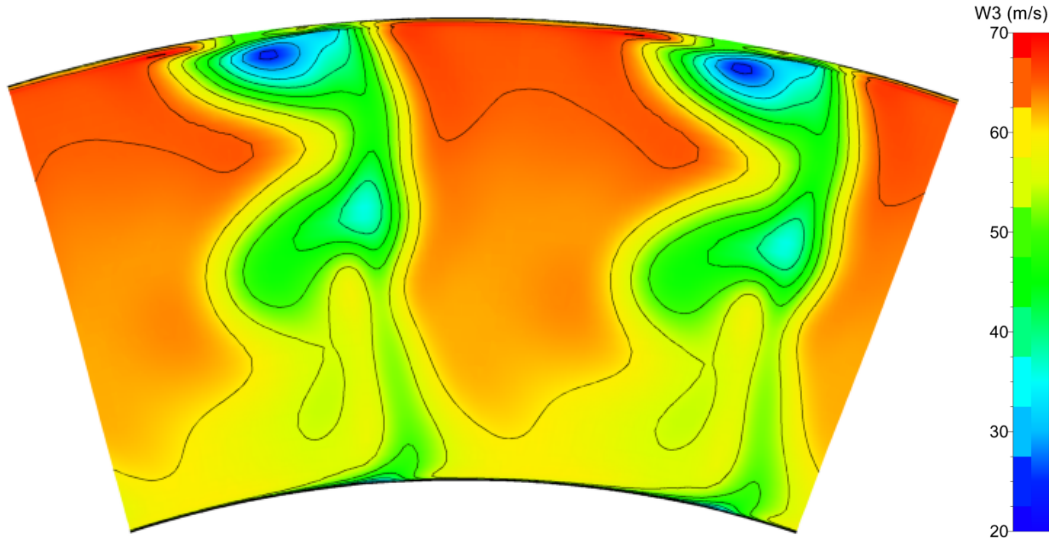

(b) Contoured endwall

Figure 6.3: Design case: Comparison of annular and contoured relative velocity magnitude

Where the red stream tube represents the pressure surface leg of the horseshoe vortex and the blue represents the suction surface leg of the horseshoe vortex. The black streamlines represent the cross passage flow, driven by the cross passage pressure gradient.

Figure 6.5 also has the relative rotor exit flow angle plotted on the measurement plane. From this it can be seen that the region of overturning evident at approximately 30 % span is caused by the bottom of the endwall secondary flow vortex system. Similarly, the under turning of the flow is caused by the top of the endwall secondary flow vortex core. The cause of the protrusion below the endwall secondary flow vortex in Figure 6.3 now becomes evident. The endwall secondary flow vortex system has become less tightly wrapped in the contoured rotor case.

The endwall contour has weakened the passage vortex that moves due to the cross

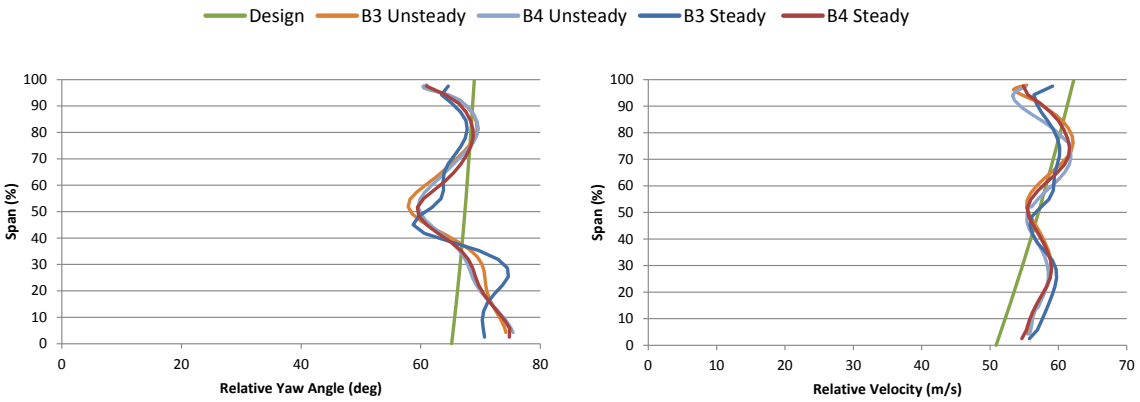

(a) Relative outlet flow angle (b) Relative velocity magnitude

Figure 6.4: Design case: Comparison of steady and unsteady CFD results

passage pressure gradient. The reduction in momentum of passage vortex results in less curling up of the horseshoe vortices. Allowing for less overturning at the hub and a more radially distributed endwall secondary flow vortex system.

The streamlines in Figure 6.5 again highlight that the tip leakage flow for the annular rotor matches that of the contoured rotor. The streamlines follow the same path and have inflections in the same places. When viewing the animated version in Appendix A (Slide 3 in the design case file) it can be seen that the oscillations of the annular and contoured case are comparable as well.

6.1.2 Increased Loading Condition

Looking at the relative outlet flow angle in Figure 6.6a it is evident that the numerical results correlate well with the experimental. Again however, the radial location of the endwall secondary flow vortex structure were over predicted. The numerical results predict the spanwise location of the endwall secondary flow as being 40 % as opposed to approximately 25 % span as measured experimentally.

As in the design case, the tip leakage flow was not well captured. The experimental results showed under turning occurring above 75 % span, with the contoured rotor under turning more than the annular case. The numerical results on the other hand show no difference between the annular and contoured relative outlet flow angle above 80 % span. Again this was due to the untwisting of the blade.

Below 80 % span the contoured relative outlet flow angle was improved, with the under turned flow between 40 % and 70 % span reduced (increased relative outlet flow angle). The over turning below 40 % was also reduced (decrease in relative outlet flow angle), with the over turning being increased below 15 % span. Resulting in an overall correction to the relative outlet flow angle.

The relative velocity, however, was not as drastically altered as the relative outlet flow angle with the majority of the changes occurring below 30 % span in the endwall secondary flow vortex region. A region between 70 % and 80 % span was improved (reduced), but the improvement was small (a mere 0.75 m/s).

The contours in Figure 6.7 show that the endwall secondary flow vortex system was larger than the design case (Figure 6.2) as a result of the increased turning of the flow in the

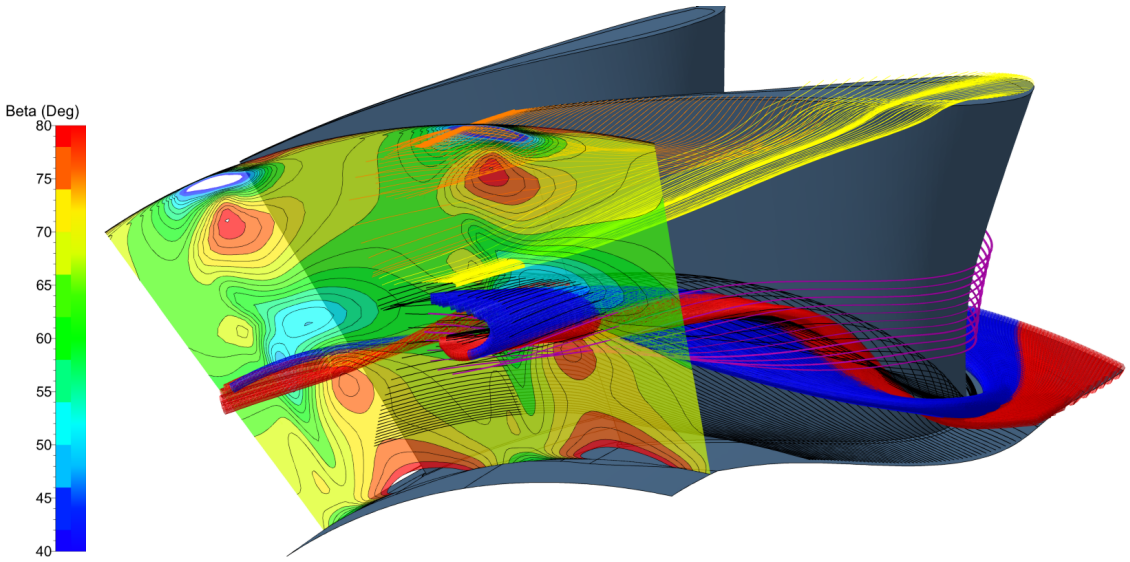

(a) Annular endwall

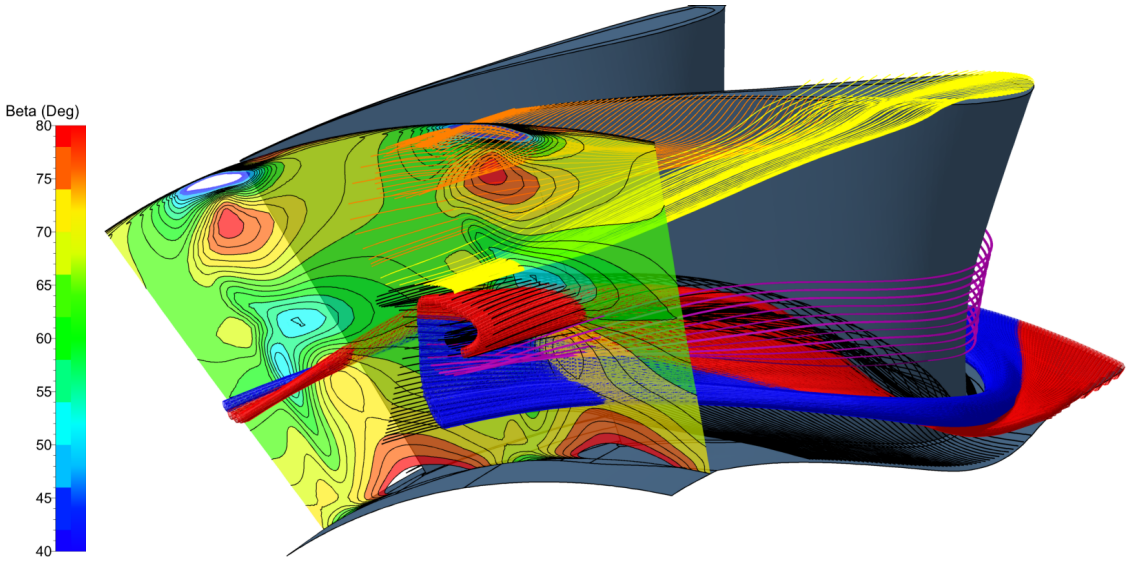

(b) Contoured endwall

Figure 6.5: Design case: Stream tubes showing rotor exit relative outlet flow angle at rotor exit

rotor passage. The contoured rotor shows a much weaker endwall secondary flow vortex system with both the over turning and the under turning being reduced. Improvement to the over turning being more drastic than the under turning with a change in size and magnitude.

Looking at the streamtubes in Figure 6.9 it can be seen that it was the over turning below the endwall secondary flow vortex that was affected the most. The reason for this is twofold: firstly the weakened passage vortex does not augment the wrapping up of the endwall secondary flow vortex; and secondly the portion of the tip leakage vortex that originates from the leading edge of the rotor blade (yellow streamlines in Figure 6.9) get

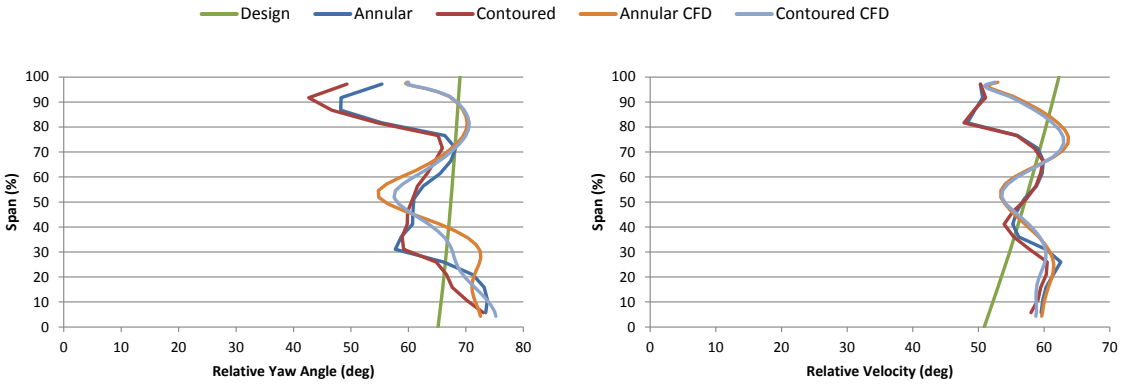

(a) Relative outlet flow angle

(b) Relative velocity magnitude

Figure 6.6: Increased loading case: Comparison of unsteady annular and contoured CFD and experimental results

entrained with the endwall secondary flow vortex causing the under turned region to be restrained from rising any further. The tip leakage flow is thus the cause of the flat shape of the endwall secondary flow vortex seen in Figure 6.7 and 6.9.

Comparing the unsteady numerical results to the steady state in Figure 6.10 it can be seen that they correlate well. The annular case showing the best correlation. The unsteady contoured case shows a larger improvement in the endwall secondary vortex region, predicting a larger reduction to the over turned flow than that of the contoured steady case.

The rotor exit relative velocity profiles shown in Figure 6.10b show good correlation between the steady numerical results and the unsteady numerical results. The most notable differences being a change to the spanwise location of the various flow features. Similar differences are evident when comparing the steady state difference between the annular and contoured results with the unsteady difference between the annular and contoured results.

6.1.3 Decreased Loading Condition

The decreased loading case represents those conditions were the rotor rotates faster than the design case such that the rotor turns the flow less. Due to the decreased turning the cross passage pressure gradient is weaker which results in a weaker endwall secondary flow vortex. The relative velocity of the boundary layer flow impinging on the blade is slower than that of the design case (since the blade is rotating faster than the flow expects it to) resulting in weaker horseshoe vortices. The final result is a more uniform rotor outlet flow as seen in Figure 6.11. Again the CFD does not capture the endwall secondary flow vortex, but it should be noted that the difference between the annular and contoured was well captured (even though there is negligible difference).

Figure 6.12 and 6.13 shows again that the differences are negligible. The streamlines and streamtubes in Figure 6.15 also show negligible differences. The endwall secondary flow vortex of the contoured rotor is slightly more unwrapped than the annular case, but the difference is slight.

The comparison of the steady and the unsteady rotor relative outlet flow angle numerical results in Figure 6.14a shows that three of the four results match with negligible

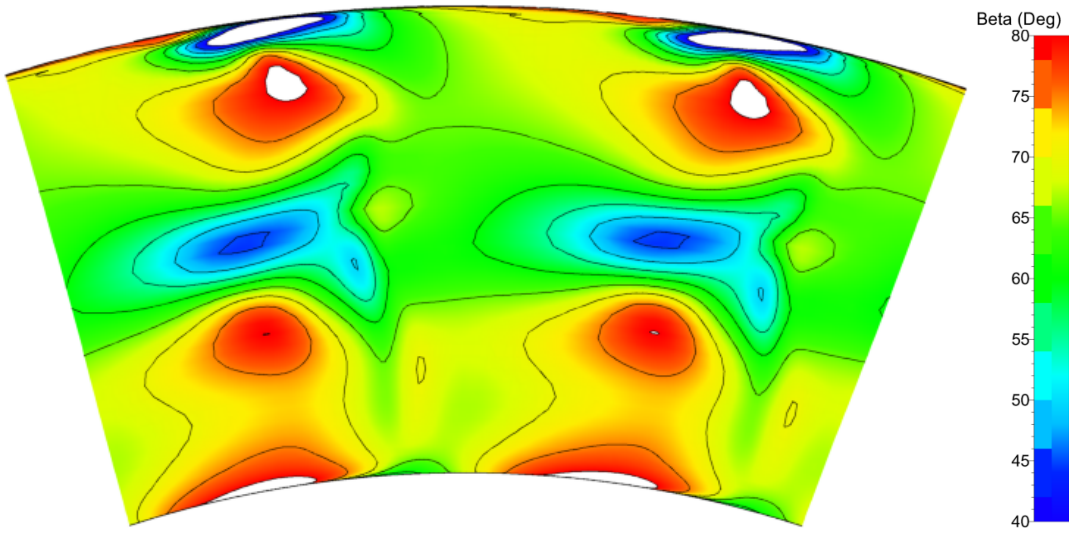

(a) Annular endwall

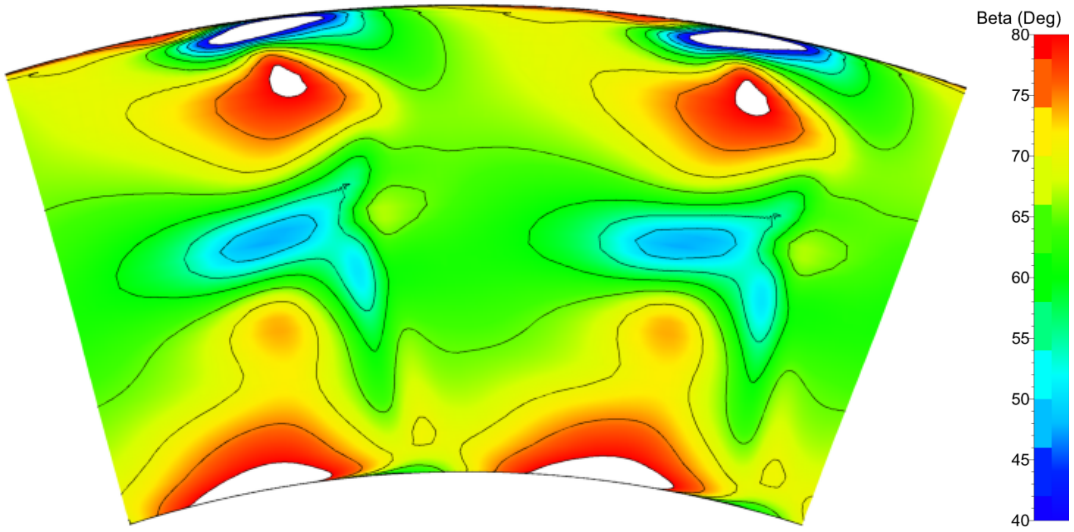

(b) Contoured endwall

Figure 6.7: Increased loading case: Comparison of annular and contoured outlet flow angle contours

differences. Snedden (2011) felt that the annular steady results were questionable, which is verified by the unsteady results.

The rotor exit relative velocity magnitude shown in Figure 6.14b does not reveal anything new that has not been covered previously.

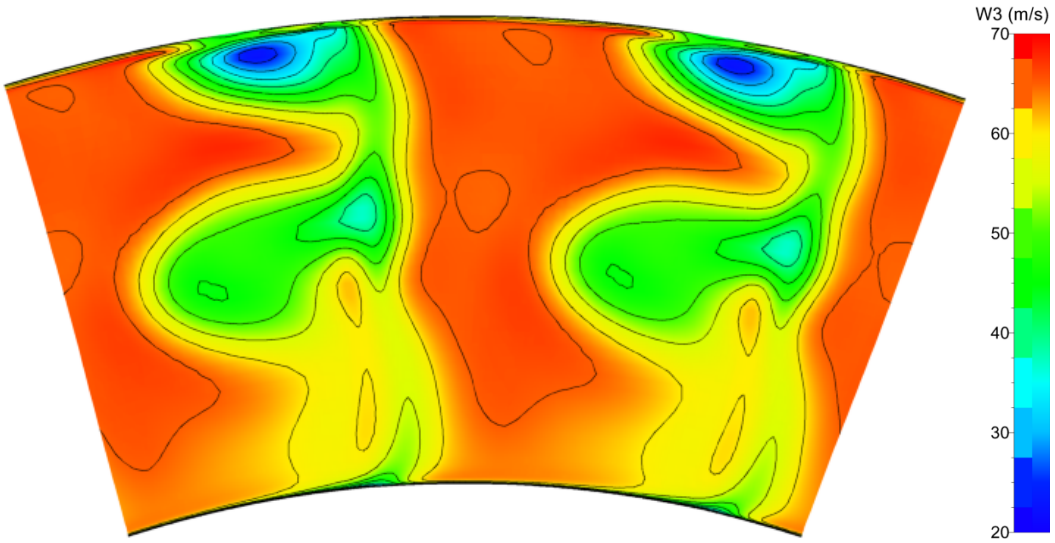

(a) Annular endwall

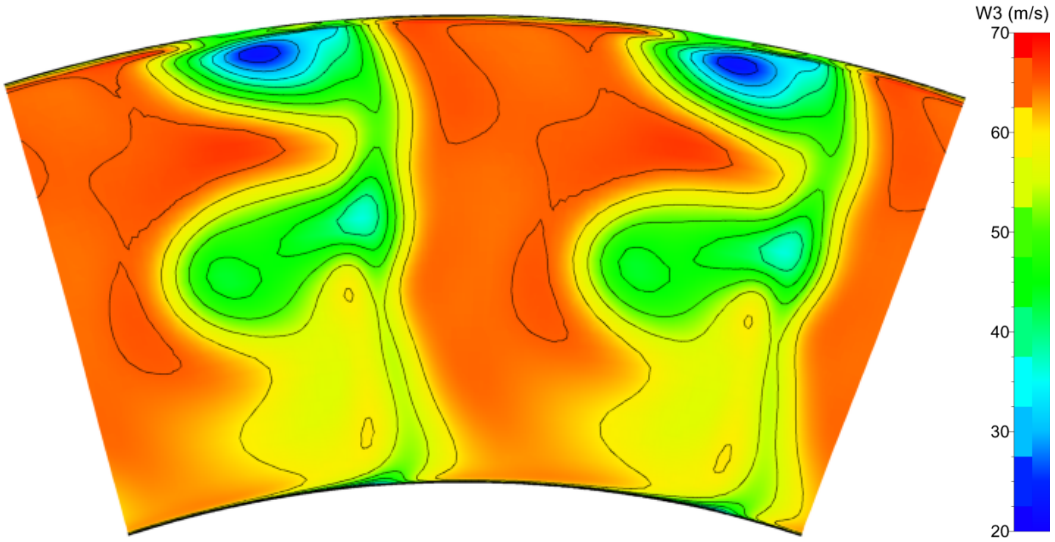

(b) Contoured endwall

Figure 6.8: Increased loading case: Comparison of annular and contoured relative velocity magnitude

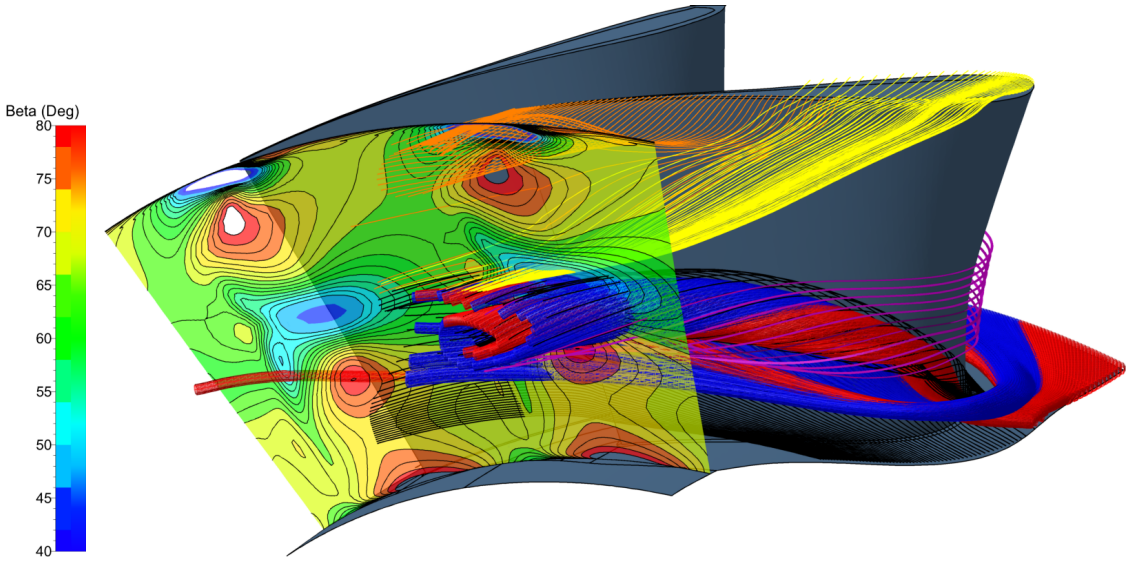

(a) Annular endwall

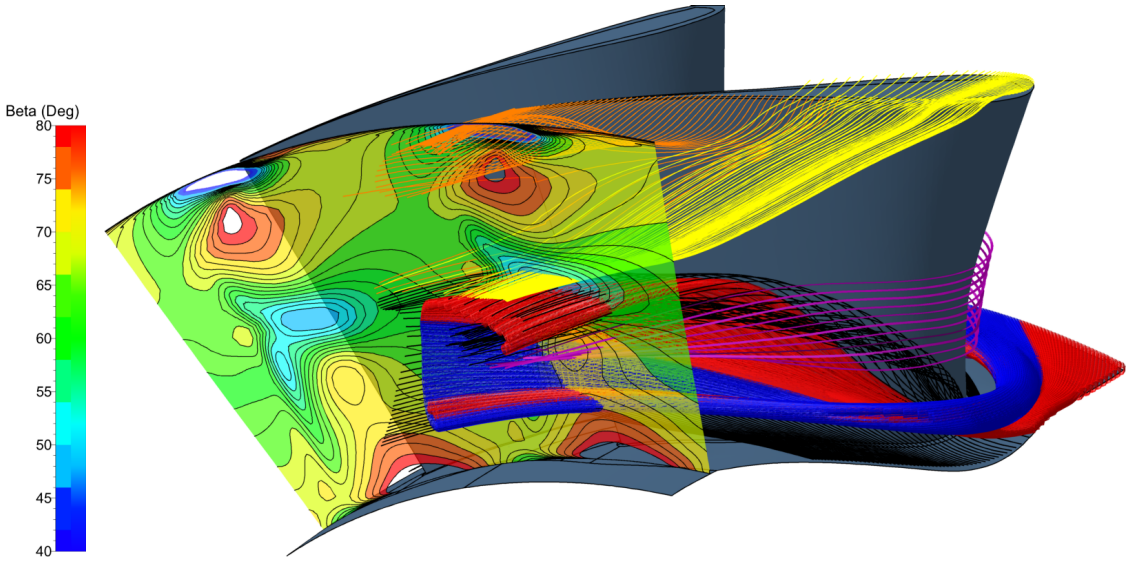

(b) Contoured endwall

Figure 6.9: Increased loading case: Stream tubes showing rotor exit relative outlet flow angle at rotor exit

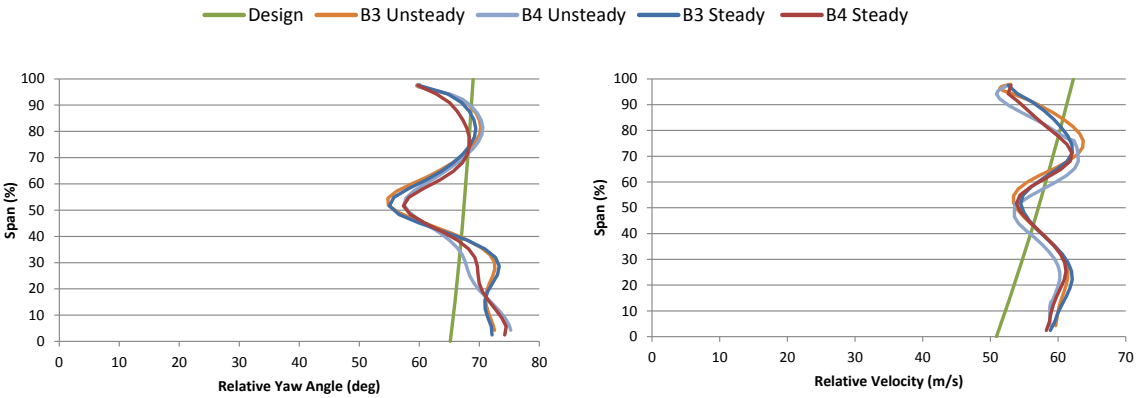

(a) Relative outlet flow angle (b) Relative velocity magnitude

Figure 6.10: Increased loading case: Comparison of steady and unsteady CFD results

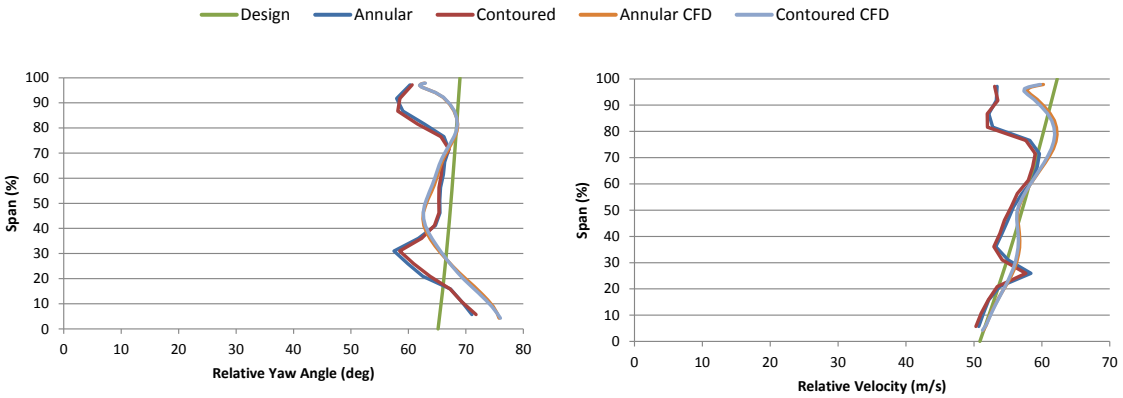

(a) Relative outlet flow angle (b) Relative velocity magnitude

Figure 6.11: Decreased loading case: Comparison of unsteady annular and contoured CFD and experimental results

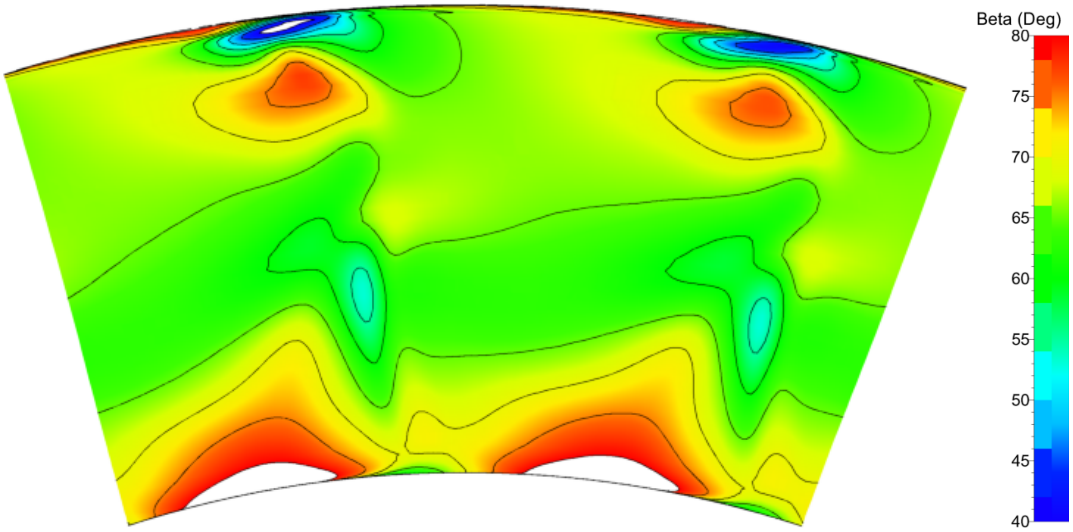

(a) Annular endwall

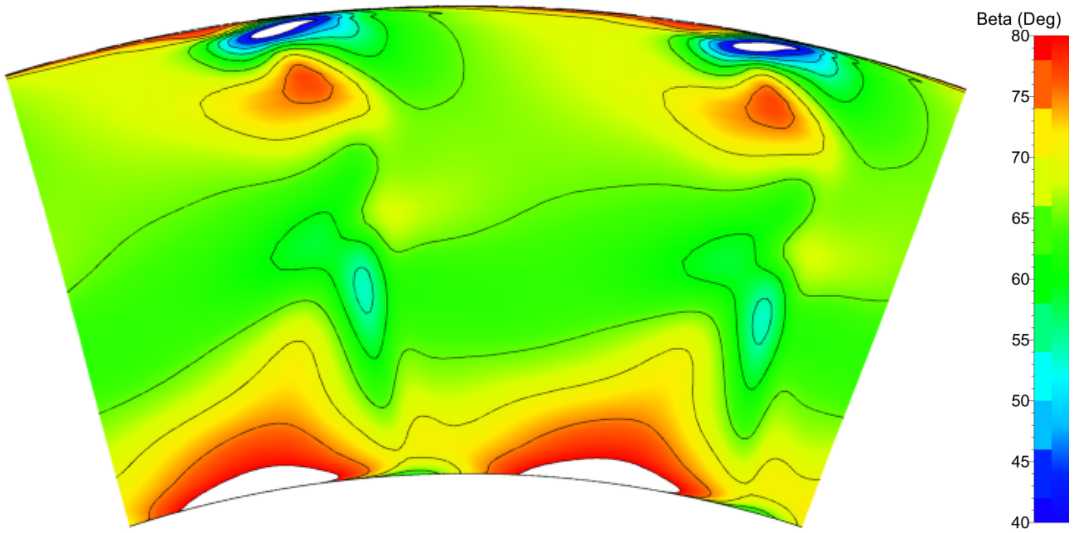

(b) Contoured endwall

Figure 6.12: Decreased loading case: Comparison of annular and contoured outlet flow angle contours

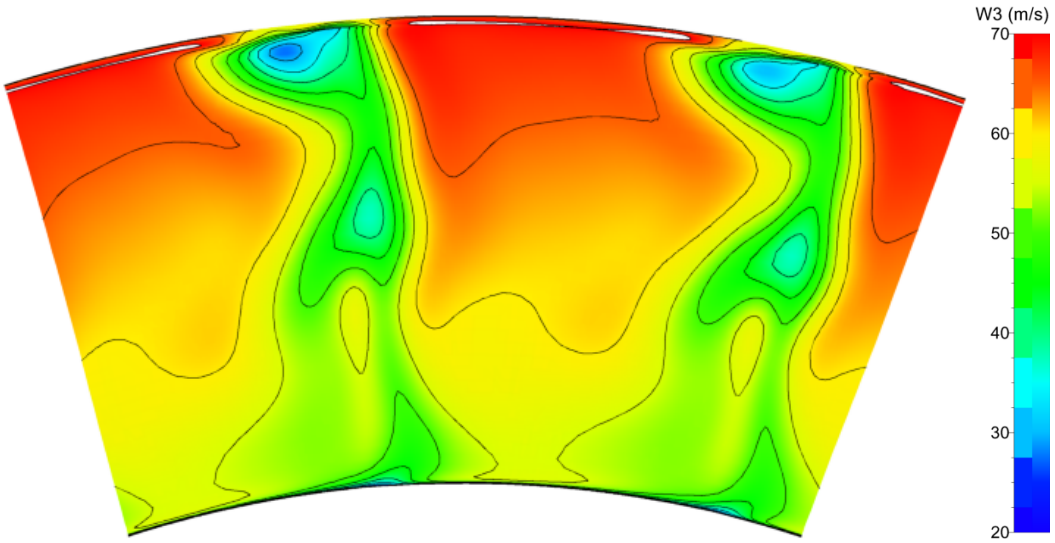

(a) Annular endwall

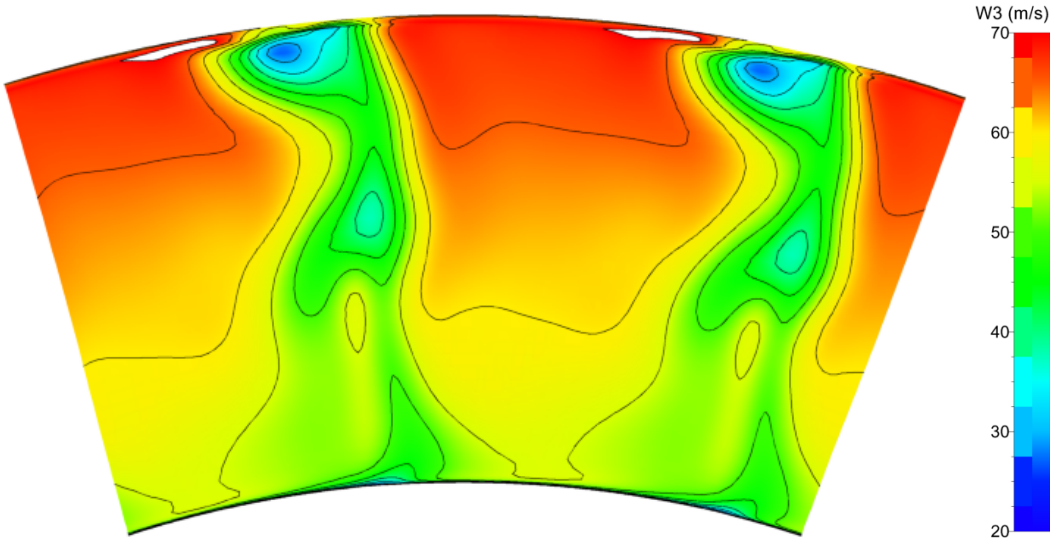

(b) Contoured endwall

Figure 6.13: Decreased loading case: Comparison of annular and contoured relative velocity magnitude

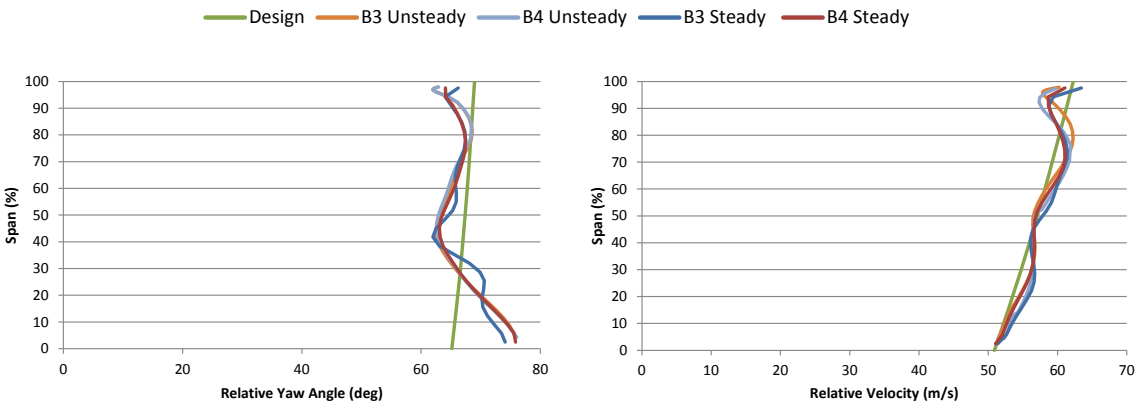

(a) Relative outlet flow angle (b) Relative velocity magnitude

Figure 6.14: Decreased loading case: Comparison of steady and unsteady CFD results

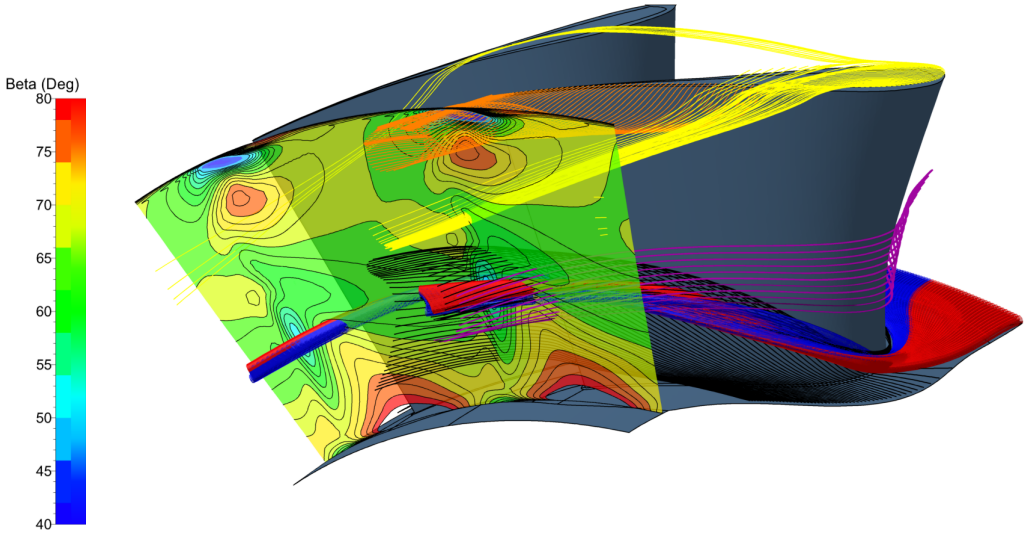

(a) Annular endwall

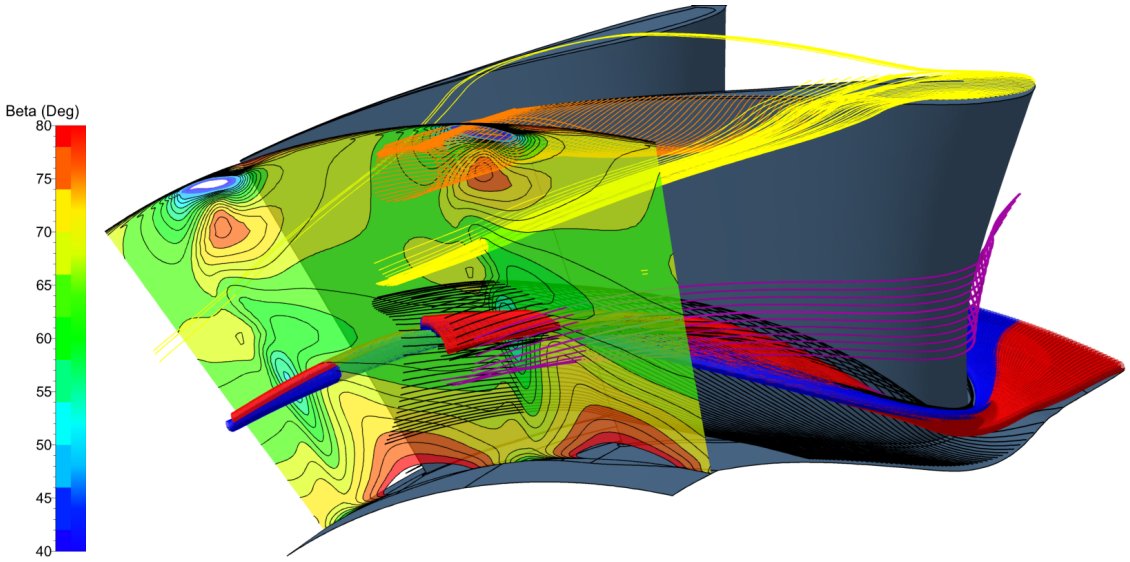

(b) Contoured endwall

Figure 6.15: Decreased loading case: Stream tubes showing rotor exit relative outlet flow angle at rotor exit

6.2 Time dependent blade pressure profiles

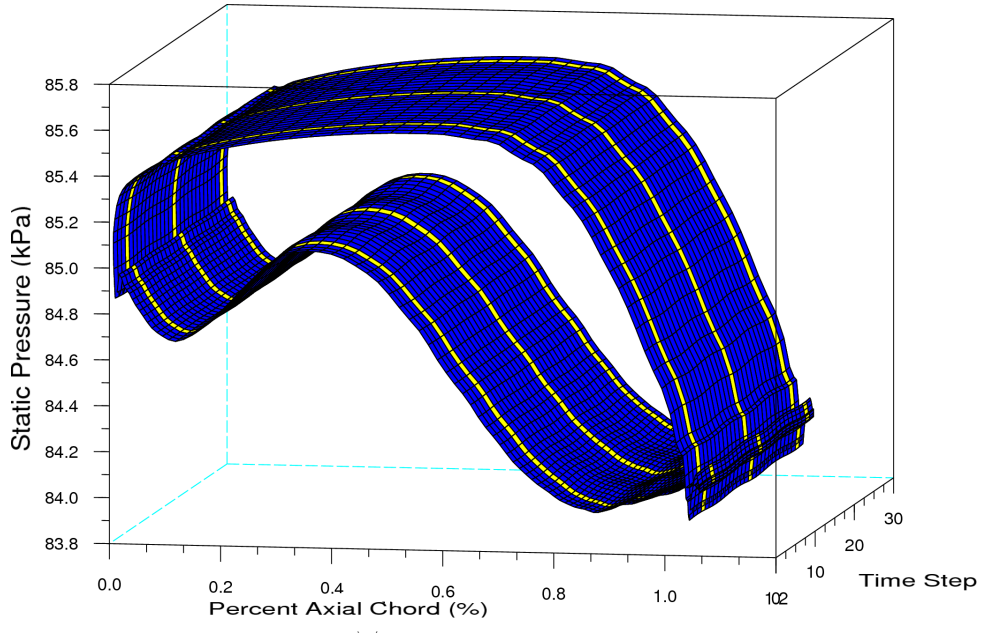

(a) Annular rotor

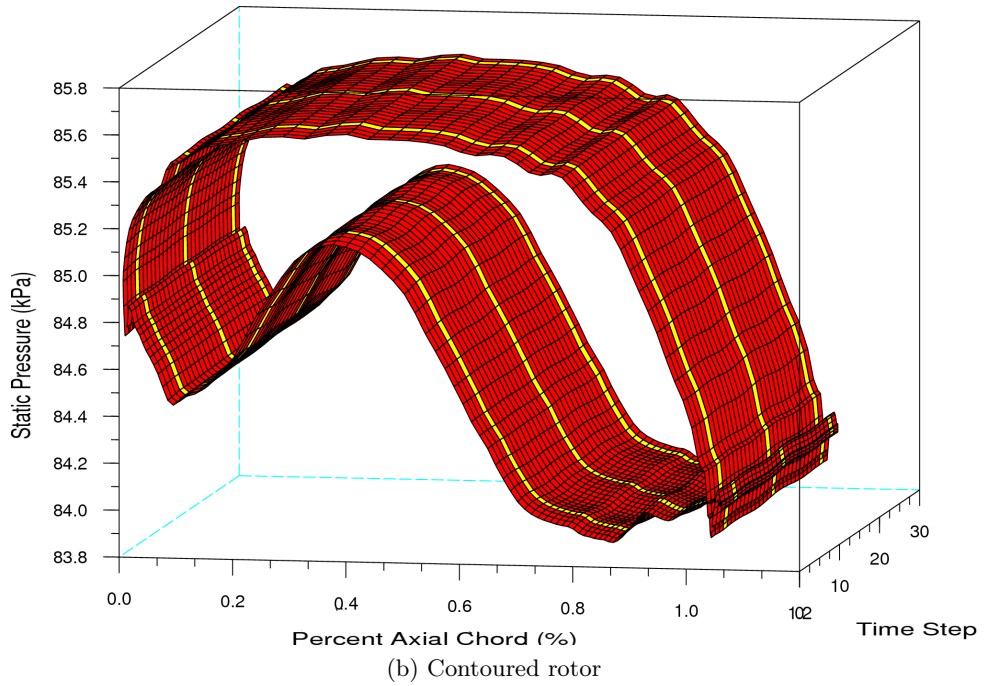

(b) Contoured rotor

Figure 6.16: Design case: Time varying blade pressure profile plots at 0 % span

Since the contouring alters the cross passage pressure gradient, it was thought that there might be some new unsteady features present in the blade pressure profiles. Figure 6.16 shows the blade pressure profiles at the hub. The pressure profiles have been plotted

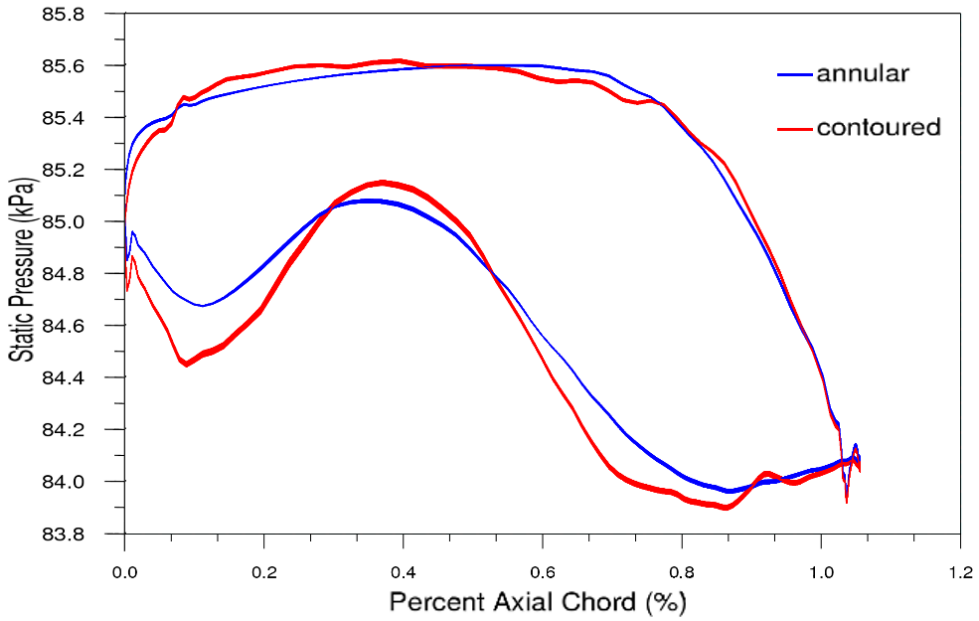

Figure 6.17: Design case: Comparison of unsteady annular and contoured blade pressure profiles at 0 % span

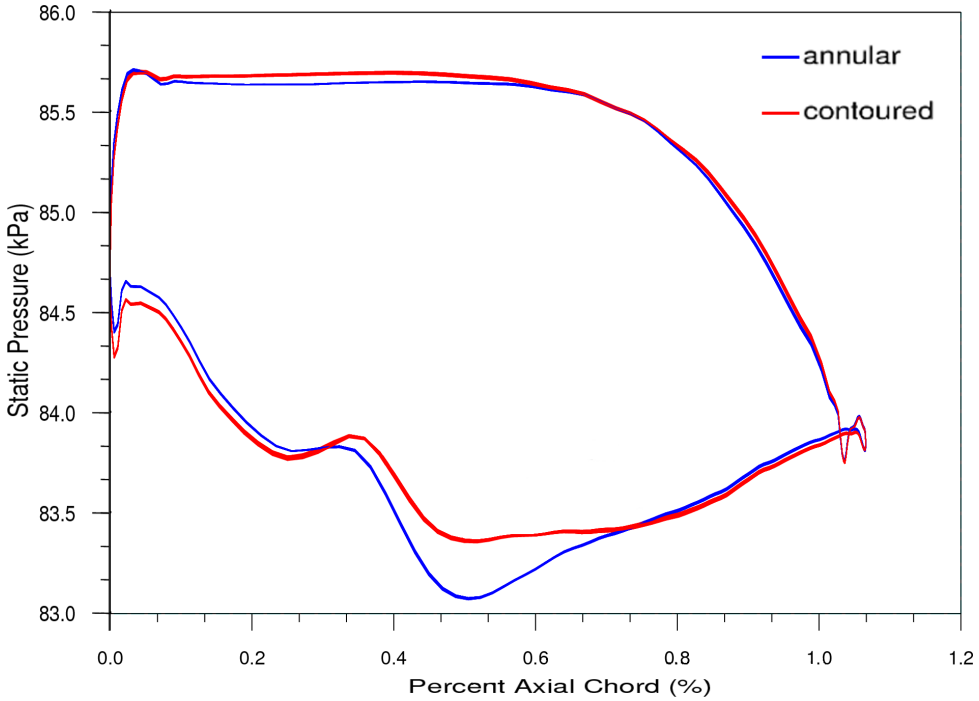

Figure 6.18: Design case: Comparison of unsteady annular and contoured blade pressure profiles at 25 % span and $y = 0.17mm$ off the blade

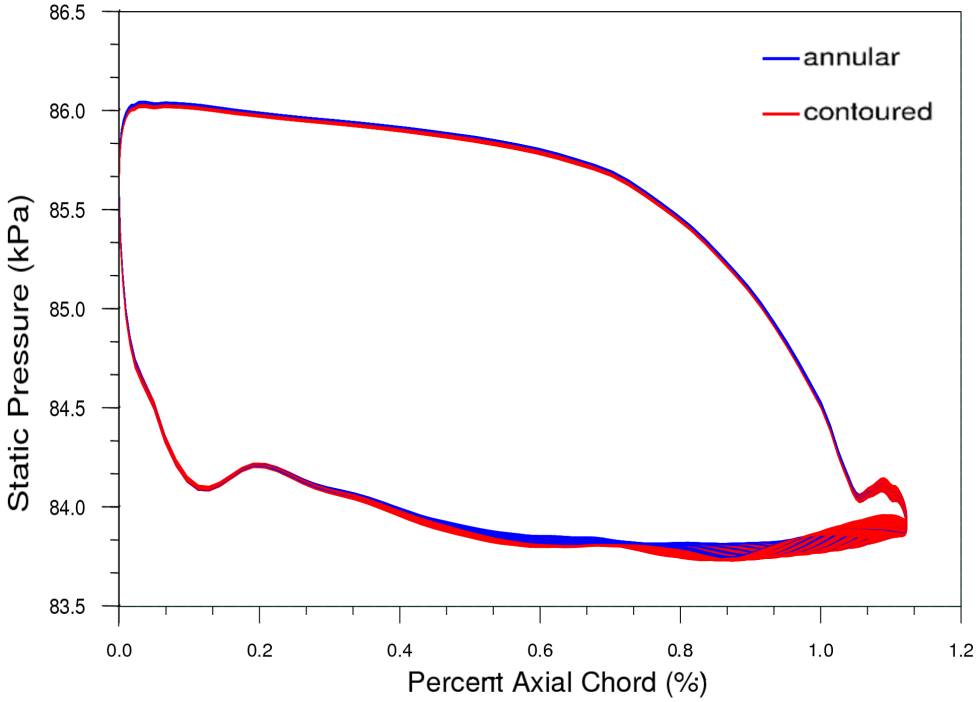

Figure 6.19: Design case: Comparison of unsteady annular and contoured blade pressure profiles at 50 % span and $y = 1.15mm$ off the blade

as a surface plot so as to indicate the change with respect to time (the axis going into the page). The yellow stripes seen on the surface plots indicate the location where the trailing edge of the upstream stator was in-line with the leading edge of the rotor. Due to phase lag and transit time this was not the location that the wake impinged on the leading edge. The location was included to indicate the blade pitch.

Looking at both of the blade pressure surfaces in Figure 6.16 it is evident that the oscillations were very small. To get a better idea of the level of the oscillations the surface plots in Figure 6.16a and 6.16b were combined (the colour was kept the same, the annular profile is blue and the contoured is red), and viewed as a 2D plot, shown in Figure 6.17, with the time axis going into the page. The resulting blade pressure profile now conveys the blade pressure with respect to axial chord and the thickness gives and indication of the amount of oscillation to be expected.

Again it can be seen in Figure 6.17 that the level of oscillation was very low, with the peak oscillation of the order of 10's of Pascals and was deemed to be negligible. Looking at the blade pressure profiles it can be seen the the cross passage pressure gradient between approximately 30 % and 60 % span has been reduced by the blade contouring. The blade has also become forward and aft loaded. Front loading of a high lift rotor has been shown to be advantageous from a blade midspan performance perspective and offered a good stall characteristic for a wide operating range (Knezevici *et al.*, 2009). Front loading has also been shown to reduce profile losses (Howell *et al.*, 2000) while aft loading reduces secondary flows (Pullan *et al.*, 2005).

In an attempt to identify unsteady effects the blade pressure profiles were also obtained closer to midspan at 25 % span and $0.17mm$ off the blade, shown in Figure 6.18. At this spanwise location and slightly off the blade there is less influence of the boundary layer and

the zero velocity on the wall condition numerically imposed. As can be seen the shape of the blade pressure profile has changed but the level of the oscillations has remained negligible. The contoured blade pressure profile still shows a reduced cross passage pressure gradient, however, the blade is only marginally forward and aft loaded compared to the annular case.

Mid-span pressure profiles further off the blade (at $y = 1.15mm$ off the blade) were also taken, shown in Figure 6.19. The pressure profiles did not show much oscillation except for the last 60 % axial chord on the suction surface while the pressure surface remained undisturbed. Lott *et al.* (2009) also found that the rotor wakes only had an effect at about $\frac{2}{3}$ of axial chord from the leading edge of the stator. The oscillations observed in the pressure profiles of the annular and contoured case, however, were of similar magnitude, resulting in nothing significant being observed.

The lack of oscillations seen in the pressure profiles presented above were due to the small difference about the average value not being able to penetrate the boundary layer, which would be of concern from a heat transfer point of view. Liu and Rodi (1994) performed an experimental investigation into wake induced unsteady flows in a linear cascade and found that the state of the boundary layer was relatively unchanged with time, but the turbulence level in the boundary layer did respond to the passing wakes, similar to the finding of Addison and Hodson (1990*b*).

6.3 Time dependent results

The discussion in this section makes reference to the animations that can be found in the digital appendix, Appendix A. The animations were generated by capturing a screenshot for each time step the presented the required view showing the required quantity. These screenshots were then stitched together to create an animation. The animations were generated from 30 separate time steps that represented two rotor blade passings (two rotor pitches).

FINE^{TM}/Turbo v8 unfortunately did not have the capability to change the viewing reference frame. The "camera" was always in the absolute reference frame making relative reference frame viewing of unsteady data require user scripts to rotate the camera at each time step. The camera location gets specified using unit vectors to specify direction and camera locations. These vectors get specified using six decimal places which was insufficient for the geometry used. For this reason some of the animations presented appear to jump.

Not all the quantities were specifically discussed, but were included for completeness. Only those quantities which could be measured experimentally were discussed.

6.3.1 Design Condition

The time dependent streamlines and streamtubes as presented in Figure 6.5 show very similar oscillations about a mean value. The largest oscillations can be seen in the tip leakage region due to the upstream stator wake passing through the tip gap.

The unsteady rotor exit relative exit flow angle (Slide 13) show a very stable endwall secondary flow vortex. The oscillations observed coincide with the blade passing frequency. The endwall secondary flow vortex does not move, however, it pulsates about the mean value. Slide 18 and 19 show two views of the endwall secondary flow vortex. The difference with respect to time in the endwall secondary flow vortex is primarily driven by the blade passing frequency, as was seen in the experimental results.

Looking at the rest of the results it is evident that this was the case through out. Where an unsteady effect was visible in the annular case, a similar effect was seen in the contoured case.

6.3.2 Increased Loading Condition

The oscillations observed for the increased loading condition show a similar trend to those of the design condition, but the magnitude of the change was larger due to the a higher load condition. The time dependent oscillations of the annular case were again similar to those of the contoured case.

6.3.3 Decreased Loading Condition

The decreased loading case again shows a similar trend as seen previously. The annular and contour results oscillate about a mean value with nothing new being evident. There does, however, appear to be a discontinuity in the last few images that make the time dependent results questionable. The time average as presented previously does not appear to be affected though, correlating well to the unsteady experimental results. Due to the low level of secondary flow evident in the decreased loading case it was felt that re-running the simulation would not bring any new information to light.

6.4 Discussion and Conclusions

The numerical results have shown that the contouring applied to the rotor has improved (become closer to design) the flow field of the rotor exit. By reducing the strength of the cross passage pressure gradient, the endwall secondary flow vortex has been reduced in both size and magnitude. The reduction in size resulted from a less tightly wrapped endwall secondary flow vortex which allowed the vortex to be distributed more in the radial direction. A more radially distributed endwall secondary flow vortex redistributed the momentum of the flow producing a more uniform rotor exit velocity profile.

The oscillations in the flow do not penetrate the boundary layer due to the low level of oscillation observed. With the state of the boundary layer unchanged there is the potential that the heat transfer characteristics for the blade of an annular rotor will match that of the blade of a contoured rotor.

Looking at the results presented it was evident that currently turbulence models were still not capable of accurately predicting the flow field in a turbine. The test rig used for this investigation operated at a low Mach Number and Reynolds Number operating at ambient temperature making compressibility and Reynolds effects small. Even under these simplified conditions the correlation was not ideal, leaving an obvious requirement for a more accurate turbulence model.

The unsteady numerical results presented correlate well with the steady numerical results, with the largest differences occurring in the endwall secondary flow region of the annular rotor. The steady annular results predicted a larger endwall secondary flow vortex than the unsteady annular results making it easier to identify the endwall secondary flow vortex in the steady numerical results. Looking at Figure 5.4 it can be seen that there was a larger difference in results from using a different turbulence model than changing the endwall design.

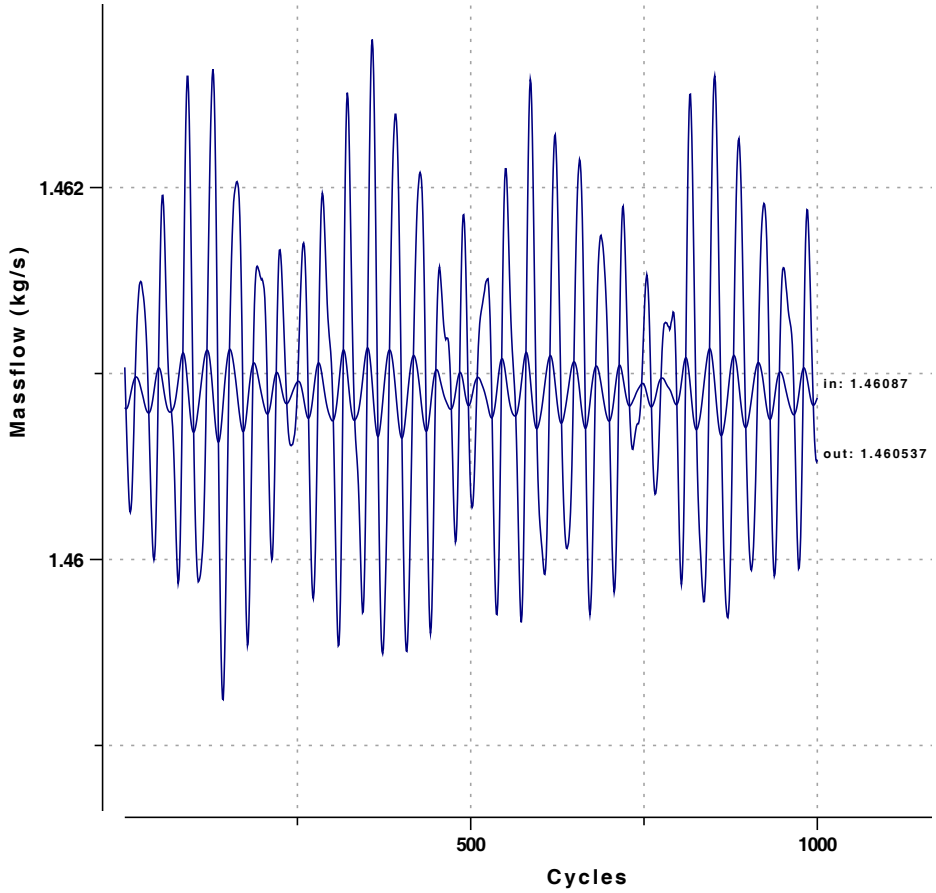

Figure 6.20: Example of the oscillating massflow residual from the design case Spalart-Allmaras steady simulation

After scrutinizing the numerical results it was found that the tip leakage flow difference found experimentally was not due to the endwall contouring but instead due to flexing of the trailing edge of the rotor blades. The steady numerical results, however, showed that there was a difference in the annular and contoured tip leakage flow as well. It was felt that the difference could potentially be caused by unsteadiness (or separation) in the flow that could not be appropriately dealt with. The trailing edge of a turbine blade causes a von Karman vortex street to develop (Cicatelli and Sieverding, 1996). The vortex street combined with the tip leakage flow at the trailing edge creates a very localized unsteady flow field that the steady state solver struggles to resolve, creating an oscillating residual.

An example of the oscillating residual can be seen in Figure 6.20, it is evident that the solution was converged (error in massflow was 0.023 % depending where the solution ended the difference could be larger or smaller). It was these oscillation that were thought to be the cause of the differences in the tip leakage flow. It is expected that by using a finer mesh that increases the number of cells in the wake region would reduce this difference by better capturing the flow field. Alternatively using a solver that can handle wake type flows in a steady simulation, like the non-linear harmonic method would remove these oscillations and insert them into the time domain, allowing for a more accurate time average to be generated.

Chapter 7

Discussion

The current drive to improve fuel consumption (and efficiency) has lead to increased blade loading due to the reduction in blade numbers. As blade loading increases and as compressibility effects become significant so too does the potential for unsteady interactions in turbomachines (Japikse, 1986). Unfortunately increased blade loading has the side effect of increased secondary flows. In previous investigations by Ingram (2003) and Snedden (2011) it has been shown that non-axisymmetric endwall contouring could help control the cross passage pressure gradient resulting in a reduced endwall secondary flow vortex. The current investigation found that this was true even when looking at the time dependent results.

7.1 General discussion

The current investigation has shown that the endwall contour tested has improved the flow field in several ways, namely: The velocity magnitude of the endwall secondary flow vortex was reduced; the over-turning of the flow was reduced at the hub; the level of the oscillations was reduced and the temporal variation in the flow was reduced. The result was a more radially and temporally uniform velocity profile which in turn improves the incidence angle distribution of the downstream blade rows.

The reduction in the variation in the velocity measured produces a more uniform inlet flow for the downstream blade rows. The variation in the velocity would be seen by the downstream blade row as being a change in flow incidence angle, from positive through zero to negative. The varying incidence angle changes the lift (which results in the torque produced by the turbine rotor) which is produced by the individual blades (Japikse, 1986). Having a varying blade lift results in a fluctuating blade load. Saravanamuttoo *et al.* (2009) states that flutter is any self-excited oscillation of a lifting surface. The implication of this is that endwall contouring could be used to delay flutter. Since the majority of the change occurs close to the endwall where the load required to induce flutter is greater the impact will be small. It should be noted that this would be of more interest for compressor blades, as typically turbine blades are not susceptible to flutter due to the blades being sturdier. In addition it is expected that designing the endwall contour for a specific frequency would be time consuming and difficult.

The fluctuations in lift generate moving pressure patterns which would have an impact on noise generation (Japikse, 1986). The difference in the acoustic noise level wasn't measured in the current investigation due to the high noise level of the test rigs auxiliary

equipment (the hydraulics being a large contributor). Due to the small change in the oscillation observed between the annular and contoured data set and the low Mach Number and low temperature (compared to a real engine) the decrease in noise would be very low. Engine noise during flight and take-off is dominated by the mixing of the high velocity jet stream mixing with the cold atmospheric air, whereas during landing it is dominated by fan noise (Saravanamuttoo *et al.*, 2009). Endwall contouring therefore will not have as large an impact as say compressor casing treatments, but designed properly for a transonic turbine potentially could produce a beneficial result.

Since the losses and heat load on the turbine airfoil surfaces are increased by the unsteady interactions from upstream blade rows (Sharma *et al.*, 1988), these will be reduced by the smaller fluctuations experienced with the contoured rotor. Influence of endwall cooling holes on the contoured rotor endwall secondary flows would need to be investigated first.

The unsteady experimental results reiterated the difference between the annular and contoured tip leakage flow as seen in the steady (both experimental and numerical) results of Snedden (2011). However, the unsteady CFD did not reproduce this difference in the tip region. After inspection it was found that the turbine blades (which were manufactured from a laser sintered nylon) were bending during testing. The bending occurred so as to increase the axial chord of the blade, which resulted in under-turning of the flow as seen in Figure 4.1a. Without further investigation it remains speculation that the difference in the annular and contoured tip leakage flow was due to this bending. The shape of the contour and the fact that the contoured blade exhibits an aft loaded pressure profile lends credence to the speculation. It needs to be pointed out, however, that the difference in annular and contoured blade pressure profile becomes negligible above midspan (as seen in Figure 6.16 to 6.19).

Hilfer *et al.* (2012) found a similar difference in the tip leakage flows in the Durham cascade and stated that there was an improvement (reduction) to the loss in the tip region. Looking at the yaw angle presented in Hilfer *et al.* (2012) shows that above 280 *mm* (approximately 75 % span) the difference in the annular and contoured results (both numerical and experimental) was marginal, with the CFD results being indistinguishable from each other. The CFD did not predict the loss correctly, indicating an increase in the loss for the contoured case. This highlights the problem of using efficiency (and loss) as an objective function. If the CFD can not predict it accurately then using CFD to optimise to reduce loss (and improve efficiency) will lead to erroneous results. As highlighted in Snedden *et al.* (2010*b*) serious consideration needs to be taken when choosing an objective function.

As mentioned earlier secondary flow structures develop on both the casing and the endwall (at both ends of the blade). Viewing the streamtubes in Figure 6.5 and 6.9 it was observed that the the tip leakage flow moved down to meet with the endwall secondary flow vortex structure resulting in a flattened endwall secondary flow vortex. It was noted that the contour spreads the vortex structure more radially, but the redistribution stops at about midspan where the endwall secondary flow from the casing and hub meet. It remains to be seen whether this improves or deteriorates the loss reduction found. An improvement would be caused by a further redistribution of the endwall secondary flow system radially making for a more uniform flow. Since the two endwall secondary flow vortex systems meeting at midspan they could potentially prevent the flow from under-turning further than it has.

7.1.1 Unsteady analysis

Experimental comparisons

The unsteady analysis highlighted a few inaccuracies in the 5 hole probe measurements. The most significant of which was the inability to capture the highly sheared flow in the endwall secondary flow vortex system and the tip leakage flows, something noted by Van Den Berg and Bertelrud (1988). The 5 hole probe used had a head diameter of 1.59 mm which is larger than the tip gap (1 mm) which potentially means that one of the pitch ports would be in line with the blade, and the other in line with the tip gap. The pressure transducer connection method used, while it measures the lowest possible pressure (which reduces the magnitude of the error which is specified as a percentage of measured range) does not allow for accurate measurement of the static pressure. The yaw ports were connected to a single pressure transducer to obtain the differential pressure, which means the static pressure was taken as being the average of the pitch ports. If the probe is in a region of high shear then the static pressure could potentially be incorrect. The hotfilm on the other hand allowed for direct measurement of the axial and tangential velocity (and therefore the yaw angle) providing a more accurate indication of the rotor exit flow angle. The commercially available hotfilm probes can only measure 2D cross flows resulting in the radial velocity being omitted. The 5 hole probe measurements showed that the radial velocity was generally small with the tangential and axial velocities dominating the flow.

The FFT data presented showed that the major unsteady feature was the blade wake. The magnitude of the harmonics of the blade passing frequency fluctuated about the uncertainty and thus could not be used to draw any conclusions. Below midspan the magnitude of the velocity of the contoured rotor at the dominant frequency was reduced, indicating a reduction in the amplitude of the oscillation of the rotor exit flow. Other than this, little new information was obtained in the unsteady experimentation that was not observed in the steady state experiments.

The reduced frequency can be used to determine if a turbine is inherently steady, unsteady or in a state where it is both steady and unsteady as it gives a measure of how important unsteady effects are when compared to steady (or quasi-steady) effects. It was calculated using (Japikse, 1986):

$$\Omega = \frac{\omega L}{\overline{C}} \tag{7.1.1}$$

Where ω is the rotational velocity, L: is the relevant length (chord in this case) and $\overline{C}$ is the through flow velocity (axial velocity in this case). When $\Omega < 1$ the unsteady effects are minimal and the flow can be considered to be quasi-steady; when $\Omega > 1$ the unsteady effects dominant and when $\Omega \approx 1$ both steady and unsteady effects are of importance. The reduced frequency was calculated as being $\Omega = 0.958$, which is sub-critical yet close to 1, and thus steady flow can be assumed but with some unsteady effects. This was manifested by the low level of unsteadiness in both the annular and contoured rotor and stator exit flow. The reduced frequency thus should be calculated in order to determine if the time cost associated with unsteady analysis is warranted. Schlienger *et al.* (2005) found that unsteady analysis does provide information not obtained by steady analysis and thus has merit. Unfortunately insufficient information was provided to calculate the reduced frequency in order to comment.

Unsteady experiments also produce large quantities of data. Each of the investigations

done (i.e. a given operating condition with a given rotor) produced over 2 gigabytes of unprocessed data. Conversion of the voltage to velocity took in excess of 6 hours on a 3.0 GHz dual core Pentium with the test itself only lasting 2 hours. The resulting files can then be processed into a meaningful set of results, which in total takes almost two hours on the same hardware. This is after a 5 hole probe experiment was performed to determine the yaw angle offsets required to keep the flow in the hotfilm probes cone of acceptance. A large amount of effort was put into a single experiment that produced a similar understanding to that obtained by a steady state experiment. For this reason it was felt that unless the reduced frequency becomes much larger than one, or unsteady inlet conditions are used that steady measurements be used for testing.

Numerical Comparison

A similar argument can be made for the unsteady numerical work. The steady state CFD took less than 12 hours of simulation time to converge, where as the unsteady CFD took in excess of 2 weeks simulation time. The time averaged results compared well with the steady state simulations, and the oscillation of the annular and contoured rotors were comparable. A large difference in the results was observed using a different turbulence model than was observed between the steady and unsteady simulations. Again unsteady inlet conditions or a change to the setup such that the reduced frequency is much larger than one would warrant an unsteady solution.

It should be noted that the non-linear harmonic method as used in FINE^{TM}/Turbo does produce a more accurate solution than the steady solver produces because it solves for the fluctuations which end up as harmonics in a Fourier series (Numeca, 2007). It requires more transport equations to be solved (based on the number of harmonics to be solved) but solution times are still comparable to those of steady state simulations.

Turbulence models still do not adequately predict the turbulent aspects of the flows in a turbine (Schobeiri *et al.*, 2012) also commented on this. Turbulence models are typically optimised for a specific set of applications or flow regimes (Versteeg and Malalasekera, 1995) and offer poor agreement in other flows. Unfortunately turbines have combinations of these undesirable flow regimes. For example impingement flows at the leading edge, vortical flow in the endwall secondary flow region, as well as the tip leakage flow, boundary layer transition and separation, jetting (highly sheared) flows through the tip gap to name a few. Until turbulence models are able to better predict the flows in a turbine unsteady analysis of this scale and flow regime is impractical. The steady state solutions using different turbulence models currently show more difference compared to the experimental than the unsteady do compared to the steady state results. Schobeiri *et al.* (2012) states that in order to accurately capture the complex flow physics in a turbine direct Navier-Stokes simulations are required, but large eddy simulation can be used to a certain extent. These methods are very time consuming and are not currently practical for engineering purposes especially when several design iterations are required.

Unsteady Losses

In order to calculate the loss (or efficiency) pressure and temperature are required To address this some researchers (Behr *et al.*, 2006; Porreca *et al.*, 2006; Rose *et al.*, 2013) have used a FRAP probe to take unsteady pressure measurements, allowing for loss determination. Unfortunately FRAP probes were not a possibility in the current investigation.

Effects of change in loading

Table 7.1: Difference of the experimental annular and contoured rotor velocity at 31 % span based on the annular case

Loading Condition RPM	C_t velocity %	C_x velocity %	Velocity magnitude %
Increased	-0.37	-7.98	-7.77
Design	-10.46	-6.12	-6.71
Decreased	19.77	-4.24	-4.16

Table 7.1 shows the percentage change in velocity experienced by the rotor with the addition of the contour at 31 % span (location of the peak over-turned flow for the annular case). All the loading conditions have shown some level of improvement, with the largest improvement occurring at the high loading condition. The decreased loading condition tangential velocity at 31 % span was increased, but the tangential velocity was small ($C_t = -1.14\ m/s$ for the annular case) making the difference negligible, even though the percentage change was large.

Since the smallest change happens at the lowest load (highest speed, 2820 RPM), with an increase in effectiveness which increases with load, it was felt that it would prove beneficial to design the contour for the decreased loading condition instead of for the design loading. Typically a civil aviation engine will only operate at maximum speeds for a short time to increase engine life. The cruise speed (decreased loading) is preferred, which operates at a lower load which is more efficient and is used for the majority of the flight (Saravanamuttoo *et al.*, 2009). With the endwall designed for cruise conditions any benefit achieved will have a large benefit at increased loads. In addition to this the improvement seen in the decreased loading case was small (negligible in the CFD results), so an endwall contour that creates an improvement would be worthwhile utilising. If for the decreased loading case only a negligible improvement could be obtained then it brings into question whether the added design and manufacturing costs make economical sense.

7.1.2 Experimental challenges

During the testing is was found that hotfilm testing was not the ideal method of sampling the data. Hotfilms are very fragile and as such break easily invalidating the current test. The sensor oxidizes relatively quickly making long tests prone to drift in the calibration. It was found that a two hour test had negligible difference in calibration and thus the tests were kept to under two hours. The results presented in this investigation would reveal more definition in flow features if the sample grid could be larger (smaller spacing between sample points). Before hotfilm testing can commence a good indication of the variation in the flow is required to ensure that the flow is always well within the cone of acceptance of the probe. With a pressure probe it is possible to null yaw the probe (by enforcing a small difference between the yaw ports) using the rig control software. Where as with the hotfilm due to the large bandwidth required and the need for proprietary software to be run in conjunction with the test rig control software it was operated on a separate computer meaning that null yawing would have to be done manually. Manually null yawing the

probe would result in more time per test, which as discussed above increases the likelihood that the sensors would break or calibration would drift.

The spacial resolution of the experimental sample grid was sufficient to resolve the endwall secondary flow vortex system, but a finer grip would provide a better indication of inflection points and improve the resolution of the image. As mentioned the hotfilm probe does suffer from life span problems that reduce effectiveness of the probe the longer it is in operation. To address this either a Fast Response Aerodynamic Probe (FRAP probe) or Laser Doppler Anemometer (LDA) show promise since they do not require a fragile or heated element to be present in the flow.

Another shortfall of hotfilm probes being used for investigating loss in a turbine is that they only provide velocities and not the pressure and temperatures required for loss calculations (as mentioned above). A desirable proxy for loss is thus required which would allow only velocity measurements to determine whether the loss has been increased or decreased.

7.2 Evaluation criterion

As previously discussed, the efficacy of endwall contouring is usually evaluated by comparing quantities such as efficiency (either total-to-total, or total-to-static), pressure loss, coefficient of secondary kinetic energy (C_{ske}) and so on, (Snedden *et al.*, 2010*b*). All except C_{ske} require temperature or pressure, or both, neither of which lend themselves to unsteady measurement in the experimental test rig. The temperature drop for the flow regime was small compared to ambient conditions and unsteady pressure measurement, while not impossible, was impractical. It was previously noted by Dunn *et al.* (2010) that for the design operating conditions small changes in temperature and pressure cause a large change in efficiency (as shown below). Therefore an alternative was required that could give an indication in the losses incurred that did not require temperature or pressure.

The isentropic efficiency problem

The stage total-to-total isentropic efficiency can be calculated using (Saravanamuttoo *et al.*, 2001):

$$\eta_{stage} = \frac{1 - \frac{T_{total3}}{T_{total1}}}{\left(1 - \frac{P_{total3}}{P_{total1}}\right)^{\frac{\gamma - 1}{\gamma}}} \tag{7.2.1}$$

Where T_{total} is the total temperature, and P_total is the total pressure. The subscript 1 indicates stator inlet (stage inlet) and 3 indicates rotor exit values.

The stage temperature difference (temperature across inlet stator and rotor) in the CFD was approximately $\Delta T = 2.5°C$. Upon inspection of Equation 7.2.1 it was noted that with such a small temperature difference, any error in the temperature equates to a large efficiency change. An error in temperature of $\Delta T = 0.1$ % equates to a change in stage total-to-total efficiency of $\eta_{stage} = 10.8$ %. If the same error (0.1 %) occurs in pressure, the change in stage total-to-total efficiency of $\eta_{stage} = -2.7$ %.

7.2.1 Design efficacy

Watanabe and Harada (1999) proposed an inverse design method aimed at reducing secondary flows that involved designing the blade so as to control the spanwise distribution of circulation ($r\bar{C_w}$) and blade thickness. It was found that this method reduced the secondary flows without changing the spanwise distribution of work. The inverse design method that was proposed however, was used to determine the blade stacking and lean. Unfortunately since tangential velocity was used scaled with radius, under and over turning were not taken into account (except by appropriate specification of the desired distribution of the circulation) neither were radial velocities inherent in vortical flows.

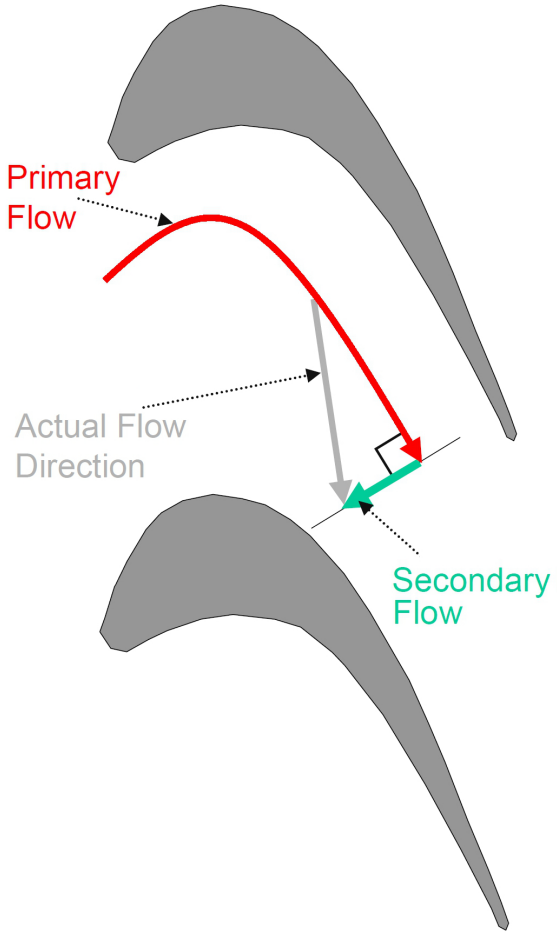

Figure 7.1: Simplified definition of secondary flow adapted from Ingram (2003)

In order to determine the efficacy of the endwall contouring, a new method is proposed that is based on one main assumption: "The design condition can be considered to be the ideal flow condition for a given mass flow rate, providing the maximum amount of work for a specified inlet mass flow rate". While the assumption is not always necessarily true it does assist in providing the downstream blades with flow that has the correct incidence. Secondary flows can be defined as flows that deviate from the primary flow (Ingram, 2003), as shown in Figure 7.1. It was thus felt that this assumption was valid since blade design is usually done at several radial stations with the gas angles adjusted to account for increase

in the blade speed, U, and the varying static pressure due to the whirl component of the flow (Cohen *et al.*, 1996). The blade design is done based on the velocity triangles in the plane of the blade cross section. For a given mass flow, any off design flow would have to originate from a decrease in either the axial or the tangential velocity, or a combination of the two.

The stage work, W_S, for a turbine can be calculated by applying the principle of angular momentum to the rotor (Saravanamuttoo *et al.*, 2001), i.e. work is the change in momentum through the rotor. The stage work can be written as (Saravanamuttoo *et al.*, 2001):

$$W_s = U(C_{w2} + C_{w3}) \tag{7.2.2}$$

Where U is the blade speed, C_{w2} is the whirl component of the flow exiting the stator and C_{w3} is the whirl component of the flow exiting the rotor. The change in the axial component of velocity across the rotor produces a thrust on the rotor, where as the whirl component produces the torque.

Using the principle of Watanabe and Harada (1999) and expanding it to include all three velocity components as well as some measure of the design flow condition, a new quantity was arrived at design efficacy, η_{de}. The purpose of design efficacy is to determine how much of the flow exiting the turbine conforms to the design exit flow conditions. Thus the design efficacy can be defined as the amount of flow that corresponds to the design flow conditions. In other words to what extent does the vector sum of the three velocity components measured/calculated correspond to the design velocity components.

In order to determine the extent of the conformity, the velocity must be resolved to the design flow direction. To determine the extent to which the flow field matches the design flow conditions, it would require that the design conditions as well as the velocity field obtained be combined. To facilitate this the design blade outlet gas angle was decomposed into a unit vector:

$$\overrightarrow{\theta_D} = cos(\alpha_D) \cdot i + sin(\alpha_D) \cdot j + cos(\phi_D) \cdot k \tag{7.2.3}$$

Where α_D is the design yaw angle for the current radial location and ϕ_D is the design pitch angle, which is $\phi_D = 0$ for the test turbine. The evaluated velocity field then gets included via the dot product:

$$\eta_{de} = \frac{1}{n_{span}} \sum_{span} \frac{1}{n_{B2B}} \sum_{B2B} \left(\frac{\overrightarrow{\theta_D} \cdot \overrightarrow{V_E}}{V_{D,max}}\right) \tag{7.2.4}$$

Where n is the number of values being summed, $\overrightarrow{V_E}$ is the evaluated/expected velocity (in vector form) and $\overline{V_D}$ is the design velocity magnitude at the same radial location in the same direction as the component of $\overrightarrow{V_E}$ being dealt with. By dividing the expected/evaluated velocity by the maximum velocity magnitude, η_{de} becomes normalised to the range of 0 to 1 to simplify comparisons. It also allows for comparisons when the flow rate is different. Equation 7.2.4 can then be averaged in the spanwise direction to obtain an overall average or plotted against span to determine the region of highest efficacy.

Thus the velocity of the evaluated/expected flow field is weighted according to the design flow angle of the blade for a given radial location. The closer the evaluated/expected flow field is to the design flow field, the closer the design efficacy is to unity and the work

is at a maximum. The averaging is done in a two stage process to allow for spanwise distributions to be plotted making it simpler to identify the region of greatest improvement.

	Annular	Contoured	Difference
η_{stt}	76.01	76.17	0.17
η_{sts}	67.95	68.38	0.43
η_{rtt}	80.47	80.73	0.26
η_{rts}	71.49	72.03	0.54
ϵ_{de}	69.10	74.76	5.66

Table 7.2: Comparison of design efficacy to efficiencies

The design efficacy for the steady state results presented by Snedden (2011) were used as validation and is presented below. Efficiency was used for comparison since design efficacy was developed as a replacement for efficiency when temperature and pressure data are not available or not reliable. Table 7.2 shows the various efficiencies, η_{stt} being stage total-to-total , η_{sts} being stage total-to-static and η_{rtt} and η_{rts} being rotor total-to-total and total-to-static respectively. The trend shows that the contoured endwall provides an improvement in efficiency. However, the improvement in efficiency in each case was small, making it crucial that the efficiency be accurate. Snedden *et al.* (2010*b*) showed that numerical efficiencies can be inaccurate depending on the conditions. Specifically at low Mach numbers and low temperatures. When the percentage change in temperature and pressure are small, the uncertainty (or error if dealing with CFD) can have a large impact on the isentropic efficiency (Dunn *et al.*, 2011*b*). Therefore a large difference between the annular and contoured results would be preferable.

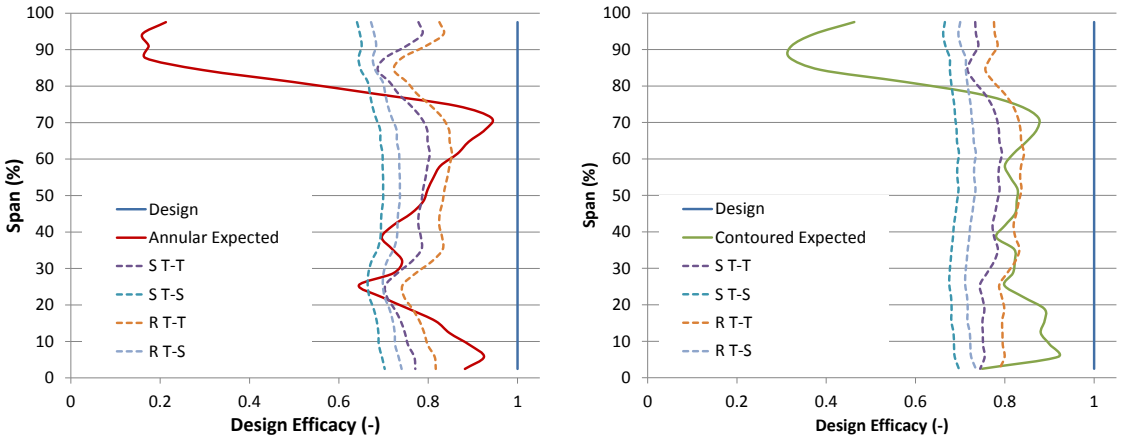

(a) Annular Endwall (b) Contoured Endwall

Figure 7.2: Comparison of design efficacy to efficiency

Figure 7.2 shows a comparison of the design efficacy and the rotor and stage efficiencies (total-to-total and total-to-static). It can be seen that the design efficacy and the efficiencies show very similar characteristics with the trend of the total-to-total matching

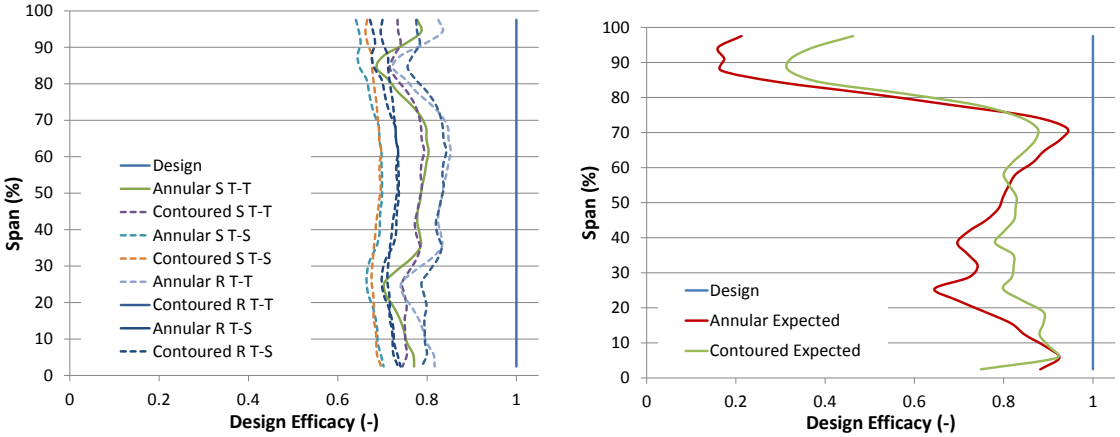

(a) Efficiency (b) Design Efficacy

Figure 7.3: Comparison of annular and contoured design efficacy with efficiency

the design efficacy the best. It can be seen that the design efficacy gives an "exaggerated" representation of efficiency with peaks being more pronounced due to the flow field.

In Figure 7.3a the annular and contoured design efficacies were compared. Solid lines are for the annular case and dashed lines for the contoured case. Lines of the same colour indicate same type of efficiency, with T-T being total-to-total and S-T being static-to-total efficiency. It can be seen that the differences between the the annular and contoured cases are small, with the midspan flows showing very small differences. Figure 7.3b shows the design efficacy for the annular and the contoured cases and a much larger difference can be seen.

It should be noted that for design efficacy to be effective something must be known about the required (design) flow field. For this reason some thought is required when the design flow field is not appropriate as a target for the optimisation. This would be in cases where changes to the primary flow would be beneficial, for instance, when a change of loading is required for improvement.

Chapter 8

Conclusions and Recommendations

8.1 Conclusions

The current work formed part of a larger investigation which started at Durham University with the design and testing of a non-axisymmetric endwall contour and aimed at answering questions which arose during the process. The follow on steady state investigation was performed at CSIR that incorporated an adapted endwall contour based on that developed at Durham University into a rotating test turbine. The current investigation extended that investigation into the unsteady domain.

The work in the current investigations was aimed at understanding the unsteady nature of the flow in a annular test turbine with and without endwall contours at design and off-design conditions. In addition it was required that numerical simulations be performed to determine if unsteady simulations increase the understanding of the flow field in the vicinity of the endwall contour. The open literature does not have a wealth of papers available that cover the unsteady effects of a contoured rotor endwall in a rotating turbine environment, this thesis aimed at helping to populate the gap.

The 1 $\frac{1}{2}$ stage turbine test rig at CSIR was re-instrumented with a commercially available hotfilm system from TSI Inc. namely the IFA 300. Some electronics were manufactured at the CSIR to create a step wave to indicate the rotor relative position for phase lock averaging. Standard operating procedures were developed and implemented that ensure that the measurements produce accurate results. The final result is an unsteady flow field data set of a rotating turbine that shows the effect of incidence as well as addition of a rotor endwall contour. At the time of writing it was the only known data set of its type available. Schüpbach *et al.* (2009) performed unsteady measurements investigating endwall contours, however no temporal data was analysed. The unsteady measurements were to allow for a frozen rotor to be observed so as to analyse the rotor relative flow.

In general the rotor endwall contour, which was originally designed for a linear cascade was found to improve the rotor exit flow field making it more radially uniform, which improves the downstream blade row incidence angle. The temporal profile was likewise more uniform, with the amplitude of the oscillations reduced which resulted in a lower FFT magnitude at the blade passing frequency below midspan. The harmonics observed were of the order of the uncertainty and thus nothing was concluded from them.

Previous observation that the tip leakage flow was increased by the endwall contour was found to be due to the blade in the test rig flexing under the aerodynamic load. The difference in the numerical results at the tip was not observed in the unsteady data set,

and thus the difference observed in the steady numerical work was speculated to be due to a physical instability in the flow such as vortex shedding. Slight differences to the flow field would then be evident, depending on where in the process of vortex shedding the solution finished.

The numerical work showed that the endwall secondary flow vortex system was more radially distributed with a less tightly wrapped endwall secondary flow vortex system due to a weakened cross passage pressure gradient. The endwall secondary flow vortex system of the hub and casing meet at midspan producing a vortex core that was flattened at the meeting point at midspan. The blade pressure profiles show that the contoured rotor has become more forward and aft loaded. Looking at the pressure profiles slightly off the blade show that the oscillations to the bulk flow are too small to penetrate the boundary layer. The unsteady flow field verifies this, showing that the oscillations occur about the time averaged values.

The unsteady investigation (both experimental and numerical) required a large amount of time and effort to obtain results, which did not reveal enough information to warrant the added expense of steady investigations. This was due to a quasi-steady rotor flow environment having constant, uniform inlet conditions. For the design process of the endwall contour, which typically consists of an optimization routine, unsteady numerical simulations are impractical. Steady state turbulence models (this excludes LES) still do not accurately capture the complex flow field in the turbine.

A new objective function for use in endwall secondary flow design was proposed named "Design Efficacy". Design efficacy aims to improve the flow such that the design blade (stator or rotor) exit velocity field is sought after. Design efficacy as calculated for the current test case has shown to have the potential to be a valid proxy for efficiency showing similar trends to efficiency, but exaggerating the difference between the annular and contoured rotor.

To answer the original questions posed in the introduction it was found that: The contoured rotor does affect the unsteady flow field but the change was linked to the reduction in endwall secondary flow; the unsteady CFD did not produce results that were significantly different to those of the steady results; the steady and unsteady flow fields were similar with the largest differences being due to the difference in measurement technique; and the off design results showed similar changes to those seen in the design results, differing in magnitude only.

8.2 Recommendations for future work

Blade flex was found to be a major contributing factor to the differences observed at the blade tip and needs further investigation. Major aspects of concern that need to be addressed are the extent of the flexing and its effect on the flow. The potential for a fluid-structure analysis is highlighted due to the blade loading changing with flexing of the blade. As part of this investigation a modal analysis of the blade would be beneficial to determine at what level, if any, an improvement to flutter onset can be achieved.

An investigation would be beneficial that can measure instantaneous loss, for instance with a FRAP probe or a 5 hole Kulite probe. This would enable the measurement of a complete unsteady data set which includes efficiency and thus loss making for an excellent numerical validation case.

The tested endwall was originally designed for a linear cascade. It is recommended

that a custom designed contoured endwall be designed for and experimentally tested in the current test turbine. Jonathan Bergh is currently in the process of such a design, having generated a preliminary endwall design. The current design, however, has not yet been experimentally tested.

In order to properly validate design efficacy as a objective function, it should be used in an optimisation. Due to the nature of the design efficacy it need not be an endwall design but could be optimisation of the blade stacking for example. The applicability of the assumptions needs to be proven to be robust enough to make design efficacy a valid objective function. It is currently being utilised as part of an investigation by Numeca Ingenieurbüro to determine its applicability and the results are much anticipated.

List of References

Abu-Ghannam, B. and Shaw, R. (1980). Natural transition of boundary layer - the effect of turbulence, pressure gradient and flow history. *Journal of Mechanical Engineering Science*, vol. 22 (5), pp. 213–228.

Addison, J. and Hodson, H. (1990 April*a*). Unsteady transition in an axial-flow turbine: Part 1-measurements on the turbine rotor. *Journal of Turbomachinery*, vol. 112, no. 2, pp. 206–214.

Addison, J. and Hodson, H. (1990 April*b*). Unsteady transition in an axial-flow turbine: Part 2-cascade measurements and modeling. *Journal of Turbomachinery*, vol. 112, no. 2, pp. 215–221.

Atkins, M. (1987). Secondary losses and endwall profiling in a turbine cascade. *I Mech E C225/87*, pp. 29–42.

Banieghbal, M., Curtis, E., Denton, J., Hodson, H., Huntsman, I. and Shulte, V. (1996 January). Wake passing in lp turbine blades. In: *AGARD Conference Proceedings 571: Loss Mechanisms and Unsteady Flows in Turbomachines*, AGARD-CP-571. AGARD, NATO.

Becz, S., Majewski, M. and Langston, L. (2003). Leading edge modification effects on turbine cascade endwall loss. ASME TURBO EXPO GT-2003-38898.

Behr, T., Kalfas, A. and Abhari, R. (2006 may). Unsteady flow physics and performance of a one-and-1/2 stage unshrouded high work turbine. In: *ASME Turbo Expo 2006: Power for Land Sea and Air*. ASME GT2006-90959.

Belik, L. (1972). The secondary flow about circular cylinders mounted normal to a flat plate. *Aeronautical Quarterly*, pp. 47–54.

Bindon, J. (1979). The effect of hub inlet boundary layer skewing on the endwall shear flow in an annular turbine cascade. In: *ASME 79-GT-13*. ASME 79-GT-13.

Bindon, J. (1980). Exit plane and suction surface flows in an annular turbine cascade with a skewed inlet boundary layer. *International Journal of Heat and Fluid Flow*, vol. 2 No. 2, pp. 57–66.

Boletis, E., Sieverding, C. and Hove, W.V. (1983). Effects of skewed inlet endwall boundary layer on the three dimensional flow field of an annular turbine cascade. AGARD CP351 Paper 16.

Brennan, G., Harvey, N., Rose, M., Fomison, N. and Taylor, M. (2001). Improving the efficiency of the trent 500 hp turbine using non-axisymmetric end walls: Part 1 turbine design. In: *ASME TURBO EXPO 2001*. ASME 2001-GT-0444.

Cicatelli, G. and Sieverding, C. (1996 January). A review of the research on unsteady turbine blade wake characteristics. In: *AGARD Conference Proceedings 571: Loss Mechanisms and Unsteady Flows in Turbomachines*, AGARD-CP-571. AGARD, NATO.

Cohen, H., Rogers, G. and Saravanamuttoo, H. (1996). *Gas Turbine theory*. 4th edn. Longman Group Limited.

Coleman, H. and Steele, G. (1989). *Experimentation and Uncertainty Analysis for Engineers*. Wiley Interscience.

Denton, J. (1993). Loss mechanisms in turbomachines. In: *ASME Gas Turbine Congress*, pp. 1–40. Scholars Paper.

Dixon, S. (1992). *Thermodynamics of Turbomachinery*. 3rd edn. Pergamon Press.

Dunham, J. and Meauze, G. (1998). Agard working group study of 3d navier-stokes codes applied to single turbomachinery blade rows. ASME 98-GT-50.

Dunn, D. (2006). *The numerical investigation of a bank of delta plenum air-cooled heat exchangers*. Master's thesis, University of Cape Town.

Dunn, D.I., Snedden, G., Roos, T. and Hildebrandt, T. (2011 September*a*). Application of transition modelling in CFD for use with turbine blades. In: *ISABE-2011*. ISABE-2011-1723.

Dunn, D.I., Snedden, G. and von Backström, T.W. (2010 January). Experimental investigation into the unsteady effects of non-axisymmetric turbine endwall contouring. In: *SACAM2010*. SACAM10-079.

Dunn, D.I., Snedden, G. and von Backström, T.W. (2011 September*b*). Numerical investigation into the unsteady effects of non-axisymmetric turbine endwall contouring on secondary flows. In: *ISABE-2011*. ISABE-2011-1715.

Dunn, D.I., Snedden, G. and von Backström, T.W. (2013 June). Unsteady effects of a generic non-axisymmetric endwall contour on the rotor of a 1.5 stage low speed turbine test rig. In: *ASME Turbo Expo 2013: Power for Land Sea and Air*. GT2013-94961.

Eymann, S., Reinmoller, U., Niehuis, R., Forster, W., M, B. and Gier, J. (2002). Improving 3D flow characteristics in a multistage lp turbine by means of endwall contouring and airfoil design modification - part 1: Design and experimental investigation. ASME TURBO EXPO GT-2002-30352.

Gregory-Smith, D. (1997). Lecture 1: Physics of secondary flows lecture 2: Sec- ondary flows and vorticity lecture 3: Secondary loss: Loss generation, effect of blade design, loss correlations and modelling. von Karman Institute for Fluid Mechanics. Secondary and Tip Clearance Flows in Axial Turbines.

Gregory-Smith, D., Ingram, G., Jayaraman, P., Harvey, N. and Rose, M. (2001). Non-axisymmetric turbine end wall profiling. *Journal of Power & Energy*, vol. 215, no. Part A, pp. 721–734.

Harrison, S. (1989). *The Influence of Blade Stacking on Turbine Losses*. Ph.D. thesis, Department of Engineering, University of Cambridge.

Harrison, S. (1990). Secondary loss generation in a linear cascade of high-turning turbine blades. *Transactions of ASME Journal of Turbomachinery*, vol. 112, pp. 618–624.

Harvey, N., Brennan, G., Newman, D. and Rose, M. (2002). Improving turbine efficiency using non-axisymmetric endwalls: Validation in the multi-row environment and with low aspect ratio blading. In: *ASME TURBO EXPO 2002*. ASME 2002-GT-30337.

Harvey, N. and Ramsden, K. (2000). A computational study of a novel turbine rotor partial shroud. In: *ASME Turbo Expo 2000 Paper 2000-GT-668*.

Hawthorne, W. (1955). Rotational flow through cascades. *Journal of Mechanical and Applied Mathematics*, vol. 3.

Hilditch, M., Smith, G., Anderson, S. and Chana, K. (1996 January). Unsteady measurements in an axial flow turbine. In: *AGARD Conference Proceedings 571: Loss Mechanisms and Unsteady Flows in Turbomachines*, AGARD-CP-571. AGARD, NATO.

Hilfer, M., Ingram, G. and Hogg, S. (2012 June 11-15). Endwall profiling with tip clearance flows. In: *Proceedings of ASME Turbo Expo 2012*. GT2012-68488.

Hodson, H. and Dominy, R. (1987 apr*a*). The off-design performance of a low-pressure turbine cascade. *Transaction of the ASME Journal of Turbomachinery*, vol. 109, pp. 201–209.

Hodson, H. and Dominy, R. (1987*b*). Three-dimensional flow in a low pressure turbine cascade at its design condition. *Transaction of the ASME Journal of Turbomachinery*, vol. 109, pp. 177–185.

Howell, R., Ramesh, O., Hodson, H., Harvey, N. and Schulte, V. (2000). High lift and aft loaded profiles for low pressure turbines. In: *ASME Turbo Expo 2000 Paper 2000-GT-261.*

Ingram, G. (2003 July). *Endwall Profiling for the Reduction of Secondary Flow in Turbines*. Ph.D. thesis, University of Durham.

Ingram, G., Gregory-Smith, D. and Harvey, N. (2003). Experimental quantification of the benefits of end-wall profiling in a turbine cascade. ISABE 2003-1101.

Ingram, G., Gregory-Smith, D., Rose, M., Harvey, N. and G, B. (2002). The effect of end-wall profiling on secondary flow and loss development in a turbine cascade. In: *ASME TURBO EXPO 2002*. ASME 2002-GT-30339.

Japikse, D. (ed.) (1986 March). *ADVANCED TOPICS IN TURBOMACHINERY TECHNOLOGY*. Principal Lecture Series No.2. Concepts ETI, Inc., Norwich, Vermont 05055, USA.

Jouini, D., Little, D., Bancalari, E., Dunn, M., Haldeman, C. and Johnson, P. (2003). Experimental investigation of airfoil wake clocking impacts on aerodynamic performance in a two stage turbine test rig. In: *ASME TURBO EXPO*. ASME TURBO EXPO GT-2003-38872.

Kaiser, I. (1996). *The effect of tip clearance and tip gap geometry on the performance of a one and a half stage axial gas turbine*. Ph.D. thesis, University of KwaZulu Natal.

Kawai, T., Shinoki, S. and Adachi, T. (1989). Secondary flow control and loss reduction in a turbine cascade using endwall fences. *JSME International Journal Series 2: Fluids Engineering Heat Transfer, Power Combustion Thermophysical Properties*, vol. 32 No. 3, pp. 375–387.

Knezevici, D., Sjolander, S., Praisner, T., Allen-Bradley, E. and Grover, E. (2009 June). Measurements of secondary losses in a high-lift front-loaded turbine cascade with the implementation of non-axisymmetric endwall contouring. In: *ASME Turbo Expo 2009: Power for Land Sea and Air*. ASME GT2009-59677.

Langston, L. (2001). Secondary flows in axial turbines - a review. *Heat Transfer in Gas Turbine Systems Annals of the N.Y.Academy of Sciences.*

Langston, L., Nice, M. and Hooper, R. (1977). Three-dimensional flow within a turbine cascade passage. *Transactions of ASME Journal of Engineering for Power*, pp. 21–28.

Liu, X. and Rodi, W. (1994). Velocity measurement of wake-induced unsteady flow in a linear turbine cascade. *Experiments in Fluids*, vol. 17, pp. 45–58.

Lott, P.T., Hills, N.J., Chew, J.W., Scanlon, T. and Shahrokh, S. (2009 June). High pressure turbine stage endwall profile optimisation for performance and rim seal effectiveness. In: *ASME Turbo Expo 2009: Power for Land Sea and Air*. ASME GT2009-59923.

MacPherson, R. and Ingram, G. (2010). Endwall profile design for the durham cascade using genetic algorithms. vol. ASSP-25, pp. –. South African Association for Theoretical and Applied Mechanics, SACAM10.

Marchal, P. and Sieverding, C. (1977). Secondary flows within turbomachine bladings. In: *Secondary flows in turbomachines*, vol. AGARD-CP-214 Paper 11.

Matsunuma, T. (2006 May). Unsteady flowfield of an axial-flow turbine rotor at a low reynolds number. In: *ASME Turbo Expo 2006: Power for Land Sea and Air*. ASME GT2006-90013.

Menter, F.R. (1994). Two-equation eddy-viscosity turbulence models for engineering applications. *AIAA Journal*, vol. 32, pp. 269–289.

Miller, R.J. (2013 June). Mechanical work potential;. In: *Proceedings of ASME Turbo Expo 2013*, GT2013-95488. ASME, ASME.

Moore, J. (1985). Calculation of 3d flow without numerical mixing. pp. 8.1–8.15. AGARD-LS-140 3D Computational Techniques applied to Internal Flows in Propulsion Systems.

Moustapha, S., Paron, G. and Wade, J. (1985). Secondary flows in cascades of highly loaded turbine blades. *Transactions of ASME Journal of Engineering for Gas Turbines and Power*, vol. 107, pp. 1031–1038.

Muller, R., Sauer, H., Vogeler, K. and Hoeger, M. (2002). Influencing the secondary losses in compressor cascades by a leading edge bulb modification at the endwall. ASME TURBO EXPO GT-2002-30442.

Muller, R. and Vogeler, K. (2005). Reduction of the secondary losses in compressor cascades using a leading edge bulb modification. In: *European Turbomachinery Conference*.

NREC (1972). *The design and performance analysis of axial-flow turbines: Volumes I and II*. Northern Research and Engineering Corporation.

Numeca (2007 October). *User Manual FINE/Turbo v8 (including Euranus) Documentation v8a*. Numeca International, 5, Avenue Franklin Roosevelt, 1050 Brussels, Belgium, v8a edn.

Numeca International (2008 August). Numeca brochure. `http://www.numeca.com/fileadmin/user_upload/numeca_brochure_01.pdf`.

Park, J., Choi, M. and Baek, J. (2006 may). Effects of the clocking on the internal flow in a 1.5 stage axial turbine. In: *ASME Turbo Expo 2006: Power for Land Sea and Air*. ASME GT2006-90472.

Perlman, B.S. and Auerbach, V.H. (1977). A phase-locking technique for estimating the ensemble average of time-series data. In: *IEEE Transactions on Acoustics, Speech and Signal Processing*, vol. ASSP-25, pp. 295–299.

Perry, A.E. (1982). *Thermodynamics of Turbomachinery*. 1st edn. Oxford University Press, USA.

Porreca, L., Yun, Y., Kalfas, A., Song, S. and Abhari, R. (2006 may). Investigation of 3D unsteady flows in a two stage shrouded axial turbine using stereoscopic PIV and FRAP part i: Interstage flow interactions. In: *ASME Turbo Expo 2006: Power for Land Sea and Air*. ASME GT2006-90752.

Prato, J., Lakshminarayana, B. and Suryavamshi, N. (2002). Development and assessment of hot-film sensor technique for the multistage turbomachinery environment. *International Journal of Rotating Machinery*, vol. 8(5), pp. 361–374.

Pullan, G., Denton, J. and Curtis, E. (2005 jun). Improving the performance of a turbine with low aspect ratio stators by aft-loading. In: *ASME Turbo Expo 2005: Power for Land Sea and Air*. ASME GT2005-68548.

Rose, M. (1994). Non-axisymmetric endwall profiling in the HP NGV's of an axial flow gas turbine. In: *ASME 94-GT-249*.

Rose, M., Harvey, N., Seaman, P., Newman, D. and McManus, D. (2001). Improving the efficiency of the trent 500 hp turbine using non-axisymmetric end walls: part 2: Experimental validation. In: *ASME TURBO EXPO 2001*. ASME 2001-GT-0505.

Rose, M.G. (2011). *Habilitation thesis: Unsteady Flow in Axial Turbines*. Ph.D. thesis, Universität Stuttgart.

Rose, M.G., Jenny, P., Gier, J. and Abhari, R.S. (2013). Experimentally observed unsteady work at inlet to and exit from an axial flow turbine rotor. *Journal of Turbomachinery*.

Saravanamuttoo, H., Rogers, G. and Cohen, H. (2001). *Gas Turbine theory*. 5th edn. Pearson Education Limited.

Saravanamuttoo, H., Rogers, G., Cohen, H. and Straznicky, P. (2009). *Gas Turbine theory*. 6th edn. Pearson Education Limited.

Schlienger, J., Kalfas, A.I. and Abhari, R.S. (2005 February). Vortex-wake-blade interaction in a shrouded axial turbine. *Journal of Turbomachinery*, vol. 127, no. 4, pp. 699–707.

Schobeiri, M.T., Abdelfattah, S. and Chibli, C. (2012). Investigating the cause of computational fluid dynamics deficiencies in accurately predicting the efficiency and performance of high pressure turbines: A combined experimental and numerical study. *Journal of fluids engineering*, vol. 134, pp. 1–12.

Schüpbach, P., Rose, M., Gier, J., Raab, I., Germain, T. and Abhari, R.S. (2009). Non-axisymmetric endwall profiles including fillet radii, in a 1.5 stage axial flow turbine. Proceedings of the 8th European Conference on Turbomachinery Fluid Dynamics and Thermodynamics (ETC '09).

Sharma, O. and Butler, T. (1986). Predictions of endwall losses and secondary flows in axial flow turbine cascades. In: *ASME*. ASME 86-GT-228.

Sharma, O.P., Renaud, E., Butler, T., Millsaps, K., Dring, R.P. and Joslyn, H.D. (1988). Rotor-stator interaction in multi-stage axial-flow turbines. In: *AIAA/ASME/SAE/ASEE 24th Joint Propulsion Conference*.

Sieverding, C. (1985*a*). Recent progress in the understanding of the basic aspects of secondary flows in turbine blade passages. *Transactions of ASME Journal of Engineering for Gas Turbines and Power*, vol. 107, pp. 248–252.

Sieverding, C. (1985*b*). Secondary flows in straight and annular turbine cascades.

Snedden, G. (2011). *The Application of Non-Axisymmetric Endwall Contourning in a 1.5 stage, Rotating Turbine*. Ph.D. thesis, School of Engineering, Durham University.

Snedden, G., Dunn, D., Ingram, G. and Gregory-Smith, D. (2010 June*a*). The performance of a generic non-axisymmetric end wall in a single stage, rotating turbine at on and off-design conditions. In: *ASME Turbo Expo 2010: Power for Land Sea and Air*. GT2010-22006.

Snedden, G., Dunn, D., Ingram, G. and von Backström, T.W. (2010 January *b*). Observations on the selection of objective function for the optimisation of turbine endwalls using computational fluid dynamics. In: *SACAM10*. South African Association for Theoretical and Applied Mechanics.

Snedden, G., Dunn, D.I., Ingram, G.L. and Gregory-Smith, D.G. (2009). The application of non-axisymmetric endwall contouring in a single stage, rotating turbine. In: *ASME Turbo Expo*, GT2009-59169.

Snedden, G., Roos, T., Dunn, D. and Gregory-Smith, D. (2007). Characterisation of a refurbished 1 1/2 stage turbine test rig for flowfield mapping behind blading with non-axisymmetric contoured endwalls. ISABE 2007-1363.

Sonntag, R.E., Borgnakke, C. and van Wylen, G.J. (2003). *Fundamentals of Thermodynamics*. 6th edn. John Wiley and Sons International.

Swelbar, W. and Belobaba, P. (2010). "Airline Data Project", MIT Global Airline Industry Programme. http://web.mit.edu/airlinedata/www/default.html.

Tecplot Inc. (2008 August). *Tecplot 360 User Manual*. Tecplot Inc, Tecplot, Inc. (formerly Amtec Engineering, Inc.) 3535 Factoria Blvd S.E. Suite 550 Bellevue, WA 98006, 2nd edn.

TSI Incorporated (2000 August). *IFA 300 Constant temperature Anemometer System: Instruction Manual*. TSI Incorporated, 500 Cardigan Road, St. Paul MN 55164, revision b edn.

TSI Incorporated (2003 July). *Model 1129 automated air velocity calibrator: Instruction Manual*. TSI Incorporated, 500 Cardigan Road, St. Paul MN 55164, revision b edn.

TSI Incorporated (2013 July). *TSI Thermal Anemometry Probes...* TSI Incorporated, 500 Cardigan Road, St. Paul MN 55164, p/n 2980465 rev b edn.

United Nations Framework Convention on Climate Change (UNFCCC) (2013 December). Kyoto protocol. `http://unfccc.int/kyoto_protocol/items/3145.php`.

Van Den Berg, B. and Bertelrud, A. (1988). Measurement techniques in low speed turbulent flows: A report on euromech 202. In: *Experiments in Fluids 6*, pp. 61–66.

Versteeg, H. and Malalasekera, W. (1995). *An Introduction to Computational Fluid Dynamics*. Prentice Hall, Harlow.

Vogt, H. and Zippel, M. (1996). Sekundarstromungen in turbinengittern mit geraden und gekrummten schaufeln; visualisierung im ebenen wasserkanal. *Forschung im Ingenieurwesen, Engineering Research*, vol. 62 no. 9, pp. 247 – 253.

Walsh, J. and Gregory-Smith, D. (1987). The effect of inlet skew on the secondary flow and losses in a turbine cascade. In: *Proceedings of the Institute of Mechanical Engineering International Conference - Turbomachinery Efficiency Prediction and Improvement*, pp. 15–28.

Walsh, J. and Gregory-Smith, D. (1990). Inlet skew and the growth of secondary losses and vorticity in a turbine cascade. *Transaction of the ASME Journal of Turbomachinery*, vol. 112, pp. 633–642.

Wang, Z.-D., Han, W. and Xu, W. (1987). An experimental investigation into the influence of diameter-blade height ratios on secondary flow losses in annular cascades with leaned blades. In: *AMSE 87-GT-131*.

Watanabe, H. and Harada, H. (1999). Supression of secondary flows in turbine nozzle with controlled stacking shape and exit circulation by 3d inverse design method. ASME 99-GT-72.

Wilcox, D. (1998). *Turbulence Modeling for CFD*. DCW Industries, Inc., La Canada, California.

Zweifel, O. (1945 December). *The spacing of turbo-machine blading, especially with large deflection*. The Brown Boveri Review.

Appendix A

Digital Appendix

The DVD provided with this thesis contains a series of PowerPoint slides. They are divided up per test case, one file per loading condition. Not all of the quantities were included, and not all of those include were explicitly covered. Those quantities which aided in interpreting the flow field.